

**THE INVESTIGATION OF ENERGY ABSORPTION
CHARACTERISTICS OF TPU TPMS STRUCTURES
SUBJECTED TO IMPACT LOADING**

**A Thesis Submitted to
The Graduate School of Engineering and Sciences of
İzmir Institute of Technology
in Partial Fulfillment of the Requirements for the Degree of**

MASTER OF SCIENCE

in Mechanical Engineering

**by
Çetin BAKICI**

**JULY 2023
İZMİR**

We approve the thesis of **Çetin BAKICI**

Examining Committee Members:

Prof. Dr. Alper TAŞDEMİRCİ

Department of Mechanical Engineering, İzmir Institute of Technology

Prof. Dr. Hatice Seçil ARTEM

Department of Mechanical Engineering, İzmir Institute of Technology

Prof. Dr. Evren Meltem TOYGAR

Department of Mechanical Engineering, Dokuz Eylül University

4 July 2023

Prof. Dr. Alper TAŞDEMİRCİ

Supervisor, Department of
Mechanical Engineering
İzmir Institute of Technology

Prof. Dr. M. İ. Can DEDE

Head of the Department of
Mechanical Engineering

Prof. Dr. Mehtap EANES

Dean of the Graduate School of
Engineering and Sciences

ACKNOWLEDGMENTS

I would like to thank my advisor Prof. Dr. Alper TAŞDEMİRÇİ for inspiring and encouraging me during my thesis study. In the light of his expertise and support, I have been able to complete my studies.

I would like to state that my thankfulness to nTOPOLOGY for the software support to the thesis.

Furthermore, I want to express my gratitude to my mother İlknur BAKICI, my father Ercan BAKICI, and my sister Ece CALP for their emotional support during completion of my thesis. Special thanks to Mesut BAYHAN for their invaluable assistance during the experimental work and Dynamic Testing and Modeling Laboratory Team for their support.

Lastly, I would like to thank my dear girlfriend Dilşad KAYA whose love and endless support encouraged me to overcome this hardworking study.

ABSTRACT

THE INVESTIGATION OF ENERGY ABSORPTION CHARACTERISTICS OF TPU TPMS STRUCTURES SUBJECTED TO IMPACT LOADING

In this thesis, the energy absorption capability of a schwarz based TPMS structure both experimentally and numerically was investigated. In the product, TPU material and FDM printer was used. Instead of the regular schwarz primitive cell structure, which has been frequently examined in the literature, the sandwich structure design was prepared with the geometry selected from the region between two cells was used and its advantages were compared. In the selection of the TPMS structure, both its high energy absorption capability per unit weight and its geometry suitable for mass production in the future was important. A hyperelastic material TPU and a printer suitable for its production were selected to show deformation behaviour of the structure against multiple loading. After material characterization with TPU specimens, the determined printer parameters were kept constant, and single and multiple cell structures were produced. Static and dynamic tests were performed, and single and multiple-cell structures were modeled and validated in the LS-DYNA finite element package program. It was observed that as the strain rate increases, the structures densification point also decreased and the first peak force and the energy absorption per unit weight (SAE) increase. In addition, it was observed that the deformation behaviour of single and multiple-cell structures were rate dependent. It has been observed that the structure with 9 cells absorbs 20% more energy than the structure with unit cell, which is 9 times higher than the unit cell structure due to the interaction of cells. The developed structure was numerically exposed to blast loads following Nato Stanag 4569 standart. In this standart, from the defined of the injury criteria, on the lower and upper tibia joint should experienced force values lower than 2.6 kN and 5.4 kN respectively. From the numerical simulations, it was found that the structure was able to mitigate the blast load transmitted to the during the acceptable limits.

ÖZET

ÇARPMA YÜKÜNE MARUZ TPU TPMS YAPILARIN ENERJİ EMME KARAKTERİSTİKLERİNİN İNCELENMESİ

Bu çalışmada, 3 boyutlu üretim yöntemlerinden biri olan eriyik yığıma modellemesi (FDM) ile üretimi yapılmış termoplastik poliüretan (TPU) Üç Yönlü Periyodik Minimal Yüzey (TPMS) schwarz primitive çekirdek yapısıyla elde edilmiş parçanın özellikle darbe yüklerindeki enerji emme kabiliyeti incelenmiştir. Literatürde sıkça incelenilen klasik schwarz primitive hücre yapısı yerine, iki hücre arası bölgeden seçilen geometri ile hazırlanan sandviç yapı tasarımı kullanılmış ve avantajları karşılaştırılmıştır. TPMS yapının seçiminde hem birim başına yüksek enerji soğurma kabiliyeti hem de ileride seri üretime geçebilmeye uygun geometri olması önem teşkil etmiştir. Yapının birden fazla yükleme karşısında eski şekline gelme kabiliyetini göstermesi için hiperelastik bir filament olan TPU ve üretimine uygun yazıcı seçilmiştir. 3D ile üretilmiş TPU numuneleri ile malzeme karakterizasyonu yapıldıktan sonra belirlenen yazıcı parametreleri sabit tutulup tekli ve çoklu hücre yapıları üretilmiştir. Statik ve dinamik testleri yapılan tekli ve çoklu hücre yapıları, LS-DYNA sonlu elemanlar paket programında modellenerek doğrulanmıştır. Elde edilen sonuçlara göre, gerinim hızı arttıkça yapının daha erken yoğunlaşma evresine girdiği, ilk pik kuvvetinin ve birim ağırlığa düşen enerji emme miktarının (SAE) arttığı gözlemlenmiştir. Ayrıca tekli ve çoklu hücre yapılarının deformasyon hızına bağlı olarak şekil değiştirme tarihçesinde değiştiği gözlemlenmiştir. 9 hücreye sahip yapının tekli hücreye sahip olan yapıdan, hücrelerin birbiri ile etkileşiminden kaynaklı tekli ezilme davranışının 9 katından %20 daha fazla enerji emdiği gözlemlenmiştir. Son olarak Conwep yöntemi kullanılarak, taban pedi olarak TPU TPMS yapı ile hazırlanan patlama modelinde Nato Stanag 4569'a göre alt tibia ve üst tibia kemiği bağlantı noktası için sırasıyla 5.4 kN ve 2.6 kN olan sakatlanma kriterinin altında kaldığı görülmüştür.

TABLE OF CONTENTS

TABLE OF CONTENTS.....	vi
LIST OF FIGURES	viii
LIST OF TABLES.....	xii
CHAPTER 1. INTRODUCTION	1
1.1. Literature Review	3
1.1.1. Energy Absorbtion Mechanism.....	3
1.1.2. Additive Manufacturing	6
1.1.2.1. Fused Deposition Modelling	9
1.1.3. Cellular Structures	12
1.1.3.1. TPMS Structures	13
1.1.4. TPU	16
1.1.5. Blast Wave Propagation	22
1.2. Aim of the Study	25
CHAPTER 2. MANUFACTURING, CHARACTERIZATION AND TESTING	
METHOD	27
2.1. 3D Printing Process by FDM	27
2.1.1. Specimen Preparation.....	30
2.2. Material Characterization and Crushing Tests	32
2.2.1. Quasi-Static Testing	32
2.2.1.1. Tensile Test	33
2.2.1.2. Poisson’s Test.....	34
2.2.1.3. Compression Test.....	35
2.2.2. Dynamic Testing	36
2.2.2.1. Direct Impact.....	37
2.2.2.2. Drop Weight Test	40
2.2.2.3. SHPB Test	42

CHAPTER 3. NUMERICAL METHODOLOGY	47
3.1. Available Material Models in Ls-Dyna.....	49
3.2. Material Model Selection.....	50
3.2.1. Mooney Rivlin Rubber (MAT_27)	51
3.2.2. Simplified Rubber (MAT_181).....	52
3.3. Validation Numerical Models	54
3.3.1. Single Element Compression	54
3.3.2. SHPB.....	55
3.4. Numerical Modeling of Dynamic And Static Tests of Core Structures.....	57
3.4.1. Static Compression.....	57
3.4.2. Direct Impact.....	59
3.4.3. Drop Weight	61
3.4.4. Blast.....	62
 CHAPTER 4. EXPERIMENTAL AND NUMERICAL RESULTS.....	 64
4.1. Validation of Numerical Model and Test Result	71
4.2. Unit Cell Structure Static and Dynamic Compression Results	73
4.2.1. Strain Rate and Micro-inertia Effects for One Cell Structure	80
4.2.2. Nine Cell Structures Static and Dynamic Compression Results	83
4.3. Numerical Results of Blast Model	91
 CHAPTER 5. CONCLUSIONS	 96
 REFERENCES	 99

LIST OF FIGURES

<u>Figure</u>	<u>Page</u>
Figure 1.1. One of the usage areas of TPU in the defense industry.....	2
Figure 1.2. (a) A typical compression load-displacement response of a metallic lattice (b) An example graph of energy absorption efficiency versus displacement	4
Figure 1.3. Two types of structures: (a) type I load–displacement curve, (b) type II.....	5
Figure 1.4. (a) This single-piece rocket propulsion engine (b) Additively manufactured bracket (c) The CCM Super Tacks X is the first hockey helmet interior to be 3D printed	7
Figure 1.5. Despite being the same size, the lattice structure on the right has a surface area that is 4 times greater than the cylinder on the left and weighs 4 times less.....	8
Figure 1.6. Process flow diagram for fused deposition modeling (FDM)	10
Figure 1.7. (a) Honeycomb (b) Auxetic structure.....	13
Figure 1.8. Some of the tpms types and their formulas	15
Figure 1.9. Mechanisms of deformation in various TPMS structures	16
Figure 1.10. TPU copolymer	17
Figure 1.11. Uniaxial compression and tensile tests of the 3D printed TPU material	18
Figure 1.12. (a) Engineering stress – strain curve of the SKYDEX© at different strain rates (b) Deformation history of one cell SKYDEX©	21
Figure 1.13. Friedlander waveform	23
Figure 1.14. Numerical model and axial force on tibia with pad	24
Figure 1.15. Comparison of the final plate profile along the plate's symmetry plane between expected and measured results.....	25
Figure 2.1. Some type of infill direction.....	29
Figure 2.2. Printing illustration with outer shell and 45/-45 infill type.....	29
Figure 2.3. Dimension of tensile specimen.....	31

<u>Figure</u>	<u>Page</u>
Figure 2.4. Compression cylindrical specimen used for material characterization	31
Figure 2.5. Single-core structure sliced in the Ultimaker Cura software to be produced on the XY plane	32
Figure 2.6. Quasi-static tension test set-up	33
Figure 2.7. (a) Experimental setup of the poisson’s test (b) 3D Cad of the IV. Type specimen	34
Figure 2.8. Quasi-static compression test setup.....	36
Figure 2.9. Experimental consideration at different strain rates.....	37
Figure 2.10. Schematic of Direct Impact Test	38
Figure 2.11. High speed camera and flashlight of the direct impact test.....	39
Figure 2.12. Direct impact test setup	40
Figure 2.13. (a) Drop Weight Test Setup (b) DAS 16000 (c) Impactor and multi-cell structure	41
Figure 2.14. A typical voltage vs. time curve of a SHPB test of 3D printed.....	43
Figure 2.15. Schematic of specimen and waves	44
Figure 2.16. Test setup of the Split Hopkinson Pressure Bar	46
Figure 3.1. The discretization of the TPMS structure in nTopology software.....	47
Figure 3.2. Numerical methodology	48
Figure 3.3. (a) Typical hyperelastic material’s stress-strain curve (b) 3D Printed Stress-strain curve of 3D printed TPU material.....	50
Figure 3.4. MAT_027 material model keyword	51
Figure 3.5. Comparison of hyperelastic material models	52
Figure 3.6. Ls-Dyna MAT_181 Table Input.....	53
Figure 3.7. Boundary and initial conditions of single element model	55
Figure 3.8. Numerical model of the SHPB test	56
Figure 3.9. Mesh sensitivity of cell structure.....	58
Figure 3.10. Numerical model of the unit and nine cells structures static compression	59
Figure 3.11. Numerical model of the direct impact test for unit cell.....	60
Figure 3.12. Double sided tape area trials	60
Figure 3.13. Numerical model of the 9 cells structures drop test	61

<u>Figure</u>	<u>Page</u>
Figure 3.14. Numerical model result of the blast and joint points of the tibia bone.....	63
Figure 3.15. Numerical model prepared with only bottom plate and bottom plate with TPU TPMS structure.....	63
Figure 4.1. $10^{-3}/s$ Quasi-static tensile stress-strain curves	65
Figure 4.2. Comparison of quasi-static tensile stress-strain curve	65
Figure 4.3. $10^{-3}/s$ Quasi-static compression stress-strain curves	66
Figure 4.4. $10^{-2}/s$ Quasi-static compression stress-strain curves	66
Figure 4.5. $10^{-1}/s$ Quasi-static compression stress-strain curves	67
Figure 4.6. Quasi-static compression stress-strain curves comparison	67
Figure 4.7. Comparison of quasi-static and dynamic compression stress-strain curves of 3D printed compression specimens.....	68
Figure 4.8. Input curve of material model in Ls - Dyna	69
Figure 4.9. Displacement of specimen at (a) 0 sec (b) 12.3 sec (c) 24.6 sec (d) 36.9 sec by using DIC	70
Figure 4.10. Comparison of the numerical model by using MAT_181 and the static compression test	71
Figure 4.11. Stress - strain curves of TPU specimen at (a) 2893/s (b) 4157/s strain rate.....	72
Figure 4.12. Comparison of the force displacement and specific absorb energy of (a) the schwarz primitive (b) 90-degree rotation of the investigated cell, (c) investigated cell	74
Figure 4.13. Experimental force-displacement curves of unit cell at $10^{-3}/s$	75
Figure 4.14. The experimental and numerical force-displacement curves for different material model.....	76
Figure 4.15. The effect of the material model type and parameter on peak force	76
Figure 4.16. SAE vs. displacement curves of unit cell structure at $10^{-3}/s$ strain rate.....	77
Figure 4.17. Static experimental and numerical force-displacement history of a unit cell at (a) 0 mm, (b) 2.2 mm, (c) 4.1 mm, (d) 11.4 mm.....	78

<u>Figure</u>	<u>Page</u>
Figure 4.18. Dynamic experimental and numerical force-displacement history of a unit cell at (a) 0 mm, (b) 2.2 mm, (c) 4.1 mm, (d) 11.4 mm.....	79
Figure 4.19. SAE vs. displacement curves comparison of unit cell	80
Figure 4.20. Comparison of force vs. displacement direct impact test and numerical model	81
Figure 4.21. Investigation of inertia effect with rate sensitive experiment and rate insensitive numerical model.....	82
Figure 4.22. The percentage effect ratio-displacement curves of strain rate and inertia	82
Figure 4.23. Experimental and numerical quasi-static compression force-displacement curves of the TPMS 9 cell at (a) 0 mm. (b) 2.2 mm. (c) 4.1 mm. (d) 11.4mm.....	84
Figure 4.24. SAE vs. displacement curves comparison of TPMS multi-core structures.....	85
Figure 4.25. Force vs. displacement and mean force comparison of unit cell and 9 cell structures	85
Figure 4.26. Comparison of force vs. displacement curves of numerical TPU TPMS structure and experiment for single core multiplied by 9 at static test.....	86
Figure 4.27. Comparison of 9 TPMS cell structure numerical and experimental drop - weight test result.....	88
Figure 4.28. Comparison of SAE vs. displacement curves of numerical and experimental for 9 cell structures drop weight test.....	89
Figure 4.29. Comparison of axial force loading on the lower tibia	91
Figure 4.30. Comparison of axial compressive force on lower and upper tibia	92
Figure 4.31. The displacement of the investigated TPU TPMS multi-core structure bottom pad at (a) 0 ms (b) 2.12 ms (c) 4.40 ms (d) 6.66 ms (e) 14.24 ms.....	93
Figure 4.32. The pressure of the designed TPU TPMS multi-core structure bottom pad (a) 0 ms (b) 2.12 ms (c) 4.40 ms (d) 6.66 ms (e) 14.24 ms.	94

LIST OF TABLES

<u>Table</u>	<u>Page</u>
Table 1.1. Comparison of AM technologies.....	9
Table 1.2. Comparison of filament using in FDM machine.....	11
Table 1.3. Comparison between numerical models using MAT 181 and MAT 770.....	20
Table 2.1. 3D Printing settings of TPU.....	28
Table 2.2. Mechanical properties of the aluminum 7075-T6.....	39
Table 2.3. Mechanical properties of the Vascomax C350.....	43
Table 3.1. Summary of numerical models.....	50
Table 3.2. Material model constant.....	53
Table 3.3. Implicit keywords and constants.....	58
Table 4.1. Comparison energy absorption characteristics of unit and nine cell.....	90

CHAPTER 1

INTRODUCTION

Additive manufacturing technologies that have developed since the beginning of the 2000s, highly complex geometries can still be produced quickly. There are different 3D production methods according to the usage areas of these structures. The fused deposition modeling (FDM) method, which is the most frequently used one, has been reduced to our production houses. In this way, even products that cannot be produced conventionally can be obtained easily at meager costs. Thanks to the easy accessibility of the FDM method, it is a popular field, especially for researchers.

The materials used in the FDM method may vary depending on the printer owned. Materials such as PLA and PETG can be easily used with most printers. Materials such as TPU and ABS, printers with additional features are required.

The TPU filament used in this study has the characteristics of high elasticity, wear resistance, and recyclability. Due to its high elasticity, it is difficult to produce with a 3D printer. For this purpose, a 3D printer with a direct drive extruder is used to ensure that printing is more efficient.

TPU material can be as soft as rubber or as hard as plastic. This feature is due to the presence of both hard and soft segments in its chemical structure. The most used area is those that require high energy absorption.

Due to advancements in fabrication techniques and lower mass-production costs, the use of cellular materials in the design of functional components has increased in recent years. Porous structures, defined by their porosity, have several desirable characteristics, including being structurally lightweight, having good thermal conductivity, and offering impact resistance (Mines et al., 2013). Thanks to cellular structures provide high resistance against impact loading and help a lot in weight reduction. That is why the places cover many places, from biomedical applications to the defense industry (Yan et al. 2012; Chu, Graf, and Rosen 2008; Seepersad and Crawford, n.d.; Kladovasilakis, Tsongas, and Tzetzis 2020).

Various lightweight materials (polymers, composites, and sandwich structures) are used further to improve energy absorption capability at relatively low weights.



Figure 1.1. One of the usage areas of TPU in the defense industry
(Source : “Airless Tyres for Military Humvee” 2021)

They are combined with conventional or bio-inspired geometric patterns (honeycomb, square, cylindrical, corrugated, and origami). In these buildings, geometric design and material choice are crucial. New manufacturing methods are being developed, making it feasible to build complicated geometries without sacrificing weight optimization. In addition, inspired structures found in nature may now be created by imitating them thanks to additive manufacturing (AM).

One of the cellular structures is TPMS structures with very low relative densities. Mainly used cells of TPMS structures are Neovious, Gyroid, Schwarz P, Lidinoid, Split P, and Diamond (Miralbes et al. 2020).

Many loading circumstances, such as environmental factors, explosives, and earthquakes, may be applied to the TPU structures. In order to get a better knowledge of the dynamic behavior of TPU under various loading circumstances, researchers have conducted an extensive study.

The aim of the study is to investigate the mechanical behavior of 3D-printed TPU at both low and high strain rates and to investigate the appropriateness of the material models already implemented in LS-DYNA and the determination of the material model constants. Also, the determination of the inertia effect, the energy absorption capacity, and the crushing behavior mode of the TPU TPMS structures. Numerical analyzes of dynamics experiments will provide a better understanding of the dynamic behavior of the structure and reveal the effect of sample geometry by changing the sample geometry.

1.1. Literature Review

In this section, the literature studies that are compatible with the aim of the thesis and will be compared with the results are summarized. It is explained under five sub-titles: energy absorption mechanism, additive manufacturing, cellular structures, TPU, and blast wave propagation.

1.1.1. Energy Absorbtion Mechanism

Several variables must be considered while developing an energy-absorbing structure to ensure its safety and effectiveness. First, material selection is an important consideration. For example, foam or other composite materials should be able to effectively absorb and dissipate energy when employed in the design. The material selected can greatly impact how well a structure can absorb energy and preserve its structural integrity.

The expected impact forces are another important aspect. The designer must consider the size, duration, and direction of the forces that the structure may experience. These pressures may considerably impact the effectiveness of the structure and its capacity to absorb energy. In order to ensure that the structure can withstand the anticipated impact forces, the design should account for them.

It is also necessary to determine the structure's deformation properties. The structure should absorb energy efficiently and fold in a regulated manner without collapsing or damaging its structural integrity. The designer should consider how the structure deforms under load and ensure it can properly propagate energy. An important consideration when developing an energy-absorbing structure is structural integrity. The construction must keep its structural integrity even after absorbing much energy. The designer should ensure the structure's ability to absorb energy without collapsing or deforming excessively, which might compromise its ability to withstand impacts.

Another important factor is how straightforward the installation and maintenance will be. The structure should be easy to construct, maintain, and repair as needed. Again, this is something the designer should make sure of. The structure's overall efficiency and endurance can be considerably impacted by how simple it is to install and maintain.

Environmental considerations should also be made. The designer should consider a structure's performance under various environmental factors, such as temperature, humidity, and corrosion. It should be built to withstand these components to ensure the structure's durability and effectiveness.

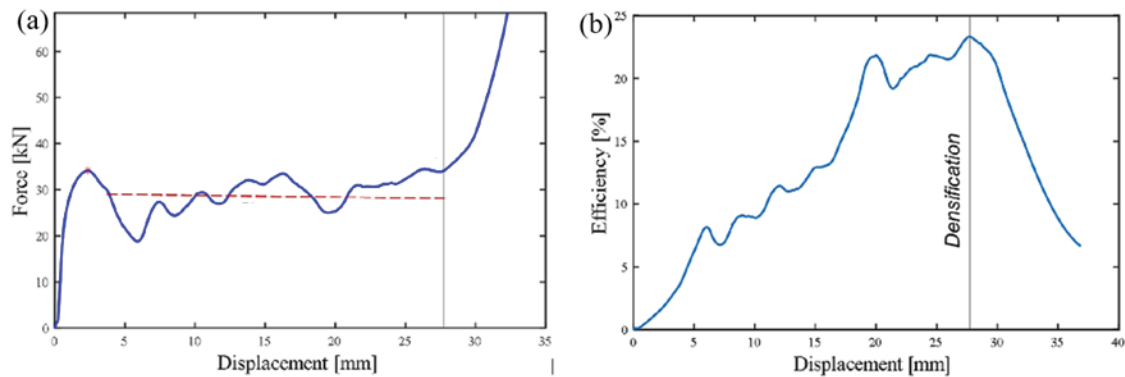


Figure 1.2. (a) A typical compression load-displacement response of a metallic lattice (b) An example graph of energy absorption efficiency versus displacement (Source : du Plessis et al., 2022)

Strain rate sensitivity describes how the deformation behavior of a material varies at various strain rates. They are excellent for energy absorber designs because materials with higher strain rate sensitivity typically have superior energy absorption capability. The kinetic energy of the hit is known as the "inertia effect," and it might cause the absorber to deform and absorb energy. In order to properly absorb and dissipate energy without collapsing, the absorber's design should take into account the kinetic energy of the impact. In order to create an efficient energy absorber, it is crucial to choose a material with high strain rate sensitivity and effective energy dissipation. The kinetic energy of the collision should also be considered while designing the absorber, as well as how the absorber will deform and absorb energy in those circumstances. To attain the highest possible energy absorption capacity and structural integrity, the design should attempt to optimize the shape and material properties of the absorber. A designer can produce an energy absorber that efficiently dissipates energy in the case of an impact by taking strain rate sensitivity and inertia effect into account (Yu et al. 2023; Zhang et al. 2023; Huang et al. 2021).

Typically, there are two types of energy-absorbing structures in terms of the shape of the overall static load-displacement curve: type I has a relatively 'flat-topped' curve (Fig. 2(a)), whilst type II has an initial peak load followed by a 'steeply falling' curve

(Fig. 2(b)) (Lu and Yu 2003; Palanivelu et al. 2011; Vimal Kannan and Rajkumar 2020). Among the deformation type mechanisms mentioned in the literature with trigger mode, the crushing efficiency of type I type structures is higher.

The literature has also shown that the "initial imperfection" of the structure has a significant impact on the "inertia sensitivity" for type II structures. The disparity between the dynamic and static performances of type II structures would be further increased by the rate dependency of material characteristics (Su, Yu, and Reid 1995).

The "crashworthiness" feature, which indicates the sensitivity of a structure under impact loads, can be utilized to measure the energy absorption capacity. Various studies have been made in the literature on this term, especially in the military and automotive industries. Developments in the automotive field necessitated focusing on crashworthiness; therefore, the tendency to design structures with high energy absorption capacity from composite to polymer has increased (Davis 1972; McHenry and Miller 1970).

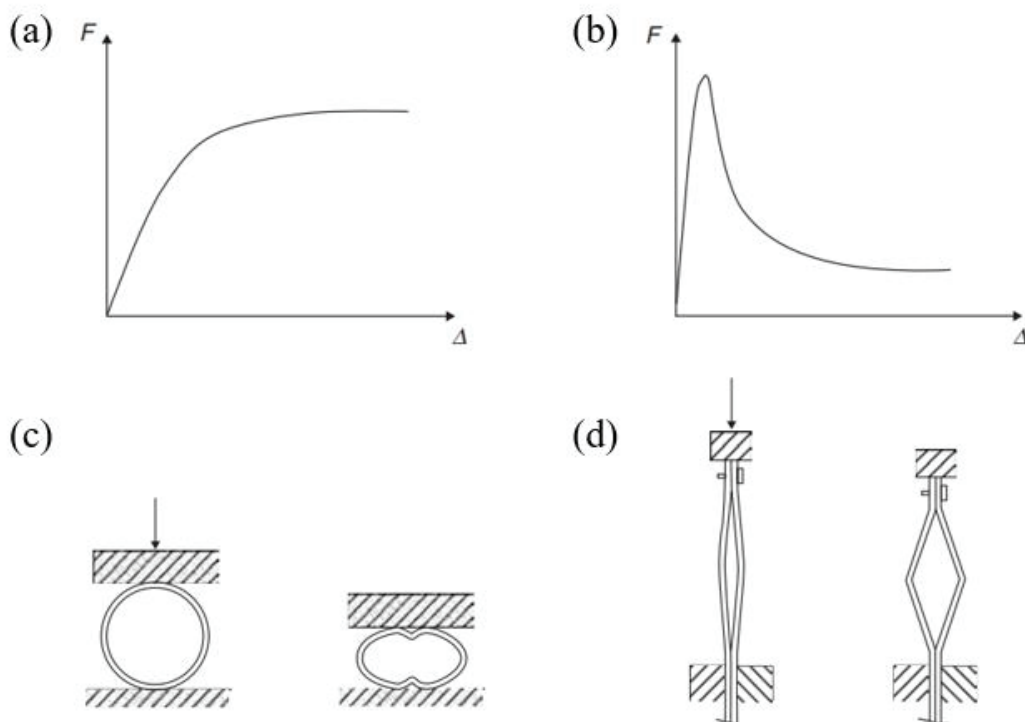


Figure 1.3. Two types of structures: (a) type I load–displacement curve, (b) type II curve, (c) type I – a circular ring, (d) type II –pre-bent plates (Source : Lu & Yu, 2003)

1.1.2. Additive Manufacturing

Additive manufacturing procedures use data from a computer-aided design (CAD) file, which is then transformed to a stereolithography (STL) file. In this procedure, the CAD-created drawing is approximated by triangles and divided into sections containing the details of each layer that will be printed. Using a variety of materials, including plastics, metals, and ceramics, additive manufacturing builds up an object layer by layer rather than cutting or molding a material into the desired shape. This cutting-edge manufacturing technique differs from conventional manufacturing techniques in a number of specific ways.

The capacity to print complicated geometries and elaborate designs that would be challenging or impossible to make with conventional techniques is one of the additive manufacturing's most important features. This is due to the fact that 3D printing can build objects in layers, enabling the gradual construction of complex shapes and designs. The aerospace industry, which uses 3D printing to build complicated components for aircraft and spacecraft, has found this capacity to create complex forms to be of great interest. Engineers can now create components that are lighter and stronger, which has significantly improved performance and efficiency. Figure 1.4 shows some special parts produced by additive manufacturing.

Another advantage of additive manufacturing is the capacity to create small quantities of products at a reasonable price. This is especially helpful for prototyping and customization since it helps designers and engineers build and test new items quickly and effectively. Producing a product in small numbers using conventional manufacturing techniques can be highly costly and need expensive tooling and molds.

In Figure 1.5, it is given that the weight of a cylinder is reduced by 4 times by using the lattice structure for this purpose. However, 3D printing makes it very simple and quick to generate small quantities, which makes it possible to design and test products more effectively.

Additionally, compared to conventional production techniques, additive manufacturing is a more environmentally friendly procedure. This is so that the production process has less environmental impact and produces less waste using recycled resources.

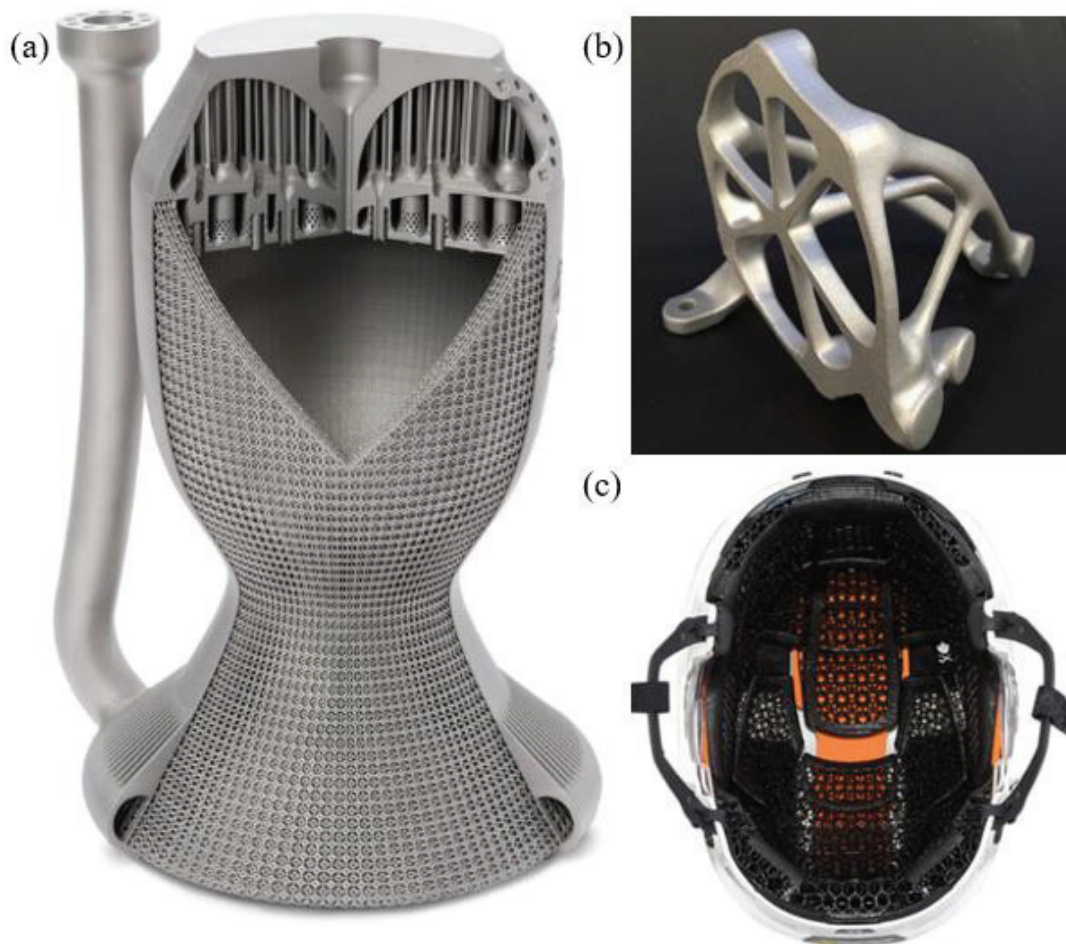


Figure 1.4. (a) This single-piece rocket propulsion engine (b) Additively manufactured bracket (c) The CCM Super Tacks X is the first hockey helmet interior to be 3D printed (Source: (a)Donath,2019; (b) Orme et al., 2017; (c) Shields, 2022)

Additionally, on-demand manufacturing is made possible by 3D printing, which can lessen the need for extensive reserves and surplus stock while also cutting down on waste. A rising trend is 3D printing in sustainable design, where designers create products out of recycled or biodegradable materials, reducing their production's carbon footprint (Pavlenko, Edl, and Kuric 2020; Javaid et al. 2021; Wu et al. 2022; Verhoef et al. 2018).

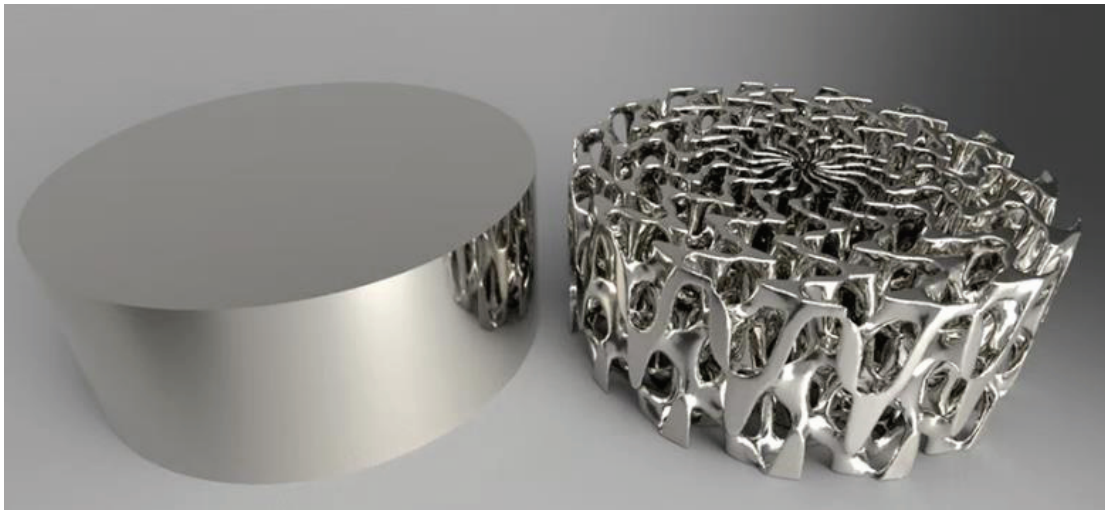


Figure 1.5. Despite being the same size, the lattice structure on the right has a surface area that is 4 times greater than the cylinder on the left and weighs 4 times less (Source: Shziields, 2022)

There are various forms of additive manufacturing, each with a unique combination of positive and negative aspects. The most popular form of additive manufacturing (AM) is fused deposition modeling (FDM), which produces objects by melting thermoplastic material and extruding it layer by layer. In stereolithography (SLA), a liquid resin is cured by a UV laser, while in selective laser sintering (SLS), powdered materials are fused by an intense laser. Digital Light Processing (DLP) is comparable to SLA using a projector rather than a laser, and Material Jetting involves jetting a liquid photopolymer onto a build base. Binder jetting also includes using a liquid binder to bind successive layers of powdered material together (Kanu, Hale, and Piper 2016; Wong and Hernandez 2012).

Despite all of the advantages of additive manufacturing, several issues still need to be resolved. The speed at which printing is done is one of the major obstacles. Even while 3D printing is a reasonably quick procedure, depending on the size and complexity of the object, it can still take many hours or even days to create one. This might be a severe limitation for large-scale manufacturing, where speed is essential for meeting

demand. The price of 3D printing presents another difficulty. Despite recent dramatic reductions in price, 3D printing is still considerably more costly than conventional manufacturing techniques for mass production. This is partly because materials and equipment are more expensive and because printing requires more labor than conventional techniques (Khorram Niaki et al. 2019).

Table 1.1. Comparison of AM technologies
(Source: Kanu et al., 2016)

Technique	Accuracy (μm)	Materials	Advantages	Disadvantages
Selective Laser Sintering	50	Polymers, ceramic		Requires powder, cell-unfriendly environment
Melt Extrusion (including FDM)	100	Thermoplastics, composites	Technologically simple	Requires strong filament and high temperatures
Stereolithography	0.5 – 50	Hydrogels, polymers, ceramic-composites	High accuracy	Single composition, requires photo-curable material
Inkjet Printing	20 – 100	Liquids, hydrogels	Use of existing cheap technology, multiple composition	Low viscosity prevents build-up in 3D, low strength

Despite these difficulties, additive manufacturing is a fast-expanding sector with the potential to revolutionize how we create items. The applications for 3D printing are limitless and range from intricate aerospace components to personalized prosthetics. Moreover, we are likely to see more cutting-edge applications of 3D printing as the technology develops, making it a crucial tool for manufacturers, designers, and engineers.

1.1.2.1. Fused Deposition Modelling

Due to its adaptability and cost, fused deposition modeling (FDM), a typical 3D printing process, has grown in popularity. It produces 3D objects by layer-by-layer

ejecting melted thermoplastic material through a nozzle into a built platform(Figure 1.4). A computer-aided design (CAD) model is used in the procedure and converted into a set of instructions that the printer utilizes to create the thing (Wong and Hernandez 2012; Abdulhameed et al. 2019).

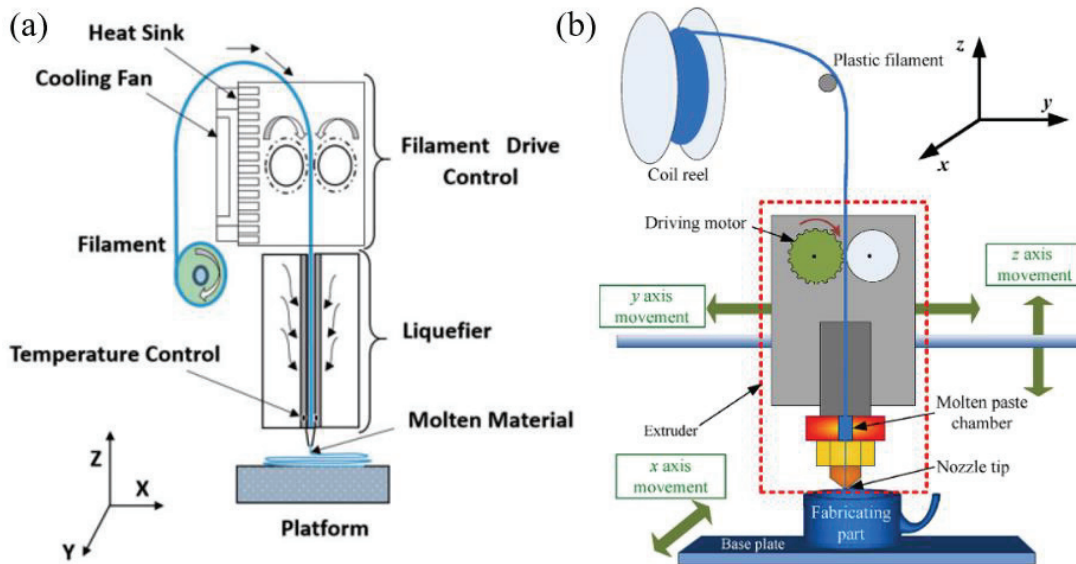


Figure 1.6. Process flow diagram for fused deposition modeling (FDM) (Source: (a) (Papon and Haque 2018) (b) (Jin et al. 2015))

FDM's adaptability is one of its primary benefits. Numerous thermoplastics, such as ABS, PLA, nylon, polycarbonate, and many more, can be printed with it (Table 1.2). Thanks to their versatility, it is possible to design items with a variety of characteristics, such as strength, flexibility, or heat resistance. FDM printers are also more accessible to people and small enterprises due to their affordability when compared to other 3D printing methods like stereolithography (SLA) or selective laser sintering (SLS). The simplicity of use of FDM is another benefit. Several consumer-grade FDM printers are plug-and-play devices, making it simple and quick for people with little or no 3D printing knowledge to set up and use them. Furthermore, while FDM prints use a typical thermoplastic substance, they require little upkeep, and the printers themselves are relatively durable and low-maintenance.

FDM, however, has a few drawbacks as well. For example, the possibility of layer lines showing up on the finished object due to the layer-by-layer printing process is one of the critical issues with FDM. Although it can be reduced using post-processing methods, this is still a problem with FDM prints. Furthermore, FDM printers often have

a lower quality than other 3D printing technologies, which could result in less clarity in minute details.

Table 1.2. Comparison of filament using in FDM machine
(Source: Martin, 2023)

NAME	PLA	ABS	PETG	TPU
Printing Temperature(°C)	180 - 230	210 - 250 °	200 - 260	190 - 245
Printing bed Temperature(°C)	20 - 60	80 - 110	80 - 90	60 - 90
Moisture Absorption	yes	yes	yes	yes
Strength	medium	good	very good (except scratches)	very good
Flexibility	bad	medium	good	perfect
Heat Resistance	bad	medium	good	good
UV-Resistance	medium	medium	medium	good
Water Resistance	medium	medium	good	good
Recyclable	yes	yes	yes	yes

Because of their valuable characteristics, polymers are frequently employed in fused deposition modeling (FDM). They are perfect for producing complicated designs with fine details because of their low melting point, which makes melting and extrusion via a small nozzle simple. In addition to being strong, flexible, and resistant to heat and chemicals, polymers are lightweight, durable, and easily manipulated with additives. They are a popular option for FDM printing in a multitude of applications, including prototyping, product development, and manufacturing, due to their affordability, accessibility, availability, and availability in various colors and finishes.

FDM technology has many possible applications in the military, from designing unique parts and equipment to quick prototyping and tactical analysis. FDM is a suitable technology for applications in the military, where the availability of specialized components and equipment can be crucial. One of its main advantages is its ability to swiftly and readily build parts and equipment. One of the most notable benefits of FDM in the defense industry is its capacity to build unique, on-demand parts fast and efficiently. In a military setting, equipment may be exposed to harsh conditions that could lead to wear and tear and the requirement for replacement parts. In addition, traditional supply

chains might only sometimes be able to supply the essential components on time, which could result in downtime and decreased productivity. By enabling soldiers to print new components and supplies on-demand quickly, FDM technology can resolve this problem (Bird and Ravindra 2021).

1.1.3. Cellular Structures

The potential for using various cellular forms as energy absorbers in engineering uses are being investigated. A typical example is the honeycomb structure, which comprises several hexagonal cells joined together to make a robust and light structure. Honeycomb structures are frequently employed in aeronautical and automotive applications because they offer a significant strength-to-weight ratio and outstanding energy absorption capacity. Compared to other production processes like vacuum forming or injection molding, the automotive sector uses FDM less frequently to produce honeycomb structures. This is because honeycomb structures made using FDM may have relatively thick cell walls, affecting their ability to absorb energy and rendering them less effective than structures made using other manufacturing processes. However, FDM can still make honeycomb structures for prototypes or low-volume production runs. In these circumstances, vacuum forming or other additional manufacturing techniques can be carried out using a master mold made using FDM (Pollard et al. 2017).

Other varieties of cellular structures, in addition to honeycombs are being researched for their capacity to absorb energy. Since they have a high strength-to-weight ratio and can bend plastically in response to stress, face-centered cubic (FCC) and body-centered cubic (BCC) structures are two examples of possible energy absorbers being investigated. They are frequently utilized in impact safety products like helmet liners and car bumpers.

In contrast to most materials, which contract when stretched, auxetic structures expand laterally because they have a negative Poisson's ratio. Auxetic materials are very effective energy absorbers because they can flex beneath stress and absorb more significant amounts of energy than ordinary materials due to their unique characteristic. Bone, tendons, and some fabrics are natural and manufactured materials containing auxetic structures. Auxetic materials are designed and produced for various uses, including safety equipment, implants, and aerospace constructions.

The potential for using lattice structures, which are made up of repeated units of linked struts or beams, as energy absorbers are also being researched. Lattice structures are flexible materials for a variety of engineering applications because they may be made to have particular mechanical characteristics, including stiffness, durability, and energy absorption capacity.

As a last sort of cellular structure, topologically patterned materials (TPMS) are being researched for their capacity to absorb energy. TPMS structures are a good choice for various engineering applications because they contain repetitive patterns that can be altered to influence their mechanical properties. Therefore, researchers are trying to create novel materials that can successfully absorb energy and enhance the performance and safety of numerous constructions and devices by investigating these and other varieties of cellular structures.

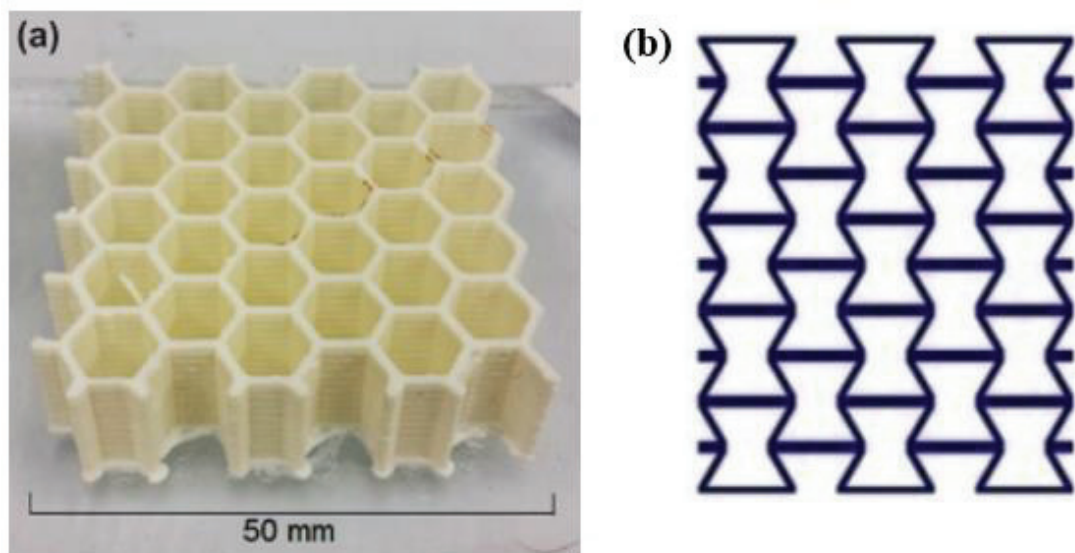


Figure 1.7. (a) Honeycomb (b) Auxetic structures
(Source: (a) de Aquino et al., 2020 (b) Pollard et al., 2017)

1.1.3.1. TPMS Structures

A lattice structure known as a triply periodic minimal surface (TPMS) structure has an interconnected cell pattern that repeats. The minimum amount of surface needed to enclose a given volume is meant by minimization of surface area, which distinguishes these constructions. TPMS structures are defined mathematically as surfaces with zero

mean curvature and periodicity in three dimensions. Solid mechanics and structural analysis principles can be used to study TPMS structures. Numerical simulations like finite element analysis can be used to forecast how TPMS structures will behave under load. The geometry and material qualities of TPMS structures have a significant impact on how they respond structurally (Diosdado-De la Peña et al. 2022; Novak et al. 2023).

The ability of TPMS structures to absorb energy effectively is one of their main benefits. In TPMS structures, the interconnected cells form a unique geometric pattern that dissipates energy over a vast surface area, minimizing stress and strain on every cell. Since they are so good at absorbing impact energy, TPMS structures are frequently employed in products like crash safety systems and protective gear. Additionally, TPMS structures may be inexpensive and lightweight, making them perfect for usage in sectors with limited weight and space, such as the aerospace and automobile industries. The TPMS structures' regular geometric form also makes them very receptive to modern manufacturing processes like additive manufacturing and 3D printing (Yang et al. 2022; Novak et al. 2023). There are various TPMS structure types, each with a unique geometric design and set of mathematical calculations. An intricate network of linked channels that form a continuous, porous network makes up the Gyroid structure. A pattern of diamond-shaped cells that link to create a three-dimensional lattice gives the Diamond structure its name. The Schwarz P surface comprises a repeating array of connected polyhedral cells with a complicated geometric pattern. A recurring pattern of curved cells that join to create a three-dimensional lattice defines the Neovius structure. A three-dimensional lattice is formed by an interconnecting pattern of octahedral cells in the Primitive structure.

The mechanical behavior of Schwarz-P TPMS lattice material under uniaxial compression for two different polymers, PLA and ABS, was examined in the work by Mishra et al. at various compression velocities ranging from 5 mm/min to 35 mm/min.

Although there were modest changes in behavior when strain rates changed, both materials showed multilayer deformation with periodic stress variation. PLA samples were 10% less compressible than ABS samples, although both materials had a propensity for catastrophic failure. PLA samples displayed values up to 30% greater than ABS, and the first peak stress rose linearly with the strain rate. Furthermore, there was very little mechanical behavior difference amongst ABS samples at moderate deformation rates (Mishra, Chavan, and Kumar 2021).

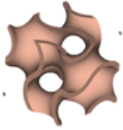
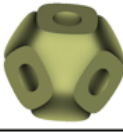
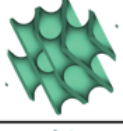
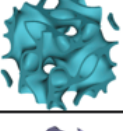
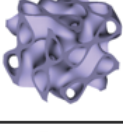
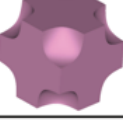
TYPE	GEOMETRY	EQUATION
GYROID		$\sin(x) \cos(y) + \sin(y) \cos(z) + \sin(z) \cos(x)$
SCHWARZ		$\cos(x) + \cos(y) + \cos(z)$
DIAMOND		$\sin(x) * \sin(y) * \sin(z) + \sin(x) * \cos(y) * \cos(z) + \cos(x) * \sin(y) * \cos(z) + \cos(x) * \cos(y) * \sin(z)$
LIDINOID		$\sin(2*x) * \cos(y) * \sin(z) + \sin(2*y) * \cos(z) * \sin(x) + \sin(2*z) * \cos(x) * \sin(y) - \cos(2*x) * \cos(2*y) - \cos(2*y) * \cos(2*z) - \cos(2*z) * \cos(2*x) + .3$
SPLIT P		$1.1 * (\sin(2*x) * \sin(z) * \cos(y) + \sin(2*y) * \sin(x) * \cos(z) + \sin(2*z) * \sin(y) * \cos(x)) - 0.2 * (\cos(2*x) * \cos(2*y) + \cos(2*y) * \cos(2*z) + \cos(2*z) * \cos(2*x)) - 0.4 * (\cos(2*x) + \cos(2*y) + \cos(2*z))$
NEOVIOUS		$3 * (\cos(x) + \cos(y) + \cos(z)) + 4 * \cos(x) * \cos(y) * \cos(z)$

Figure 1.8. Some of the tpms types and their formulas
(Source : McCreight, 2022)

Maskery et al. used mechanical compression testing and FE simulation to study the mechanical behavior of three TPMS lattice structures. It was found that the corresponding stress-strain curve and mechanical properties, as well as the lattice deformation process and failure mechanism, were strongly influenced by the cell geometry. According to the cell shape, it was discovered that the elastic moduli of TPMS lattices varied by over 100%, with the primitive lattice type exceeding both the gyroid and diamond. However, because of its wide variation in the load-bearing area and areas of high stress, the primitive lattice structure showed extremely localized plastic deformation, structure buckling, and low failure strain. For applications that require high strength and stiffness in a single clearly defined loading direction, the study suggests employing a primitive lattice. A gyroid or diamond lattice would be ideal for applications needing high strain before failure (Maskery et al. 2018).

Miralbes et al. looked into the weights, mechanical characteristics, and energy absorption capacities of six distinct types of TPMS structures (Neovious, gyroid, Schwarz

P, Lidinoid, split P, and diamond) under quasi-static compression. These characteristics were contrasted with those of Z-Ultra, the original printing material, and expanded polystyrene foam. According to the study, the Neovious, diamond, and Lidinoid structures are the best alternatives to expanded polystyrene foam, especially for safety helmets with high specific energy absorption capacities (Miralbes et al. 2020).

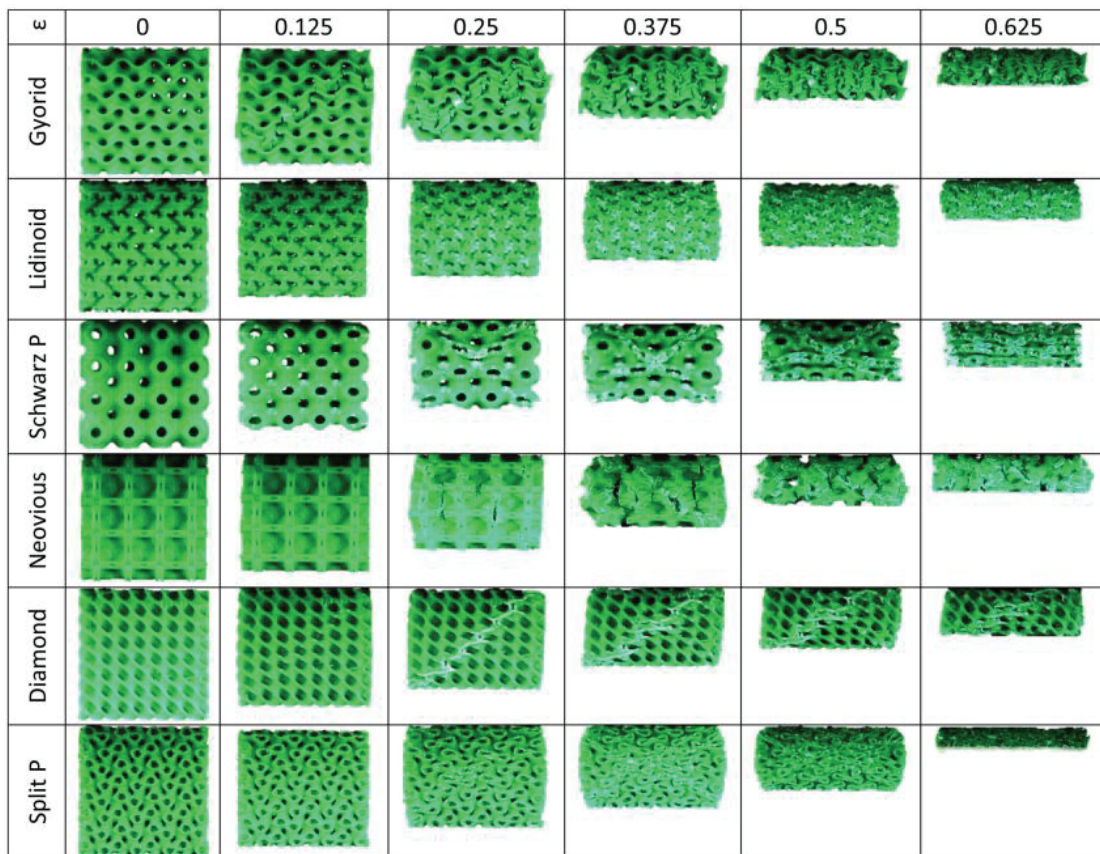


Figure 1.9. Mechanisms of deformation in various TPMS structures (Source : Miralbes et al., 2020)

1.1.4. TPU

The first thermoplastic polyurethanes (TPUs) were produced commercially in the 1950s by Bayer-Fabrenfabriken in Germany and B.F. Goodrich in the United States (Schollenbenger, C.S., Scott, H., Moore 1958). A type of polyurethane elastomer known as thermoplastic polyurethane (TPU) has thermoplastic characteristics. TPUs comprise soft and hard segments joined together by urethane linkages, in contrast to conventional polyurethanes, which are cross-linked thermoset polymers. The hard segments comprise short-chain diisocyanates and chain extenders, while the soft segments are

frequently built of long-chain diols. While the soft portions offer flexibility, the hard segments structure the material. Figure 1.10 describe a typical illustration of a segmented TPU copolymer.

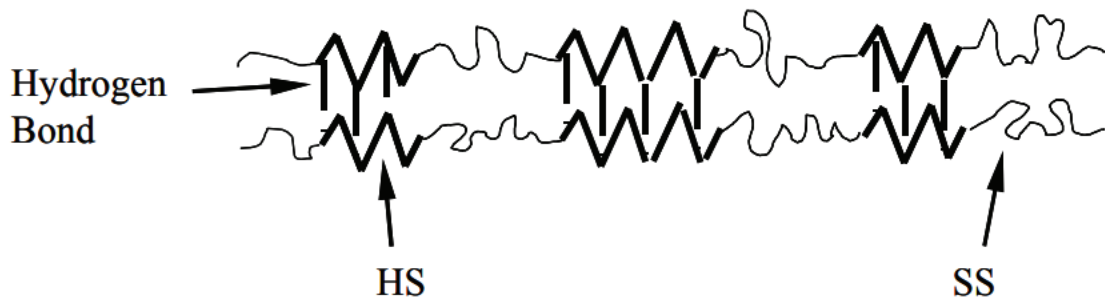


Figure 1.10. TPU copolymer
(Source : Qi & Boyce, 2005)

Both polyurea and polyurethane exhibit strong rate dependence in their stress-strain behavior (Sarva et al. 2007; Raman, Ngo, and Mendis 2011). By employing FFF 3D printing, Vidakis et al. examined the impact of layer height, nozzle temperature, and strain rate on the mechanical characteristics of two materials (PC and TPU). Tensile strength was shown to be more affected than elastic modulus by layer height and nozzle temperature, although strain rate had a less significant effect. For PC material, the divergence for tensile strength was 30%, and for elastic modulus, it was under 20%. The temperature had a more substantial overall impact on TPU material than on other materials, with the deviation for tensile strength being 45% and for elastic modulus being 15% (Vidakis et al. 2021).

Hohimer et al. examined how the nozzle temperature, raster pattern, and air gap affected the ultimate tensile strength (UTS) of thin-walled TPU manufactured using an inexpensive FDM machine. The study discovered that isotropic printed samples might be produced even with different raster patterning. The stress-strain behavior up to the failure point was consistent between the bulk and the samples manufactured with a negative air gap, even though the UTS of the printed samples did not match that of the bulk molded samples. Although temperature and raster pattern had less impact on the UTS, the air gap did. The findings suggested that printed TPU samples may have isotropic mechanical characteristics and that bed or containment temperatures may impact mechanical qualities (Hohimer et al. 2017).

Chaudhry and Czekanski aimed to examine the effects of process parameters on the mechanical performance of TPU materials. In this study, the impacts of infill %, layer height, and raster orientation were examined concerning the mechanical characteristics of the produced parts under quasi-static and high strain rate (2500 s^{-1}) loading. As layer height reduced from 0.4 mm to 0.1 mm, tensile strength increased by 36.5%, demonstrating that layer height was crucial for quasi-static loading. However, infill percentage was the most crucial consideration for high strain rate loading, with 100% infill resulting in a 12.4% improvement in compressive strength compared to 80% infill (Chaudhry and Czekanski 2020).

Mechanical properties	Density (ASTM D792)	Melt Index (210 °C, 1.2 kg)	Elastic Modulus (X-Y) ASTM D638	Tensile Strength (X-Y) ASTM D638	Elongation at Break (X-Y) ASTM D638	Shore Hardness ASTM D2240
TPU 95-Polyflex	1.20–1.24	3–6 (g/10 min)	9.4 ± 0.3 (MPa)	29.0 ± 2.8 (MPa)	330.1 ± 14.9 (%)	95 A

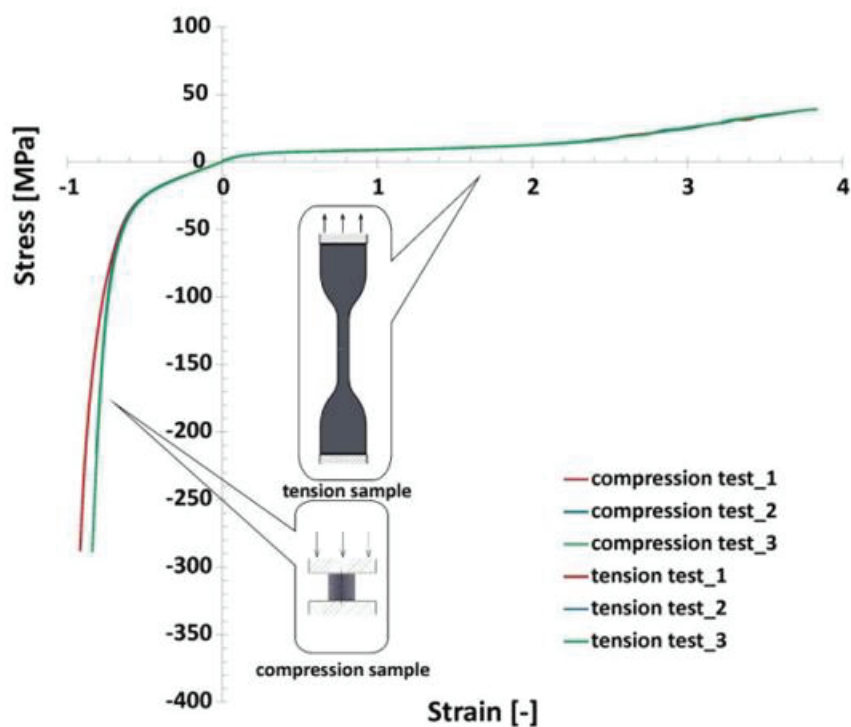


Figure 1.11. Uniaxial compression and tensile tests of the 3D printed TPU material (Source : Płatek et al. 2020)

Płatek et al. used experimental compression experiments and numerical simulations to examine the deformation of regular cell structures under quasi-static load circumstances. The design and production of a regular honeycomb and four variants with various topologies of relative density values using the FDM 3D printing technique in

flexible TPU-Polyflex thermoplastic polyurethane material were all part of the study. The study determined the most effective and precise 3D printing settings for thermoplastic polyurethane filament and discovered that the Polyflex material produced by 3D printing had a non-linear stress-strain relationship and was very flexible. Mechanisms for buckling and bending were blamed for the distortion of produced structures. Numerical simulations were utilized in the study to reflect the mechanical response of the structural specimens under quasi-static compression stress using the Finite Element (FE) method and Ls Dyna software. In addition, the hyperelastic characteristics of the TPU material were described using the Simplified Rubber Material (MAT_181) constitutive model. The suggested FE models and boundary conditions were verified, and the outcomes of numerical models and the data from experimental compression testing showed good agreement (Płatek et al. 2020).

Shepherd et al used impact scenarios to create and validate Finite Element (FE) models for thermoplastic polyurethane (TPU) lattices. The impact response of three auxetic lattices, a traditional honeycomb lattice, two drop hammer kinds, as well as a focused load that frequently occurs in sporting impacts is all explored in this work. The research emphasizes the advantages of FE modeling and additive manufacturing for examining the impact behavior of lattices, especially when it comes to sporting, personal protective equipment (PPE) In the study, the Mooney-rivlin material model with 5 parameters was used for TPU (Shepherd et al. 2020).

Engelbrektsson's thesis covers the finite element program LS-DYNA's modeling and calibration of three material models. While the Soft Tissue model performed better under low and intermediate strain rates, the Ogden Rubber model performed worse during nonlinear strain stiffening. Although the Simplified Rubber model can accommodate nonlinear strain stiffening, this model has the disadvantage of having a rapid reaction in stress to a change in loading velocity. The article presents two material models that accurately predict compressive tests conducted at strain rates of 0.2/s and 100/s. However, more experiments and simulations are required to validate the models fully. It is also pointed out in the article: In analyses involving quasi-static and dynamic strain rates, the bulk modulus values in the material models were taken differently for validation (Engelbrektsson 2011).

Bondy aimed to identify methods for developing accurate and valuable finite element models of chassis components that use hyperelastic materials. The study focused

on several topics, including the characterization of materials in both quasi-static and dynamic environments.

Table 1.3. Comparison between numerical models using MAT 181 and MAT 770

ELEMENT TYPE	MATERIAL CHARACTERIZATION PROCESS	MATERIAL MODEL	ELEMENT FORMULATION	ELEMENT SIZE (mm)	VALIDATION METRIC	CPU TIME (min)
Tetrahedron	Simple compression	MAT 181	10	2	0.98387	3
Tetrahedron	Simple compression	MAT 181	13	2	0.98364	3
Tetrahedron	Simple compression	MAT 181	4	2	0.98267	14
Hexahedron	Simple compression	MAT 181	3	2	0.95116	9
Tetrahedron	Simple compression	MAT 770 8 terms	10	2	0.87854	0.933
Tetrahedron	Simple compression	MAT 770 8 terms	13	2	0.87854	0.95
Hexahedron	Simple compression	MAT 770 8 terms	3	2	0.78655	5

This study establishes different element formulations, element sizes, material models, and single-element models for tension, compression, and shear. The test curves and the stress-strain curves in the single-element models were compared with each other, and a validation matrix was created. As a result of the study, it was found that the tetrahedron element type for compression, the model established with ELFORM 10 and 13, was validated at a rate of approximately 98%. In addition, when MAT_077 and MAT_181 were compared, it was seen that MAT_181 gave 10% more valid results for the same model (Bondy 2013). Jiang et al. introduce the SKYDEX[®] pad, a brand-new, during crash/blast situations, the material is intended to disperse a significant amount of kinetic energy. First, uniaxial compressions with multiple strain rates and drop tests from three heights were used to determine the material's mechanical properties. Then, using homogenized foam-type material laws (MAT_26, MAT_83, and MAT_163) in the LS-DYNA program, numerical models were created without using individual cells based on the test results.

According to calculated data, MAT_163 performed equally well in drop tests, while MAT_83 and MAT_163 performed better in simulations of compression tests. However, of the three material types examined, MAT_163 is considered the best because

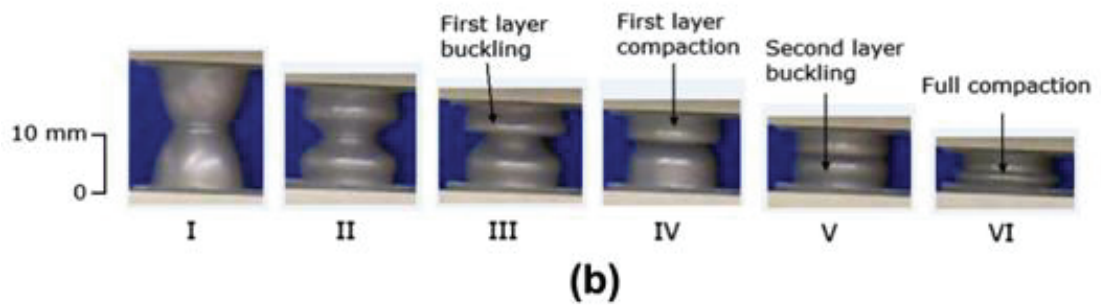
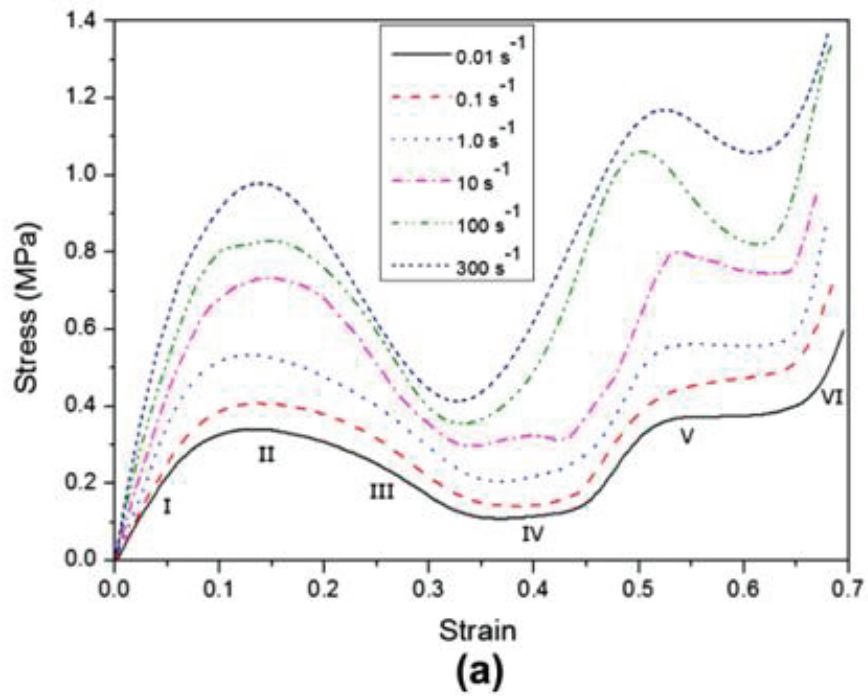


Figure 1.12. (a) Engineering stress – strain curve of the SKYDEX[®] at different strain rates (b) Deformation history of one cell SKYDEX[®] (Source: Jiang et al., 2013)

fewer material constants are needed, and parameter calibration is more straightforward (Jiang et al. 2013).

1.1.5. Blast Wave Propagation

The layer that consists of compressed air in front of the gas produced by the explosion of explosives is known as a blast wave, which holds the majority of the explosion's energy. In an air burst, the pressure rapidly decreases as the blast shock wave expands. Overpressure is the initial peak pressure intensity, which may be many orders of magnitude greater than the sea-level atmospheric pressure. The overpressure spreads outward from the detonation point but finally goes negative as it decays exponentially over time and space. As the shock wave passes by a building on its way, a reflection factor increases the excess pressure. These reflection coefficients usually increase with normal incidence (perpendicular to the source) and decrease with increasing angle of obliquity. Shock waves reflect and multiply by a factor of 13 when encountering a surface. In the final stages of the explosion, the shock wave turns negative. Because the negative phase typically has little impact on the maximal reaction, it is frequently disregarded. The region under the positive portion of the reflected pressure-time curve corresponds to the maximal impulse sent to the structure. Pressure and impulse (or length of time) are necessary to determine the blast loading. The stand-off distance, angles of incidence, and reflect pressure affect the blast pressure pulse in different ways (Kingery 1966).

The pressure is at ambient pressure p_0 before the shock front arrives. When the shock wave gets to the measurement point at an arrival time, and after an explosion was initiated at t_0 , the pressure increases reasonably rapidly to a maximum overpressure value P^0 . After a positive period, the pressure eventually drops to ambient pressure. The positive specific impulse, the side-on impulse, is located in the positive region below the pressure-time trace as shown in Figure 1.13.

There are several ways to model blasts in LSDYNA. The primary techniques for investigating blast response numerically include the CONWEP algorithm, the Arbitrary Lagrangian Eulerian (ALE) approach, the Structured Arbitrary Lagrangian Eulerian (S-ALE) method, and the Smooth Particle Hydrodynamics (SPH) method. Each method has its advantages and disadvantages. With the method CONWEP algorithm, which is the fastest among them, blast pressure can be mapped to the surface determined by empirical

expressions by using the `LOAD_BLAST_ENHANCED` keyword in Ls-Dyna (Niezgoda and Wojtkowski 2013a; Erdik, Kilic, and Ak 2014).

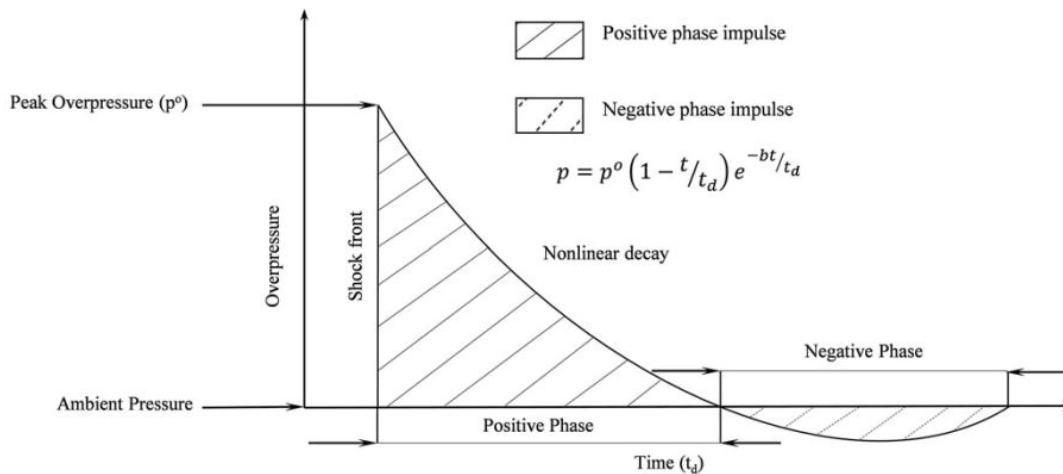


Figure 1.13. Friedlander waveform
(Source : Sundaramurthy et al., 2012)

Williams et al. were performed a series of tests at DRDC - Valcartier employing square aluminum and steel test panels that were subjected to the explosion of buried charges (surrogate mines) containing 6 kg of C4 explosive served as the foundation for the validation. For their problem, they found a difference of 2.2 times over the displacement value of the plate between CONWEP and the experimental (Williams et al. 2002).

In another article were discussed the difficulties in obtaining comprehensive information about improvised explosive devices (IEDs) effects on people. To get around this, the authors perform modeling and experimental research utilizing a 50th percentile numerical HYBRID III dummy to simulate the impact of blast waves on a human body.

Data from the numerical dummy, including hip and knee moment of inertia, femoral force, and foot acceleration, was collected to compare survivorship to injury threshold estimates from other sources (Niezgoda and Wojtkowski 2013a).

Based on NATO STANAG 4569 recommendations, the study comprised mounting a numerical dummy on a rigid seat covered in a thin layer of elastic material and creating impetus with explosive charges of 6 kg, 8 kg, and 10 kg positioned at the average distance between the ground and the bottom of MRAP vehicles. The bottom dimensions used in the investigation were 2000x2000x10 mm, and the impulse was pro-

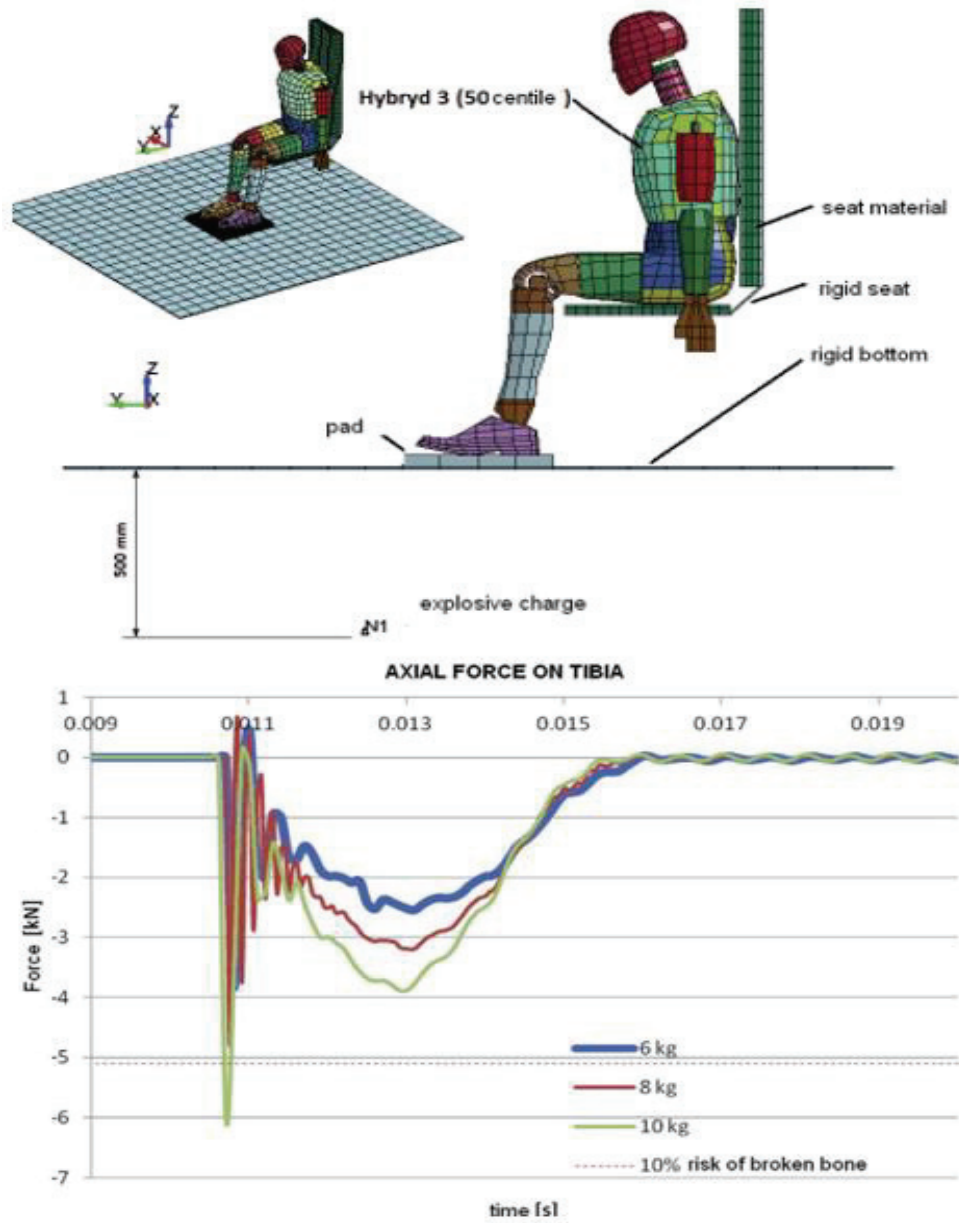


Figure 1.14. Numerical model and axial force on tibia with pad
(Source : Niezgodą & Wojtkowski, 2013)

duced using the CONWEP function. The findings obtained for the identical load situations demonstrated a significant improvement in energy absorption, which supports the usage of additional protection.

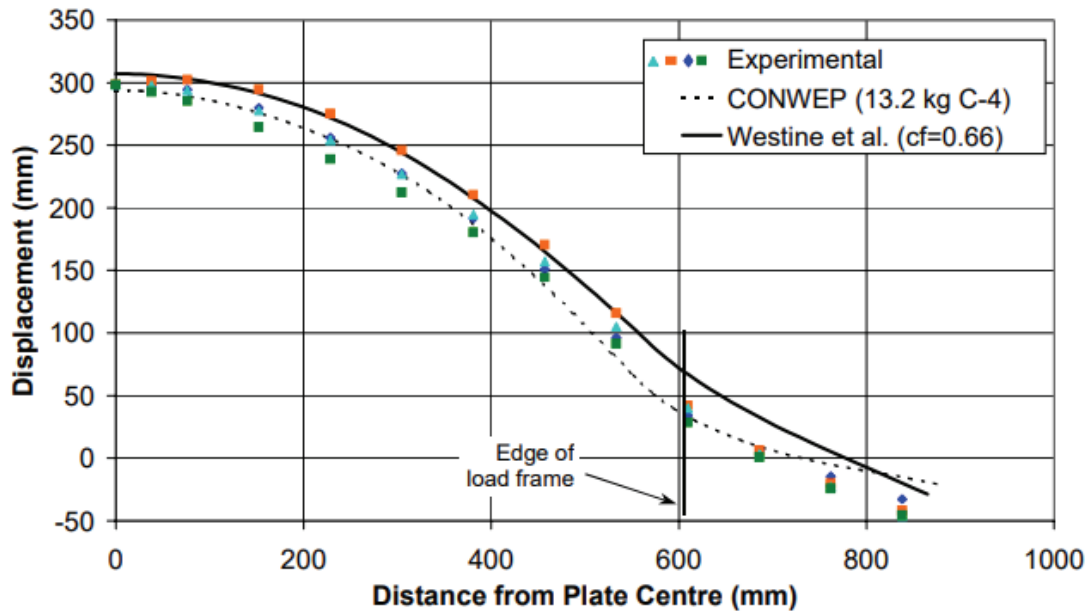


Figure 1.15. Comparison of the final plate profile along the plate's symmetry plane between expected and measured results (Source : Williams et al., 2002)

1.2. Aim of the Study

The aim of this thesis is to design a new cellular structure with high energy absorption capacity, inspired by the schwarz-type cell structure, instead of the cell structures frequently examined in the literature from the Triply Periodic Minimally Surface (TPMS) structures. In addition, it is aimed to examine the interaction between the cell walls of the selected cell structure at both static and dynamic loading conditions.

Although several studies have examined TPMS structures, there are few studies characterizing thermoplastic polyurethane (TPU) and then comparing it with single and multiple cells.

The static and dynamic compression characteristics of the structure developed with single and multiple cells was investigated both experimental and numerical. In order to reveal the effect of rate sensitivity and micro-inertia, numerical simulation were re-run by taking into account the rate sensitivity effects or not.

Having a validated numerical model then allowed to investigate the behaviour of the structure against blast type of loads. Then energy absorption capabilities were compared.

In order to obtain the material model parameters of the TPU used, an extensive mechanical characterization study carried out. TPU is known of its different behaviour under tension and compression loading thus the study was further extended to incorporate these effects. The strain rate dependency of the TPU was also determined during the study.

CHAPTER 2

MANUFACTURING, CHARACTERIZATION AND TESTING METHOD

Surfaces with zero mean curvature" are how differential geometry defines minimal surfaces. The sum of the primary curvatures at each place, in other words, is zero. This implies they are equally convex and concave in all directions, giving them a saddle-like or hyperbolic shape. They are called minimal because the area of a "minimal surface" is extreme compared to other surfaces with the same boundary curve when given a set boundary curve. The 3D printing method was selected to produce the structures due to their fast and high ability to manufacture challenging parts. PLA and ABS are mainly used for 3D printing, but hyperplastic materials such as TPU have increased day by day in recent years.

2.1. 3D Printing Process by FDM

The FDM machine Creality SERMOON D1 has 280 mm X 260 mm X 310 mm maximum print size and 0.1 mm printing accuracy. Also, the machine can produce near-industrial prints between 0.1 and 0.4 mm layer thicknesses. In this study, a 0.4 mm nozzle diameter was used to print the structure. This machine is easily supported to print PLA/ABS and TPU. Domestic brand 1.75 diameter TPU filament was used to manufacture the structures. Since there is no datasheet about this filament, it has been tried to find the optimum temperature between 200 degrees and 260 degrees, which is the maximum printing temperature of the machine, by increasing it by 5 degrees. As a result of the studies, optimum print quality was obtained at 215 degrees, and this value was kept constant in future tests. At the same time, there was no recommended value information in the printing table. Therefore, the optimum temperature was determined between 50 and 80 degrees by increasing it by 5 degrees. Around 60 degrees, no failure was observed by the filament sticking to the plate during the printing. This temperature value is also constant for future tests. Has been kept. All these adjustments can be made to the finest detail in the Ultimaker Cura, and this program was used for the settings in this study.

Table 2.1. 3D Printing settings of TPU

PARAMETERS	VALUES
Nozzle Diameter	0.4 mm
Layer Thickness	0.2 mm
Wall Thickness	0.8 mm(0.4x2)
Fill Percentage	%100
Wall Printing Speed	10 mm/s
Infill Printing Speed	5 mm/s
Nozzle Temperature	215 C
Bed Temperature	60 C

Besides the parameters mentioned above, build orientation is the parameter that has the most influence on the determination of mechanical properties. Therefore, even with the same 3D printer and operating parameters, the mechanical properties of samples generated in different build orientations (flat, on-edge, upright) will vary significantly. High-height structures are challenging to print on on-edge and horizontal axis(Caminero 2017). This is because it becomes more difficult to control the temperature changes in the structure as you move away from the printing table. As the height increases, supports may be required to prevent the strength from decreasing. Then it will be difficult to remove it from inside the structure. Therefore, in this study, the XY axis was chosen instead of the XZ axis to print the design. Thanks to this choice, the use of support during the optimization of the structure was avoided as much as possible, and even if the support was used, it could be easily removed. Since the structure is complex, the support formed inside cannot be removed. This method has been used. As a result of the tests performed, no delamination was observed in the sample.

Besides the printing axis, infill orientation and layer height are also challenging. This study carried out tests for tensile specimens in different layer heights and infill orientations (0/90,45/-45) printed with TPU filament. When we look at the result, 0.2 layer height and strength of 45/-45 sample are the highest stiffness(Chaudhry and Czekanski 2020).

Hence, 0.2 layer height and 45/-45 raster angle were used in this study. To use as bulk samples as possible in material characterization, 100% infill density was used.

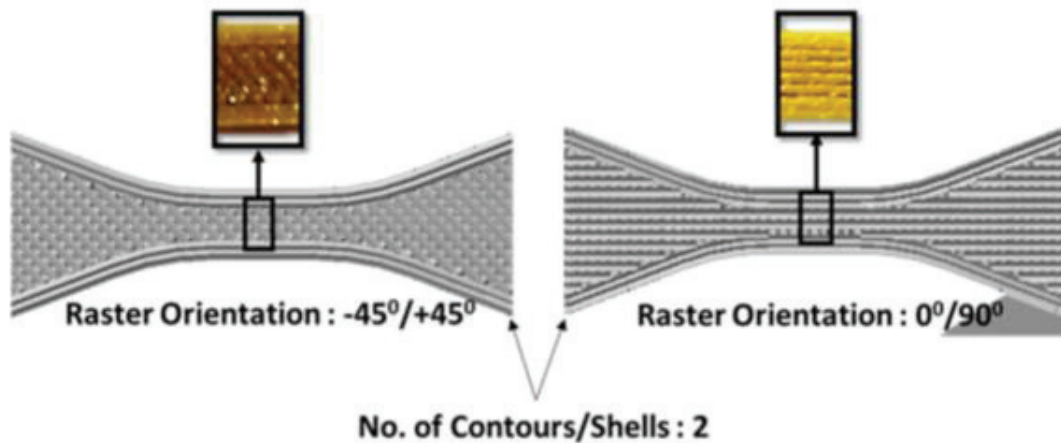


Figure 2.1. Some type of infill direction
 (Source: Chaudhry and Czekanski 2020)

The printing process starts from the outer wall first, and after the two outer walls are finished, the inner wall is passed. Afterward, the inner side is filled according to the infill option. It was observed that it created a lot of air gaps on the walls during the printing process. Therefore, before starting the production, it was kept at 75 Celcius for about 45 minutes,

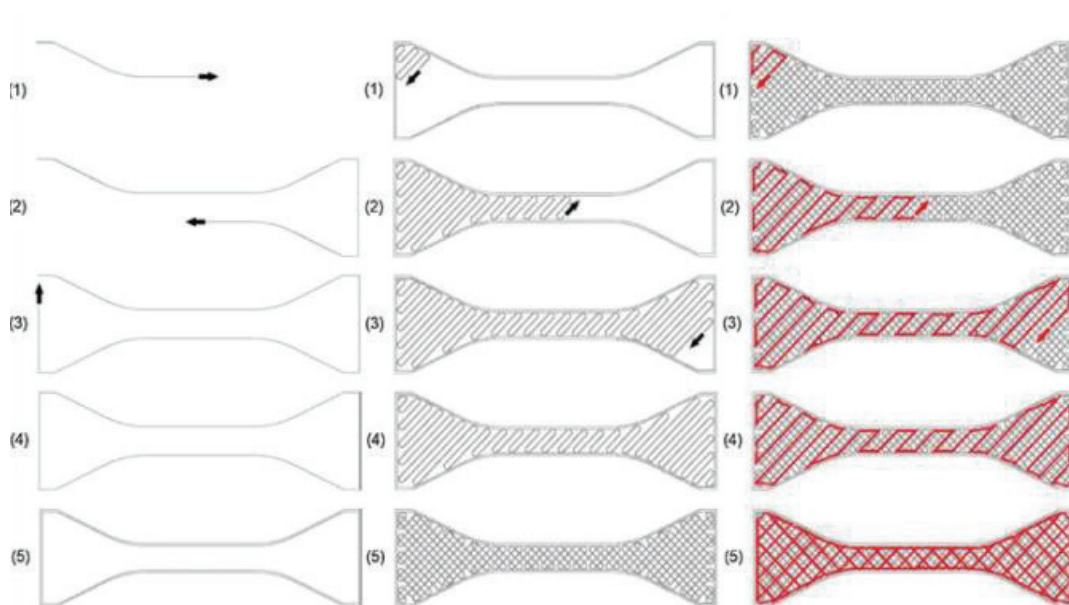


Figure 2.2. Printing illustration with outer shell and 45/-45 infill type
 (Source : Webbe et al. 2019)

In the preliminary study, Since the TPU filament absorbs a lot of moisture, it has and then production began, and each sample was aimed to be obtained as a result of the same conditions.

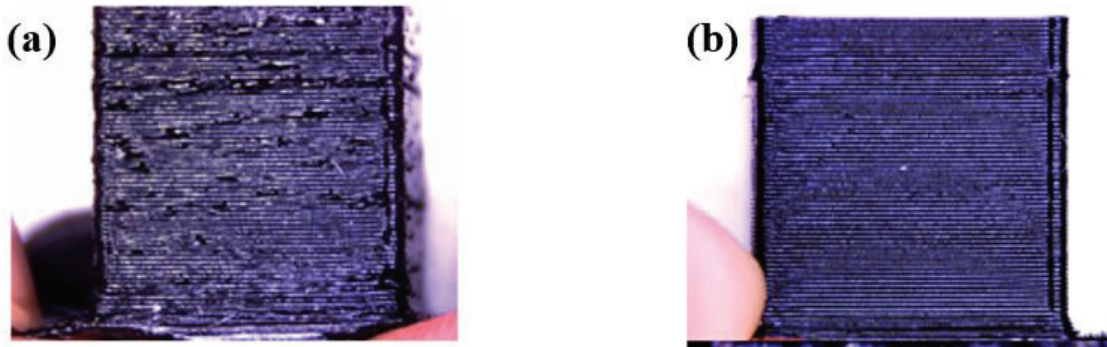


Figure 2.3. (a) TPU specimen produced without preheating (b) TPU specimen produced by preheating

As a result of the additional studies, the optimum value of the printing speed has been set as 10 mm/s for the walls and five mm/s for the infill. The skirt option has been activated to ensure that the sample adheres to the hotbed more.

2.1.1. Specimen Preparation

Specimen preparation was applied for both material characterization tests and TPMS structures, with the same printer settings being valid. Two different samples, static and dynamic, were produced for the tensile tests. Two different samples, static and dynamic, were produced for the tensile tests. While the cubic sample was produced for the compression tests, a thinner cylindrical sample was produced after checking the compatibility resulting from the tests. In the light of the printing techniques obtained from the samples produced for characterization, one-cell, four-cell, and nine-cell structures were printed. The same steps were applied in the construction of all samples. These steps are respectively; 3D drawing of the sample (nTopology software is used for TPMS structures), the output of the drawing with STL extension, importing STL files to Cura software and printing settings, cleaning unnecessary places such as skirts after the production of the sample, finally performing the test operation. First, ASTM 638D-TYPE 4 samples were produced for the quasi-static test sample. Since the cell has thin walls, this specimen was chosen to have the lowest thickness. The Type IV sample seen in the

Figure 2.3 was produced in the XY axis, and all the printer settings mentioned before were kept the same.

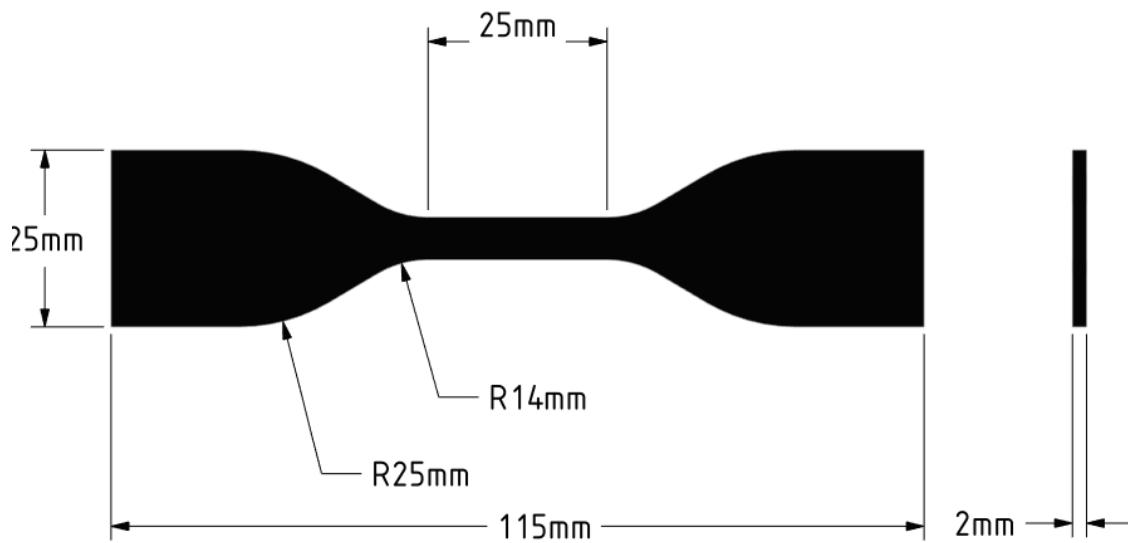


Figure 2.3. Dimension of tensile specimen

After the tensile tests, quasi-static and dynamic compression specimens were produced. First, 10x10x10 mm cubic specimens used for compression characterization tests were produced in the previous study, and then cylindrical specimens of 2 mm thickness and 12 mm diameter, seen in Figure 2.4, were produced due to the thin-walled design of the cell (Niezgoda and Wojtkowski 2013a). The sample height-to-diameter ratio was set to be below one to prevent potential buckling (Qi and Boyce 2005).



Figure 2.4. Compression cylindrical specimen used for material characterization

After the dynamic tests, the core structures were produced in two different planes, horizontally and vertically. However, to not use support in the production of the structures planned to be tested in the future, the single-cell and multi-cell structures that were printed later as shown in Figure 2.5 were printed only in the XY plane.

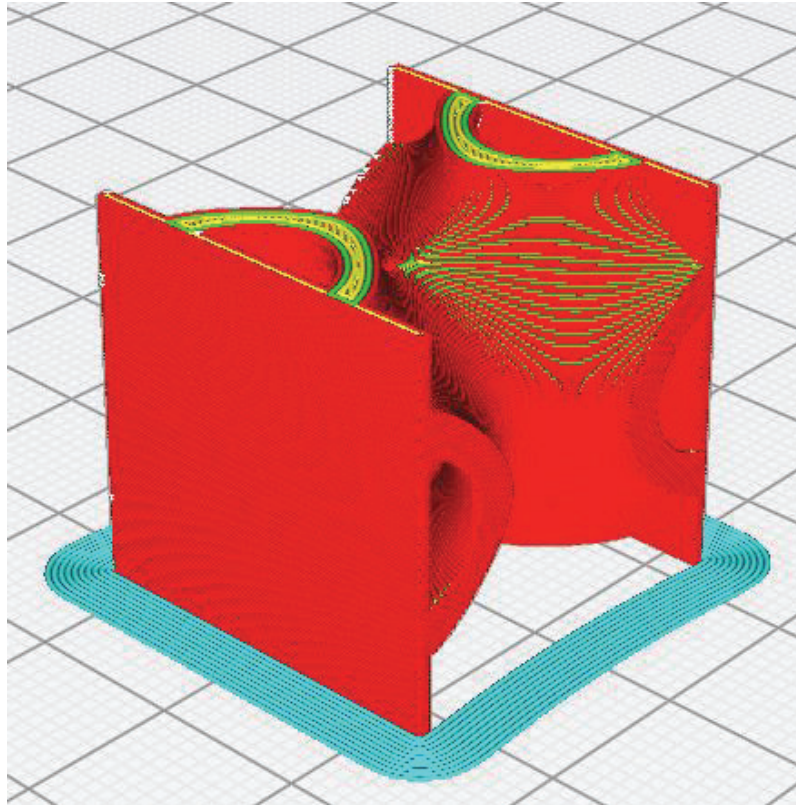


Figure 2.5. Single-core structure sliced in the Ultimaker Cura software to be produced on the XY plane

2.2. Material Characterization and Crushing Tests

Experimental methods used in this section are explained. Experimental methods were first performed to determine the strain rate-dependent behavior of TPU material and then to determine the energy absorption capacities of single-cell and multi-cell structures, respectively.

2.2.1. Quasi-Static Testing

Material characterization allows us to understand material properties and structures. Quasi-static tests are one of the most used test types in material characterization. In this study, the first tests were started with low strain rates. Then, the tensile and compression behavior of the TPU was demonstrated by quasi-static tensile and compression tests. One of the most popular hyperelastic materials, the data acquisition frequency in the tests was adjusted to reflect the material's behavior.

2.2.1.1. Tensile Test

As mentioned above, the quasi-static tensile test is one of the most common tests for material characterization. Quasi-static tests were carried out with a Shimadzu AG-X machine with a loading capacity of 300 kN. This machine is suitable for performing quasi-static tests at strain rates of 10^{-4} to 10^0 1/s. The values measured from stroke were verified with a video extensometer. In addition, a camera was used to observe the damage formation. The material's behavior at different strain rates was observed in this way. The tensile test was performed by ASTM standards for 10^{-3} and 10^{-2} 1/s strain rates. . Due to 3D printing, various cavities occur while producing the material. Therefore, different mechanical properties were observed even in the samples pressed repeatedly. Therefore, the tests were repeated until three comparative tests were obtained at each strain rate. Due to the extensometer's shooting angle limitation, the tests were terminated at 1.6 strains. Finally, the force vs. displacement values was read from the machine using TRAPEZIUM software.

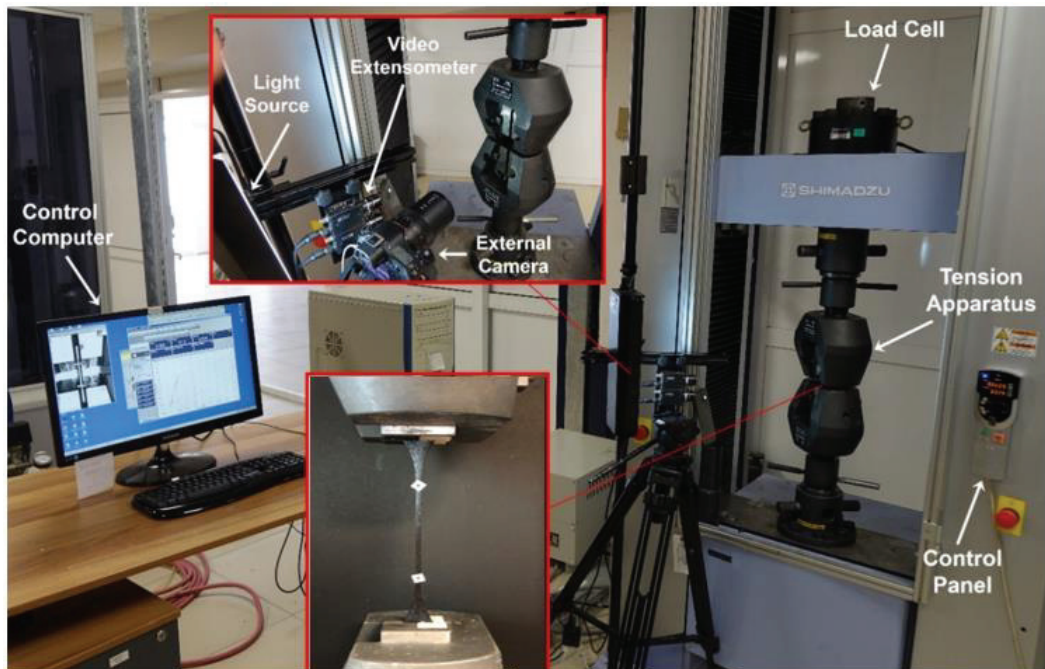


Figure 2.6. Quasi-static tension test set-up

2.2.1.2. Poisson's Test

In the Poisson's test, the same tensile test apparatus was used, and it was realized by reading the axial and transverse strains on the sample using 2D DIC. The crosshead velocity was selected as 5 mm/min by the ASTM 638D standard. Also, before starting the test, apply 0.1 mm pretension, and any bending stress effect on the sample is prevented.

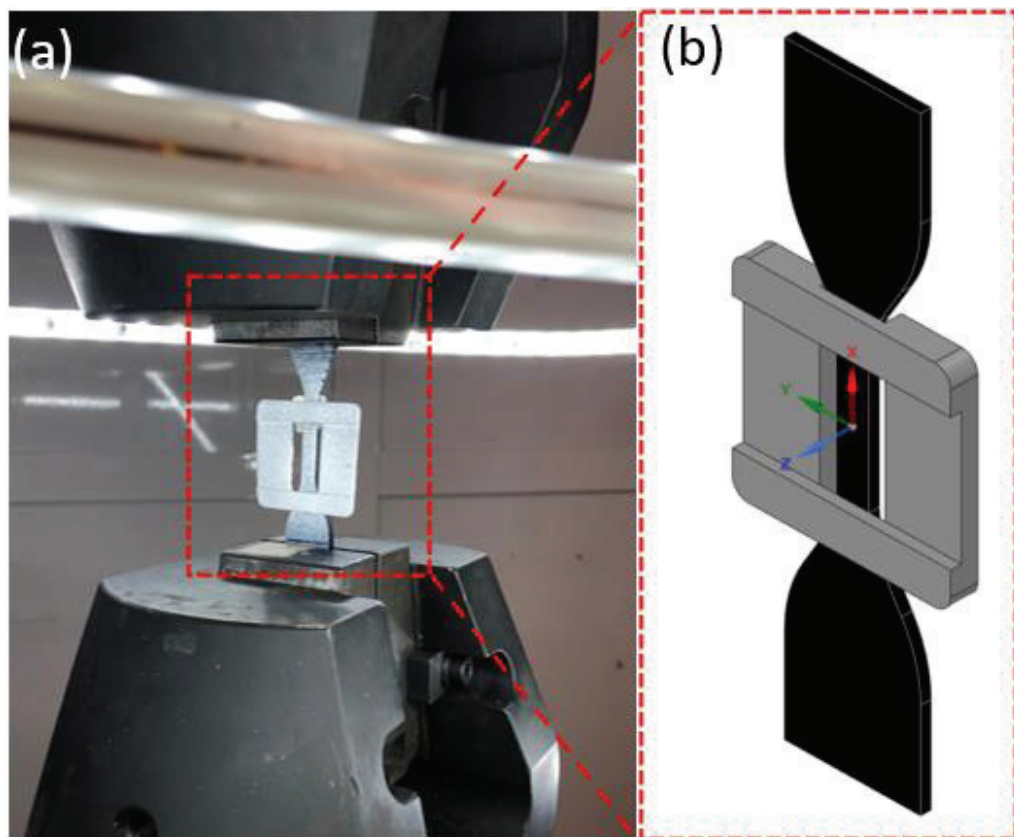


Figure 2.7. (a) Experimental setup of the Poisson's test (b) 3D Cad of the IV. Type specimen

It is pretty challenging to find the Poisson's ratio of soft materials such as TPU. So, mostly, strain gauges are adhered to the sample and read. However, it is challenging to stick the strain gauge on the sample because traces are formed along with the layer thicknesses on the samples produced with the 3d printer. It adds additional weight and stiffness to the sample. Instead, it has been seen in studies that it can be read non-contact in 2D DIC, and its accuracy rate is higher (Juang et al. 2021). The surface is divided into small pieces by applying contrast difference on the sample to be examined in DIC. The

displacement on the sample was obtained with the first image taken before the test started and then the images taken at regular intervals.

In order to prevent the errors that may occur due to the slip of the sample from the tensile axis, a piece containing the gauge length was produced from polyacid (PLA) material, and the test process was carried out with a TPU tensile sample produced with a 3D printer.

There are two blank areas on the sides of the mold that allow verification, and the PLA piece will only change place while the sample is changing shape. In this way, it is aimed to get more accurate results by subtracting the displacement value read on the sample from the displacement value read on the PLA piece. Video footage was shot at 1080p at 30fps.

2.2.1.3. Compression Test

Compression tests were carried out on a Shimadzu AG-X Universal testing machine with a -1 kN load cell and a Shimadzu AGS-X with a 300kN load cell at room temperature. The characterization and core samples were compressed between flat steel plates at constant strain rates of 0.001, 0.01, and 0.1 1/s to the point of full densification at the same rate. Tests were controlled and recorded using Trapezium X, the Shimadzu test. In addition, the deformation behavior of all the specimens was recorded using a video gauge that recorded the position at the plate surface using a speckle pattern on the face of the compression plates; this measurement was used to verify the positional location recorded directly from the test fixture. The sample was tested perpendicular to the production axis to reflect the compression properties as in core structures.

In this type of structure, the samples are compressed to approximately 80% of their original thickness (Laurin and Vizzini 2005). In this study, the samples are compressed to at least 70% of the thickness. Equation 2.1, where V_{ch} is the crosshead velocity of the machine, $\dot{\epsilon}$ is the strain rate for the specimen, and L_0 is the initial length of the cylindrical sample.

$$V_{ch} = \dot{\epsilon}L_0 \quad (2.1)$$

After the tests, the stress and strain values of TPU were calculated using the following equations

$$\sigma = P/A \quad (2.2)$$

$$\varepsilon = \Delta L/L_0 \quad (2.3)$$

where σ is the stress on the cylindrical sample, P is the force applied to it, A is the cross-sectional area of the sample, ε is the strain, ΔL is the amount the deformation of the sample and L_0 is the initial length of the sample.

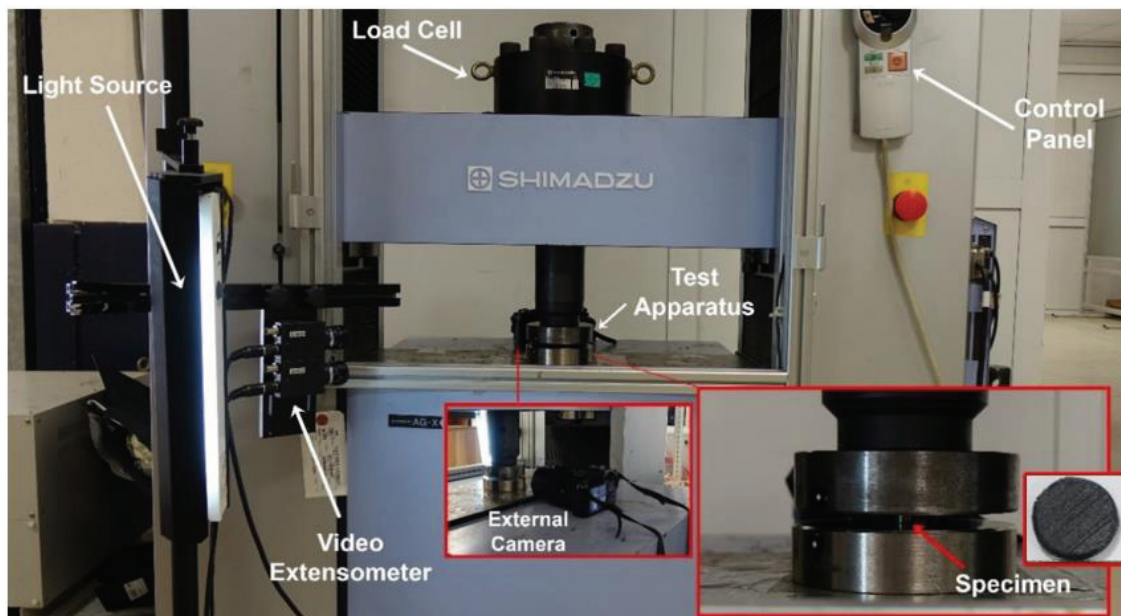


Figure 2.8. Quasi-static compression test setup

2.2.2. Dynamic Testing

Strain rate is a dynamical loading phenomenon related to constant widely used in various industrial fields (Siviour 2015). Strain rate sensitivity is a widely studied parameter in polymers produced with FDM (Rohbeck et al. 2020). TPU, on the other hand, has a high strain rate sensitivity like most thermoplastics. This strain rate sensitivity behavior is described in chapter 3. Then, it is explained in more depth. Due to the high

strain rate sensitivity of the material, it directly affected the energy absorption and deformation mechanisms.

Since the primary purpose of this study is to design an alternative energy-absorbing structure, the material's behavior under dynamic loading should be determined. As seen in Figure 2.9, strain rates between 10^0 - 10^4 are high strain rates. Therefore, SHPB and SHTB tests were performed to determine material characterization. In addition, drop weight and Direct Impact tests were performed with core structures.

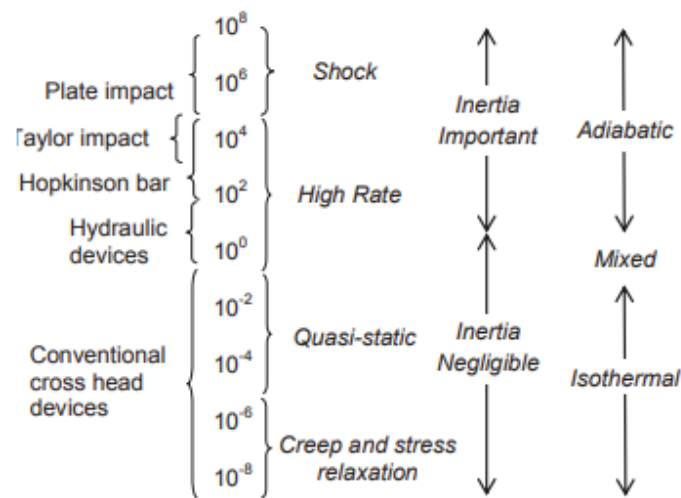


Figure 2.9. Experimental consideration at different strain rates
(Source : J.E. Field et al., 2004)

2.2.2.1. Direct Impact

The direct impact apparatus consists of 3 main elements: bar components, loading mechanism, and data acquisition system. In addition, piezoelectric quartz crystal was used in this test, which enables direct reading of the force applied to the bar surface with the sample. The schematic of the direct impact test setup is shown in the Figure 2.10.

Bar components have three different bars, but only two were used in this study. Striker bar size changes according to the determined velocity, 20 and 40 cm bar, 199 cm long incident bar, and 1 cm between sample and incident bar. Tests were carried out by placing a piezoelectric crystal between a cylindrical piece of the same material and the bars.

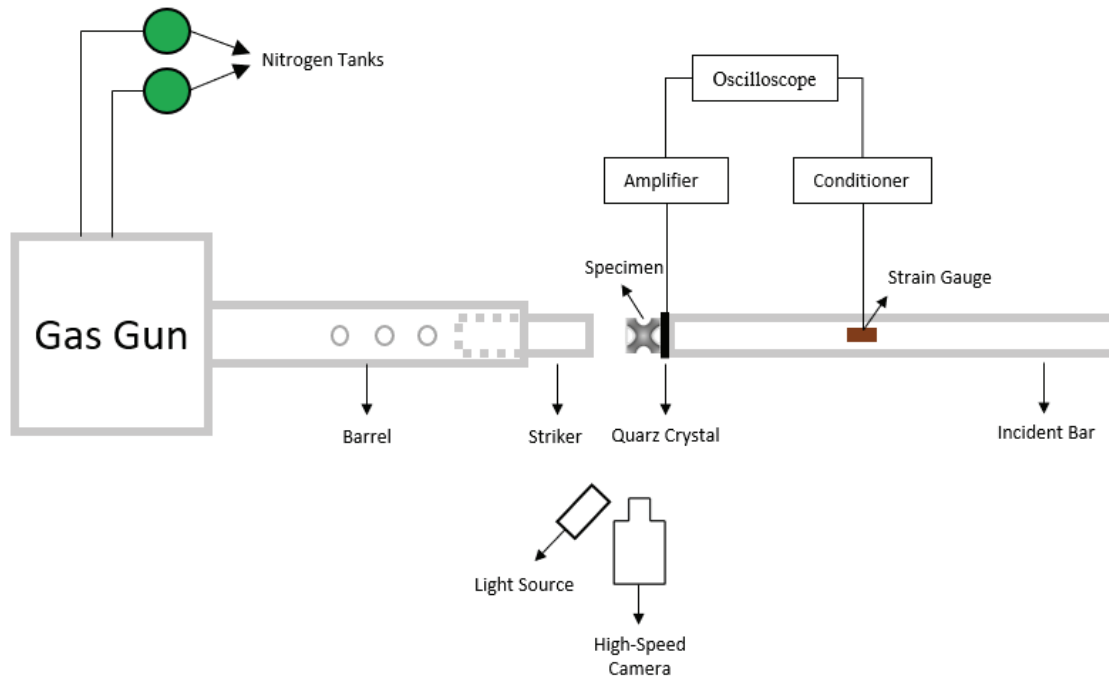


Figure 2.10. Schematic of Direct Impact Test

The material of all bars is 7075-T6 Aluminum, and their diameter is 40 mm. At the same time, they are all on the same axis, and teflon apparatuses are used to reduce the friction between their supports. The physical properties of aluminum 7075-T6 are listed in the Table 2.2. The gas gun system is used since a safe and controllable test procedure is provided. There are two nitrogen cylinders to store nitrogen gases in the system. First, the valves of the gases are opened, and the valves are opened on the gas day to fill them with gas at the desired pressure.

To start the test, when the valve of the gas gun is opened, As a result of the rapid release of the gas, the striker standing next to the valve starts to move and moves along the barrel. The initial velocity of the striker bar was read and verified with the ImageJ program from the image recorded with a two-point laser optical measuring device and a high-speed camera. Conditioner 200 gain, and It was set to 10V excitation voltage. Tektronix MD03024 Mixed Domain Oscilloscope was used.

A piezoelectric quartz crystal (an X-cut quartz crystal disc) of the same diameter placed between the sample and the bar surface was used to measure the Crushing Force. This technique was preferred because quartz crystal has more sensitive force transducers than strain gauges.

Table 2.2. Mechanical properties of the aluminum 7075-T6

PHYSICAL PROPERTIES	VALUES
Elastic Modulus	71.7 GPa
Density	2810 kg/m ³
Poisson's Ratio	0.3

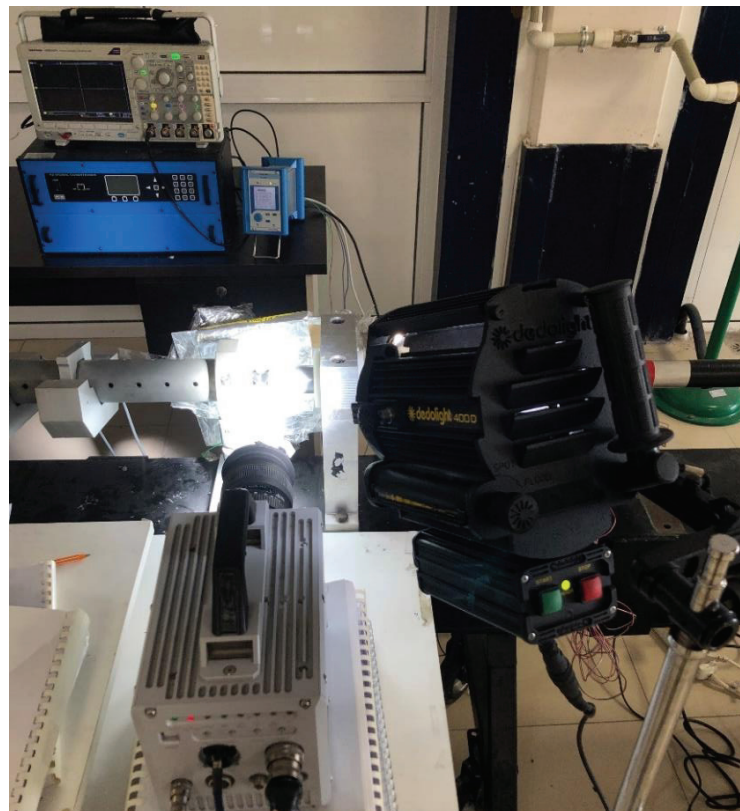


Figure 2.11. High speed camera and flashlight of the direct impact test

Since the mechanical impedance of the quartz crystal is very close to the mechanical impedance of the aluminum bars, it is prevented from affecting single-dimensional wave propagation (Chen, 1999). Piezoelectric quartz crystal could also be placed directly between the sample and the bar. However, rubber-like materials such as TPU may damage the crystal during axial compression. In order to avoid expensive and inconsistent tests, it was preferred to be placed between the aluminum disc and the bar. A 40 mm diameter and 0.254 thick crystal from Boston Piezo Optics were used. In order to read the voltage value with an oscilloscope, Kistler Solo A Amplifier was used. To fix

the sample horizontally on the bar surface, Double-sided tape passing through the middle of the sample was used. This detail needs attention while creating the numerical model in the next chapter.

The prepared test setup is shown in the figure. The deformation of the sample and the movement of the bar were recorded with the help of a Fastcam SA1.1 high speed camera and Dedolight Daylight 400D light source. The direct impact test setup used in dynamic testing of unit cell structures is represented in Figure 2.12.



Figure 2.12. Direct impact test setup

2.2.2.2. Drop Weight Test

In this study, the drop test was performed to determine the energy absorption behavior of multi-core structures. In addition, the characteristics of the structure in axial and low-velocity impact loads were observed. Fractovis Plus drop weight device was used to perform this test. It consists of weights, an optical speed sensor, and a stationary bottom plate fully fixed to the base. In this test, the kinetic energy required to crush the designed

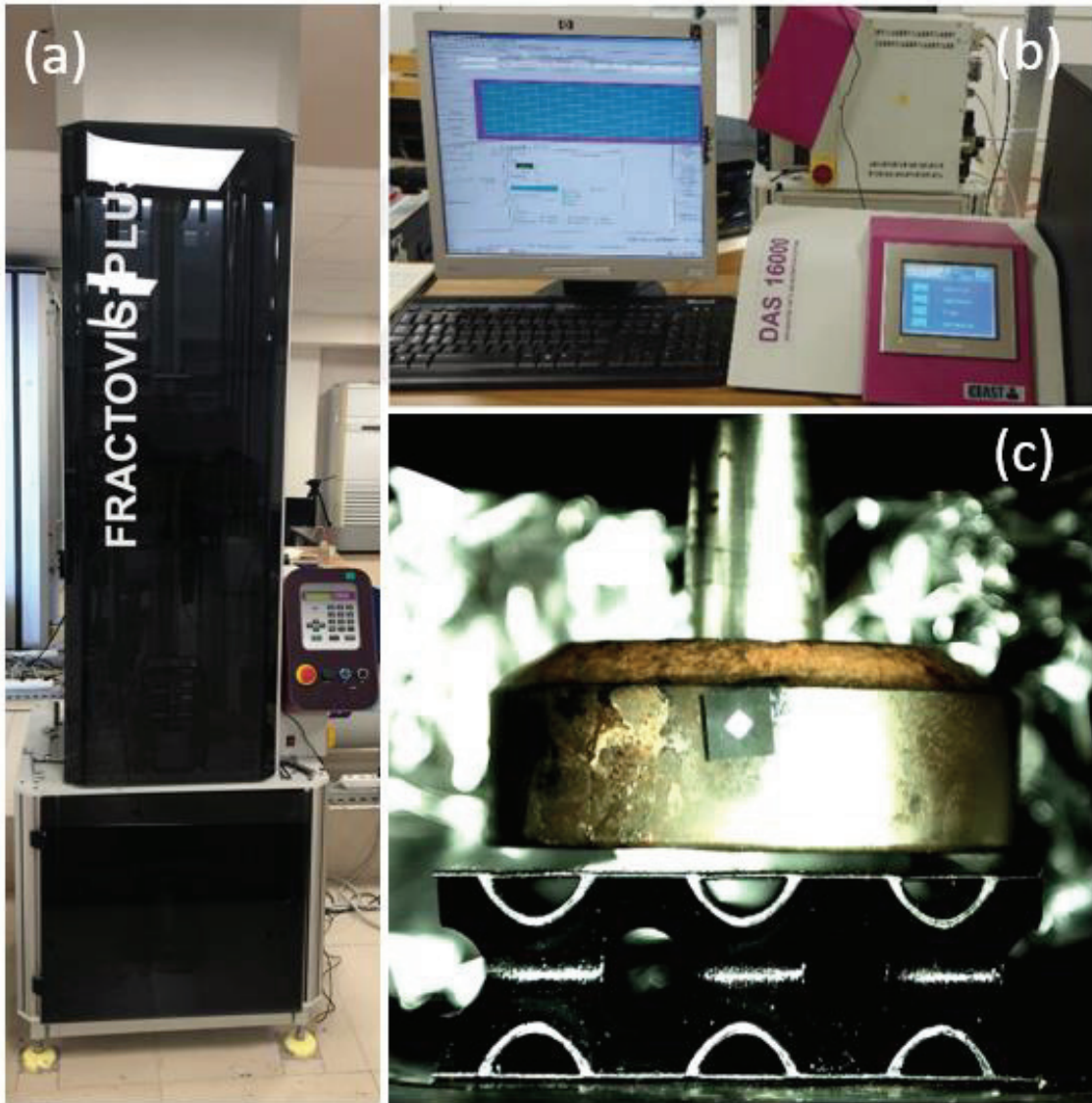


Figure 2.13. (a) Drop Weight Test Setup (b) DAS 16000 (c) Impactor and multi-cell structure

multi-cell structures up to 80% of the structure was determined according to the weight added to the structure and the desired velocity. Although the speed could be measured from the optical velocity damper, it was also verified with a high-speed camera. The desired strike velocity was calculated from the potential and kinetic energy conversion.

Equation 2.5 is obtained by analyzing the Equation 2.4 below, and in this way, the device automatically adjusts the height to which the weight will be dropped according to the desired velocity value.

$$\frac{1}{2}mv^2 = mgh \quad (2.4)$$

$$\sqrt{2gh} \quad (2.5)$$

Where V is impact velocity, g is the gravitational acceleration, and h is the drop height.

DAS 16000 works integrated with the drop weight device, an advanced data acquisition system. In this way, force and displacement values are read and recorded depending on time. They recorded the deformation of multi-core structures under dynamic loads and verified the velocity with a high-speed camera and light source. The force-displacement taken from the device was later verified with a camera, and the energy absorption capability of the structure was determined with this curve. Since the thickness of the cylindrical sample used for characterization is 2 mm, this machine was not used to avoid any damage to the device during the test.

2.2.2.3. SHPB Test

In order to determine the strain rate sensitivity of TPU produced with a 3D printer, tests were carried out at strain rates between 10^2 and 10^4 1/s. In general, the Split Hopkinson Pressure Bar (SHPB) apparatus; consists of a striker bar, an incident bar, and a transmitter bar. During the additional test to the test apparatus, the video was tried to be taken with a high-speed camera, but the video could not be achieved due to the thinness of the sample. Therefore, Vascomax C350 steel was used for all bars to reduce impedance

mismatch and not affect wave propagation. The. The table lists the mechanical properties of Vascomax C350 steel.

Table 2.3. Mechanical properties of the Vascomax C350

PHYSICAL PROPERTIES	VALUES
Elastic Modulus	180 GPa
Density	8100 kg/m ³
Poisson's Ratio	0.3

The diameter of the incident and transmitter bar is 19.2 mm, and the length of the bar is 1200 mm. 20 mm striker bar is used. As in the direct impact test setup, when the air in the gas gun moves the striker bar, a rectangular incident stress pulse occurs when the striker bar hits the incident bar. This pulse moves over the incident bar until it reaches the sample. A part of the incident pulse is transmitted to the transmitter bar due to an impedance mismatch over the sample. The other part is transmitted back to the incident bar from the sample surface with the bar.

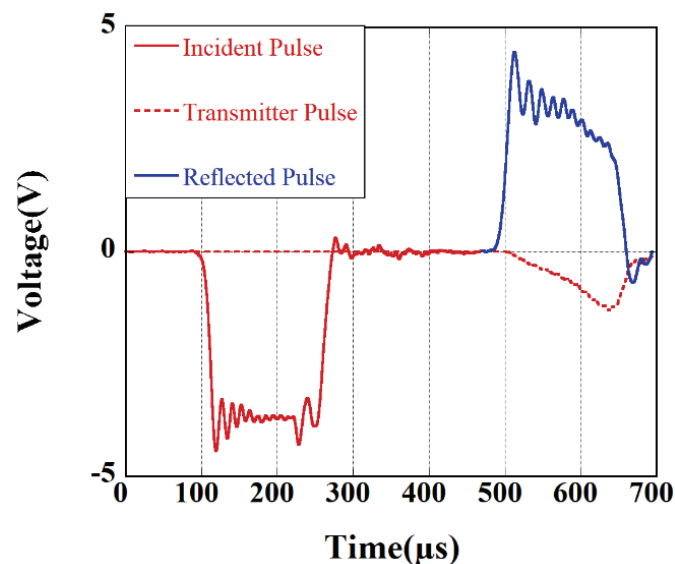


Figure 2.14. A typical voltage vs. time curve of a SHPB test of 3D printed

Meanwhile, elastic strain values from strain gauges equidistant from sample and bar surfaces are read from the oscilloscope with the help of a conditioner. With the excitation voltage and gain values set by the Conditioner, the signals coming from the

strain gauge are read from the oscilloscope correctly. Then, the data taken from the oscilloscope is converted into strain, stress, and strain rate data with the formulas to be explained below. Since these data are recorded as a function of time, the strain rate is found from the slope of the strain vs. time graph created. The bar response curves of a sample TPU sample are shown in the Figure.

For the test to be valid, the yield strength of the bars must be greater than that of the sample. An elastic stress wave occurs on the incident bar when the striker bar hits the incident bar. This elastic wave velocity is demonstrated by Equation 2.6, where E elastic modulus, ρ is the density of the material.

$$c = \sqrt{\frac{E}{\rho}} \quad (2.6)$$

The formulas in which the wave propagation and strain occurring in the SHPB test are explained as a function of time are given below.

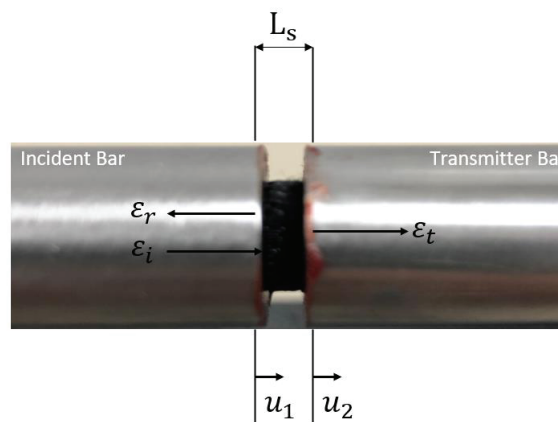


Figure 2.15. Schematic of specimen and waves

The formulas in which the wave propagation and strain occurring in the SHPB test are explained as a function of time are given below. In the Figure 2.15, the interfaces between the incident bar and specimen are shown with notation 1, and the forces between the transmitter bar and specimen are shown with notation 2. Therefore, the forces on the incident bar and transmitter bar are shown in Equation 2.7 and 2.8.

$$F_1 = A_b E_b (\epsilon_i + \epsilon_r) \quad (2.7)$$

$$F_2 = A_b E_b (\varepsilon_t) \quad (2.8)$$

Where A_b is the cross-sectional area and E elastic modulus of the bars, in the validated SHPB test, the forces on the sample and both bar surfaces are considered equal. Therefore, when the equilibrium of the forces Equation 2.7 and Equation 2.8 are equalized, Equation 2.9 is obtained.

$$\varepsilon_t = \varepsilon_i + \varepsilon_r \quad (2.9)$$

Then, the average force above the specimen is obtained in Equation 2.10. After solving it by writing Equation 2.7 and Equation 2.8 instead, the average stress equation is obtained as Equation 2.11.

$$F_{avg}(t) = \frac{F_1(t) + F_2(t)}{2} \quad (2.10)$$

$$\sigma_{avg}(t) = \frac{\pi D_b^2}{2} E [\varepsilon_i(t) + \varepsilon_r(t) + \varepsilon_t(t)] \quad (2.11)$$

The incident and transmitter bar displacements in Figure 2.15 are shown in Equation 2.12 and Equation 2.13, respectively.

$$u_1(t) = c_b \int_0^t [\varepsilon_i(t) - \varepsilon_r(t)] dt \quad (2.12)$$

$$u_2(t) = c_b \int_0^t [\varepsilon_t(t)] dt \quad (2.13)$$

The specimen's strain is obtained by subtracting Equation 2.13 from Equation 2.12 and dividing by the initial length of the sample, shown in Equation 2.14.

$$\varepsilon_s(t) = \frac{u_1 - u_2}{L_s} = \frac{c_b}{L_s} \int_0^t [\varepsilon_i(t) - \varepsilon_r(t) - \varepsilon_t(t)] dt \quad (2.14)$$

In order to obtain the specimen strain rate, the time derivative of Equation 2.14 is obtained as in Equation 2.15.

$$\dot{\varepsilon}_s(t) = \frac{c_b}{L_S} [\varepsilon_i(t) - \varepsilon_r(t) - \varepsilon_t(t)] \quad (2.15)$$

$$\varepsilon(t) = \frac{2V(t)}{V_e \times K_{gain} \times GF \times (1 + \nu)} \quad (2.16)$$

Equation 2.16 is used to convert the voltage signals read from the strain gauges on the bar to strain values. In the formula, V_e , K_{gain} , GF , ν are abbreviated as excitation voltage, gain factor, strain gauge factor set in the conditioner, and Poisson's ratio of bars, 10 Volt, 200, 2.16, 0.3, respectively. Test setup of the SHPB is represented in Figure 2.16.



Figure 2.16. Test setup of the Split Hopkinson Pressure Bar

CHAPTER 3

NUMERICAL METHODOLOGY

The finite element method (FEM) is a numerical method used for solving physical or mathematical problems. The application areas of FEM include structural analysis, fluid flow, heat transfer, and electromagnetic fields.

It is impossible to find solutions with the classical method for complex geometries, boundary conditions, and nonlinear materials. Therefore, it can be solved using simultaneous algebraic equations instead of partial differential equations (PDE) or ordinary differential equations (ODE) that need to be solved thanks to FEM. This numerical method has been developed to determine solutions with a certain degree of accuracy. The classical method, which is solved using the PDE as mentioned earlier, is thanks to the meshing of the geometry, called discretization, which is divided into small parts and turns into matrix equations to be solved with the help of computers. Calculations are made separately for each divided element. Then combine these results. By doing this, the desired results of the structure are resolved. In Figure 3.1, the discretization state of the structure is shown.

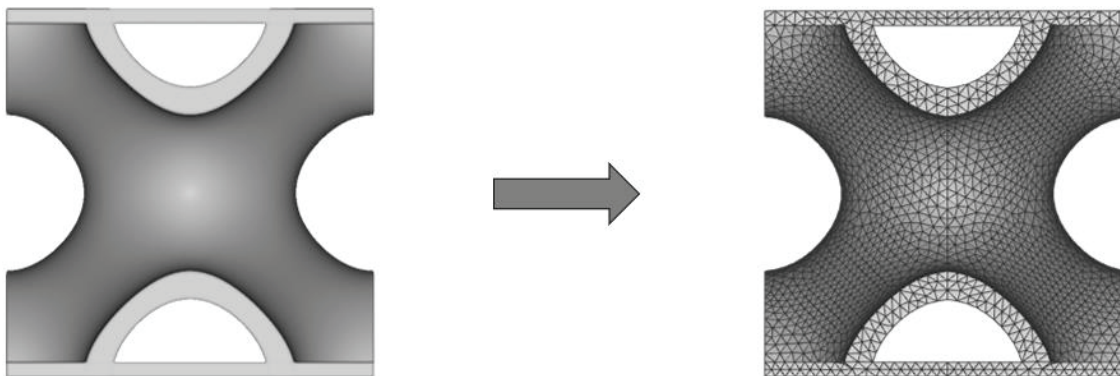


Figure 3.1. The discretization of the TPMS structure in nTopology software

In this study, volume meshing was performed for nTop in order to perform the finite element analysis of the cell structure, which was first designed with the help of nTopology for modeling. The mesh file obtained from here was integrated into the Ls-Dyna software, where the analysis will be performed. The prepared models are Ls-Dyna Solver and the desired results are displayed with Ls-PrePost. Previously performed tests

and numerical model results are compared. The modeling schematic used in this study is shown in Figure 3.2.

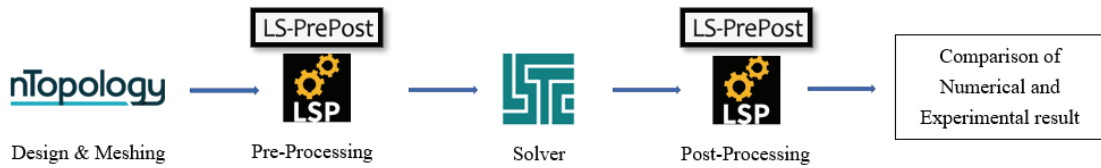


Figure 3.2. Numerical methodology

Ls-Dyna is one of the most powerful programs used to solve explicit analysis. Therefore, it is frequently used in fields that require more than one nonlinearity, such as military, space, production, and automobile. Large deformation, not ideal elastic material behavior (such as TPU), and non-constant and time-varying boundary conditions create nonlinearity. Although Ls-Dyna is generally used for explicit analysis, its recently developed features can be used for implicit analysis.

To explain briefly from the explicit and implicit analysis;

In implicit analysis, the time variable is constant. Therefore, the analyzes are solved as shown in the simple linear Equation 3.1, where K is the stiffness matrix, and x is the displacement.

$$[K]\{x\} = \{F\} \quad (3.1)$$

On the other hand, a more complex governing equation in an explicit analysis is solved using the mass matrix, where M is the damping matrix, \dot{x} is the first derivative of displacement, and \ddot{x} is the second derivative of the displacement, shown in the following equation.

$$[M]\{\ddot{x}\} + [C]\{\dot{x}\} + [K]\{x\} = \{F\} \quad (3.2)$$

The time step is much larger than in the explicit solution in the implicit solution. In this way, faster simulations can be performed. However, this method causes convergence problems, and unstable solutions can be obtained.

In the explicit solution, the time step is calculated with the smallest element and the wave velocity of the material. Therefore, a much smaller time step is chosen compared to the implicit analysis to avoid convergency and instability.

The explicit time integration uses past configurations to derive a direct solution when solving the equation of state for the next timestep. In this way, convergence problems are not encountered. Implicit and explicit time integration calculation formulas are given below, respectively.

$$x_{n+1} = f(x_n, x_{n-1}, \dots, t_{n+1}, t_n, \dots) \quad (3.3)$$

$$0 = f(x_{n+1}, x_n, \dots, t_{n+1}, t_n, \dots) \quad (3.4)$$

This study used the implicit method to model the crushing behavior of single and multi-core structures in quasi-static conditions. The explicit method was used to model their behavior in dynamic conditions. First, the experimental tests obtained stress-strain curves at specific strain rates, and then numerical models were used. It is aimed to predict the crushing behaviors of TPMS core structures.

3.1. Available Material Models in Ls-Dyna

Many material models are used for soft materials such as rubber in ls dyna. MAT_27(MAT_MOONEY-RIVLIN_RUBBER) and MAT_181 (MAT_SIMPLIFIED_RUBBER) only require uniaxial test curves. Some are relatively complex and require more test data to be entered pure shear and Require all tension and compression curves to be defined as input.

The accuracy of the material model is directly related to the accuracy of the test. Therefore, hyperelastic material models such as MAT_27, MAT_31 (MAT_FRAZER_NASH_RUBBER), and MAT_77(Ogden) mentioned in the studies were compared, and it was found that MAT_77, which contains the most parameters, gives more accuracy(Finney and Kumar 1988; Charlton, Yang, and Teh 1994).

MAT_181 is an Ogden-based material model and easily reflects the strain rate sensitivity of the material. In this study, MAT_181 was used in the modeling of all test

setups, and it was compared with MAT_27 in terms of being an alternative in quasi-static test modeling. The following table shows which material cards are used to model the tests.

Table 3.1. Summary of numerical models

	1 Cell QS	9 Cell QS	1 Cell DI	4 Cell DW	9 Cell DW	Blast
MAT_27	✓					
MAT_181	✓	✓	✓	✓	✓	✓

3.2. Material Model Selection

The use of 3D printed parts in many industrial areas increases day by day. As a result, the popularity of 3D printing of hyperelastic materials such as TPU is also increasing. Material selection is crucial for modeling the behavior of this type of material at different strain rates and under high deformation (Ursini and Collini 2021). Although the obtained part is anisotropic due to the nature of the product with the .3D printer, in this study, the voids in the samples, the layer by layer production method, and the residual stresses caused by this were neglected, and the sample was modeled and examined as if it were a bulk material.

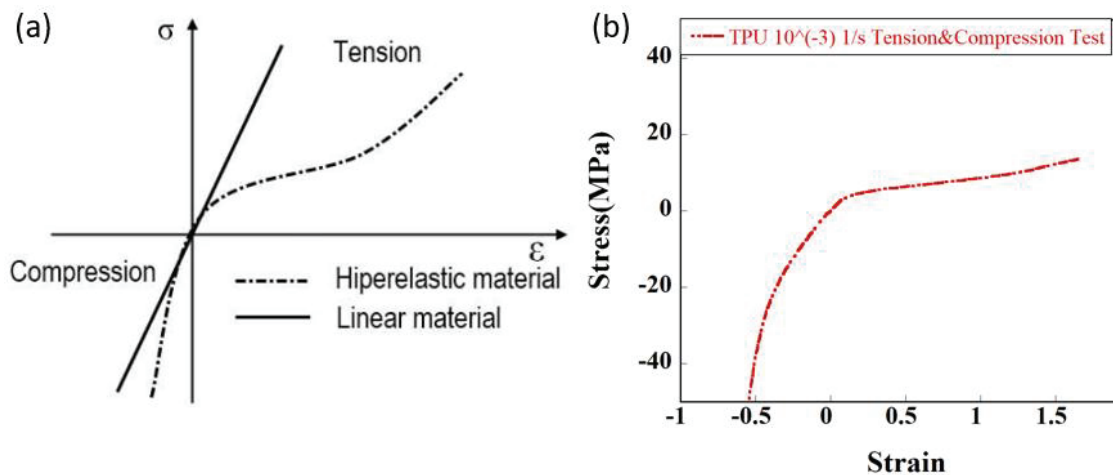


Figure 3.3. (a) Typical hyperelastic material's stress-strain curve (Source: ANSYS, 1999) (b) 3D Printed Stress-strain curve of 3D printed TPU material

Since the deformation of core structures under impact loads will be examined, the MAT_181 material model, which considers the strain rate sensitivity effect, has been used to model rubberlike materials in many studies. It has been accepted that the sample has

not suffered any perpetrators, and no damage parameter has been defined (Baranowski et al. 2013). Their constitutive relationship between stress-strain is due to a nonlinear elastic theory called hyperelasticity (Mooney 1940; ANSYS 2002). Since TPU is nearly or fully incompressible, and its stress-strain response is highly nonlinear, choosing a hyperelastic material model approach was deemed appropriate. The stress-strain curve of the TPU test performed at 10^{-3} strain rate in Figure 3.3 shows an ideal hyperelastic material. The sample is compared with the stress-strain curve, and its similarity is shown.

3.2.1. Mooney Rivlin Rubber (MAT_27)

This material card is used for modeling rubber and rubber-like materials with 2 parameters. Although strain rate sensitivity effect will be considered in this study, quasi-static strain rates are used as an alternative material model. This material card is solved with strain energy density function (W). However, by setting the gauge length, thickness and width option to 1 in the material card, the engineering stress-strain curve containing the tension and compression region to be defined can be easily used and fitted with the least square during the initialization phase (LSTC, 2021).

*MAT_MOONEY-RIVLIN_RUBBER_(TITLE) ((null)) (0)

TITLE
3D Printed TPU

1	MID	RO	PR	A	B	REF
	1	1.02E-9	0.42			0.0
2	SGL	SW	ST	LCID		
	1	1	1	<input type="radio"/>		

Figure 3.4. MAT_027 material model keyword

The file with the d3hsp extension was checked to compare the entered input curve and the fitted values. Unfortunately, as the strain values increase, the fit will become more difficult due to the increase in the slope of the input curve.

Therefore, as the strain value increases, it will be difficult to predict the experimental results with this material model, as shown in the figure. Also, MAT_27

Since it does not include strain rate effect, it is not used in direct impact, drop weight and blast modeling.

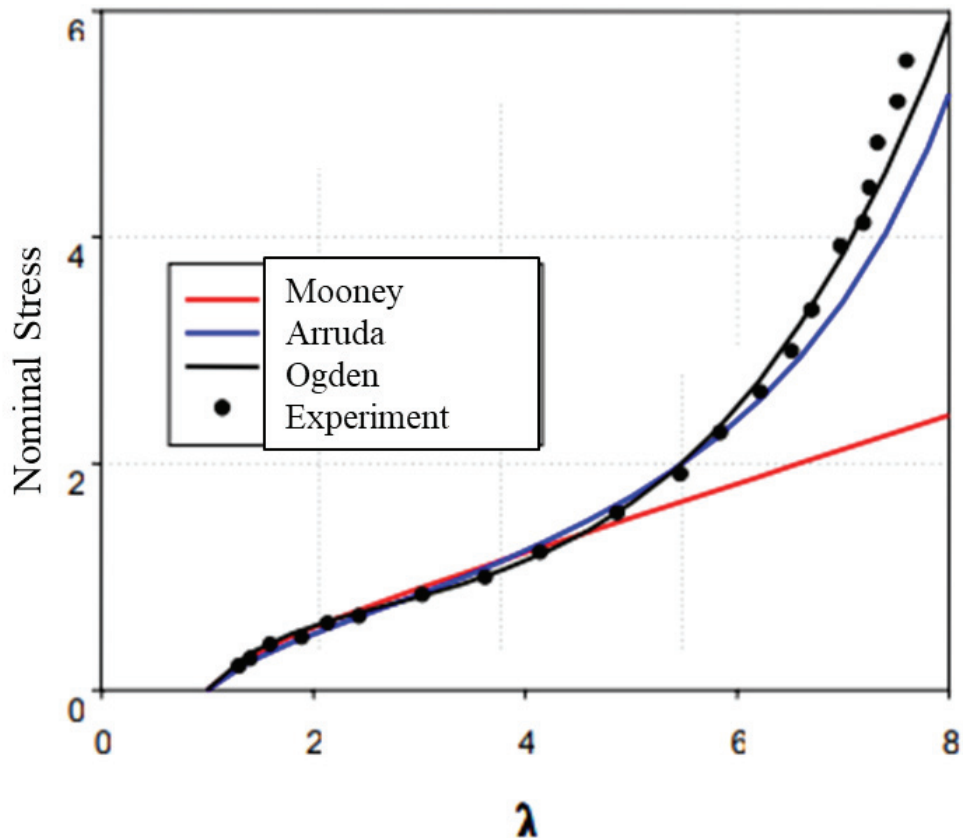


Figure 3.5. Comparison of hyperelastic material models
(Source : ANSYS, 2002)

3.2.2. Simplified Rubber (MAT_181)

MAT_181 is a material card used for rubber and foams. It is a material model that can be used directly without a fitting to find any parameter by entering curves at multiple strain rates. This model is the tabulated version of Ogden(MAT_77).

To account for the strain rate effect, when more than one curve is defined in the material model, stress values at intermediate strain rates are found by linear interpolation. Thus, it was sufficient to define tabulated stress-strain curves as in FIGURE, without the need for a new test for each different strain rate(LSTC, 2021).

As shown in the Figure above at 10^{-3} , 10^{-2} , 10^{-1} , 4157 s^{-1} compression engineering stress-strain curves at strain rates and tensile test curves at 10^{-3} , 10^{-2} ,

10^{-1} s^{-1} strain rates are tabulated, specimen length,width and height is set to one as in MAT_27, then tabulated. The other parameters used in the model are shown in the Table 3.2.

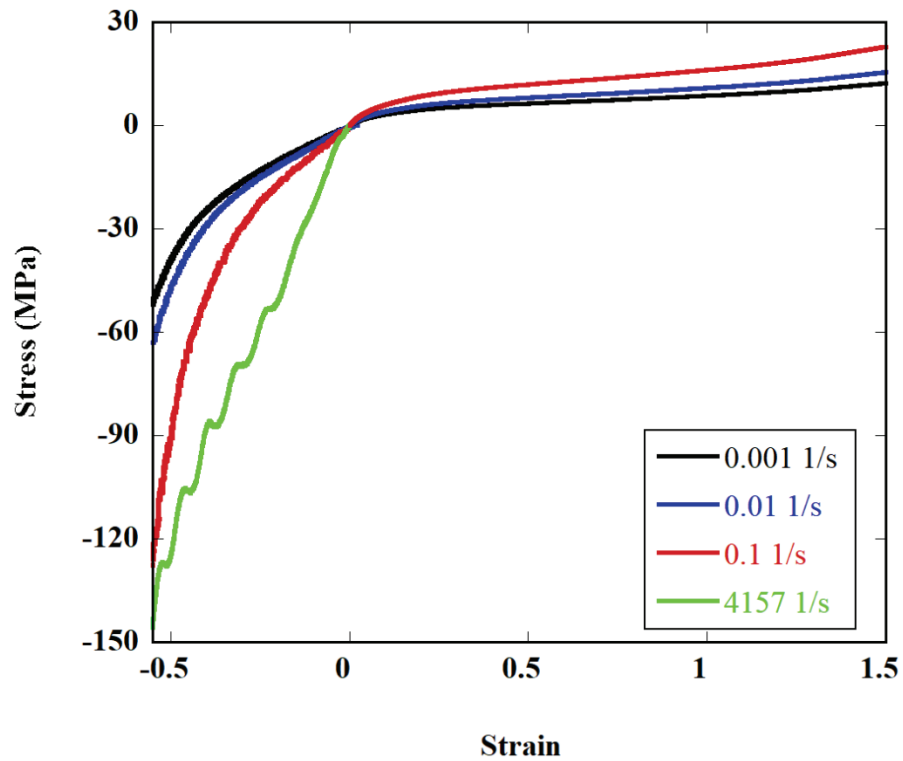


Figure 3.6. Ls-Dyna MAT_181 Table Input

Table 3.2. Material model constant

Symbol	Information	Value
RO	Density	1.02E-9 tonne/mm ³
KM	Linear Bulk Modulus	50 MPa
MU	Damping Coefficient	0.1
SGL	Specimen Gauge Length	1
SGW	Specimen Width	1
ST	Specimen Thickness	1
TBID	Table ID or Load Curve	Table
RTYPE	Strain Rate Type	0
AVGOPT	Curve Average Option	1

In Hyperelastic materials, strain values are often over 100%, and after this value, the expression stretch(λ) is used instead of strain. $I_{1,2,3}$ strain invariant in terms of stretches defined as ;

$$I_1 = \lambda_1^2 + \lambda_2^2 + \lambda_3^2 \quad (3.3)$$

$$I_2 = \lambda_1^2 \lambda_2^2 + \lambda_2^2 \lambda_3^2 + \lambda_3^2 \lambda_1^2 \quad (3.4)$$

$$I_3 = \lambda_1^2 \lambda_2^2 \lambda_3^2 \quad (3.5)$$

Where a_{ij} is non-intager, K is the bulk modulus, $\lambda_i^{-1} = \lambda_i J^{-1/3}$ and $J = \lambda_1 \lambda_2 \lambda_3$ shown in the equation 3.6 below (Ogden,1984);

$$W = \sum_{i=1}^3 \sum_{j=1}^n \frac{\mu_j}{\alpha_j} (\lambda_i^{*\alpha_j} - 1) + K(J-1 - \ln J) \Rightarrow \sigma_i = \sum_{p=1}^n \frac{\mu_p}{J} \left[\lambda_i^{*\alpha_p} \sum_{k=1}^3 \frac{\lambda_k^{*\alpha_p}}{3} \right] + K \frac{J-1}{J} \quad (3.6)$$

Since MAT_181 is also a material model based on Ogden, equation 3.7 is simplified and determined by defining the primary stretch ratio in a table as follows (Baranowski et al. 2013; LSTC 2005);

$$f(\lambda) = \sum_{p=1}^n \mu_p \lambda^{*\alpha_p} \Rightarrow \sigma_i = \frac{1}{J} \left[f(\lambda_i) - \frac{1}{3} \sum_{j=1}^3 f(\lambda_j) \right] + K \frac{J-1}{J} \quad (3.7)$$

3.3. Validation Numerical Models

In this section, the SHPB test made for the dynamic characterization of the base material used and the single element model prepared for its validation are included.

3.3.1. Single Element Compression

It is based on comparing the stress-strain curve defined in the material model with the experimental data by reading the data from a single element after the fitting process. In this way, it is aimed to verify the material model with the test. Moreover, it is a faster

and more convenient method than wasting time on the full model. Since both implicit and explicit analysis will be used in test models, a single element model has been established and compared with both types of analysis

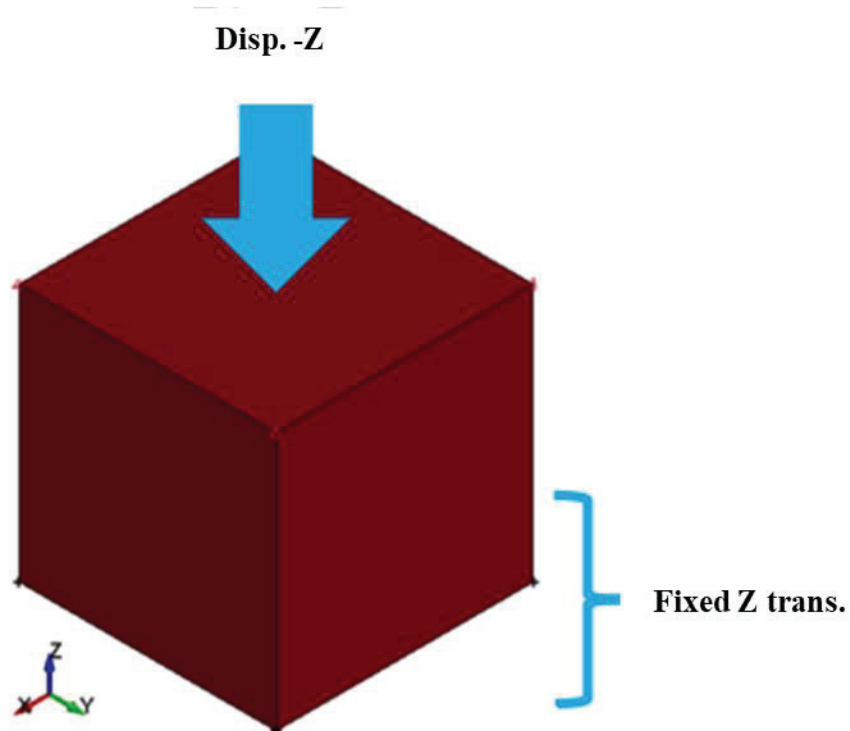


Figure 3.7. Boundary and initial conditions of single element model

As shown in Figure 3.7, reduced-order element was used, and ELFORM 1 element formulation was selected. Translational constrain was given to the four nodes at the bottom of the Z-axis, and a displacement was defined in the +Z direction to the four nodes on the upper surface of the element with PRESCRIBED_MOTION_SET.

3.3.2. SHPB

Explicit solver is used in modeling of SHPB test. As shown in the figure, incident, transmitter bar, and sample are modeled, and incident bar response is defined with SEGMENT_LOAD keyword on the surface of the incident bar instead of the striker bar.

The purpose of modeling this test is to ensure that the input curve is output, as in the single element model, and to understand that the model considers rate sensitivity with tabulated curves defined in the MAT_181 material model.

In order to determine the strain gauge points in the model, the incident and transmitter bar are modeled in 2 different parts, the node is shared with the duplicate node, and the integrity of the bars is not broken.

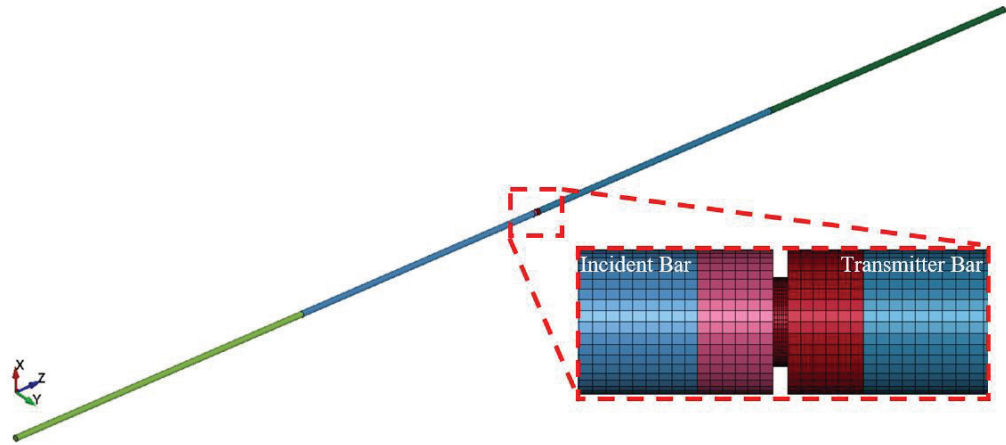


Figure 3.8. Numerical model of the SHPB test

Z axial stresses were taken from the elements at these points and compared with the bar response graph in the test. Material model MAT_181 for TPU sample and material properties of Vascomax 350 steel shown in Table 2.3 for bars were defined to material model MAT_001(MAT_ELASTIC).

CONTACT_AUTOMATIC_SURFACE_TO_SURFACE was used between the bars and the sample, and the CONTACT_AUTOMATIC_SINGLE_SURFACE contact formulation was used with the SOFT=2(segment-based) option to see the interaction between the sample's walls. In this way, it is aimed to avoid penetrations that may occur due to the mesh density difference between the sample and the bar surfaces. The contact stiffness is calculated based on the actual timestep in this option.

$$k = SLSFAC \langle SFS \text{ or } SFM \rangle 0.5 \left(\frac{m_1 m_2}{m_1 + m_2} \right) \left(\frac{1}{\Delta t_0} \right) \quad (3.8)$$

The contact stiffness is shown in equation 1, where SLSFAC(0.3) is the penalty stiffness, SFS(5) is the slave side stiffness factor or stiffness factor for the master side in SFM, and m1 and m2 are the masses of the segments.

Static and dynamic friction 0.67 and 0.65 were used, respectively (Platek et al., 2020). By using VDC(viscosity damping coefficient) = 20(%), it is aimed to prevent vibrations on the contact surfaces due to the stiffness difference of the materials of the specimen and bars.

3.4. Numerical Modeling of Dynamic And Static Tests of Core Structures

In this section, the modeling of the tests performed to observe the deformation history of the unit and 9-cell structure with numerical methods is included. In addition, numerical modeling of the blast loading scenario, which is one of the intended application areas of the structure, is included.

3.4.1. Static Compression

An implicit solver was used in the modeling of the quasi-static test. In modeling rubber-like materials, it is generally recommended to use type 7 with QM=0.01 or to use a tetra element to avoid hourglass problems in high deformation. Therefore, ELFORM 13, a first-order tetrahedral element formulation, was used, unlike the tests performed to validate characterization tests. In addition, this element formulation was used to prevent the complexity of geometry and contact instability in implicit analysis (LSTC 2012).

In addition, studies show that when sufficient mesh density is provided with ELFORM 13, at least as much accuracy as hex element, although the solution is not as fast as hex element (Bondy 2013). Therefore, mesh sensitivity analyzes were performed to determine the optimum mesh amount. As can be seen in Figure 2, it was decided to use 0.7 mm mesh element size as a result of the numerical analysis.

In order to perform implicit analysis in Ls-Dyna, IMFLAG was set to 1 in CONTROL_IMPLICIT_GENERAL, and the IGS = 2 option was used to help turn off the geometric stiffness effect. Then, the CONTROL_IMPLICIT_SOLUTION keyword was used to determine the convergence tolerance of the model and the solution method to be used. Next, by using CONTROL_IMPLICIT_AUTO, IAUTO was set to 1 to automatically decrease the timestep size of the model when it could not converge. Finally, the GAMMA and BETA options in the CONTROL_IMPLICIT_DYNAMICS keyword,

offered as suggestions in the studies, were set to 0.6 and 0.38, respectively. The keywords and values used for implicit analysis are given below.

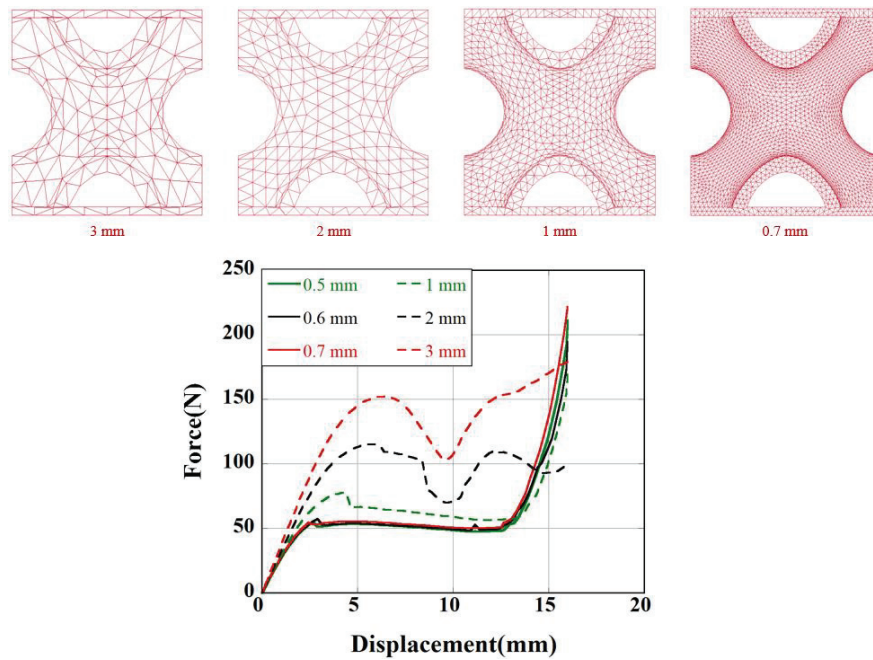


Figure 3.9. Mesh sensitivity of cell structure

In the implicit analysis, the MORTAR options of the CONTACT keywords, which were also used in SHPB before, were used. Also, MINFO = 1 for the CONTROL_OUTPUT keyword to observe the contact penetrations. As mentioned before, MAT_27 and MAT_181 material models were used in the quasi-static core structure test models. In addition, the material model MAT_RIGID(MAT_020) was used for the movable upper and fixed lower heads.

Table 3.3. Implicit keywords and constants

	Value	CONTROL_IMPLICIT_Keyword
IAUTO	1	AUTO
GAMMA	0.6	DYNAMICS
BETA	0.38	DYNAMICS
IMFLAG	1	GENERAL
IGS	2	GENERAL
NSOLVR	12	SOLUTION

In this way, the boundary conditions for the heads could be set directly from the material card.

In the quasi-static compression model can be seen in Figure 3.10, all translational and rotational displacements of the bottom head were fixed. As a result, translational displacement in the Z-axis is free for the top head.

Thanks to implicit analysis, the velocity of the top head was defined as 0.025 mm/sec, and the termination time was set as 640 seconds.

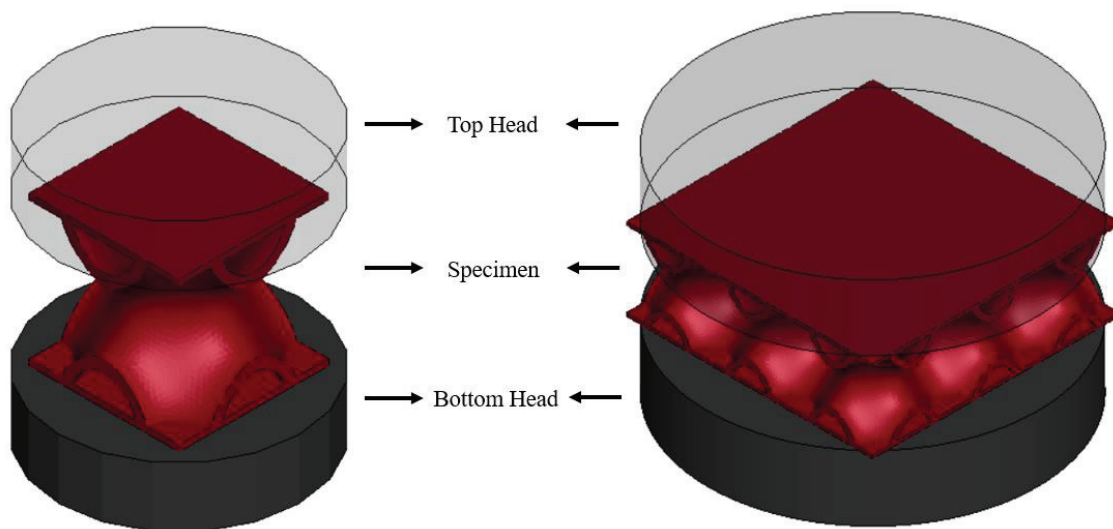


Figure 3.10. Numerical model of the unit and nine cells structures static compression

3.4.2. Direct Impact

Since this thesis aims to design an alternative shock-absorbing structure, the accuracy of the numerical modeling of impact loading tests is crucial. In the numerical modeling of the direct impact test, in which the energy absorption ability of the single-cell structure is demonstrated at dynamic strain rates, the MAT_181 material model, which contains the strain rate sensitivity effect, was used for the sample. In addition, the MAT_ELASTIC (MAT_001) material model was used for AL 7075, the material of the bars. The incident and quartz crystal surfaces are shown in the figure were combined without the need to define a contact with the duplicate node. The translational and rotational displacements in the X and Y axis were constrained with the BOUNDARY_SPC_SET keyword, provided that translational and rotational

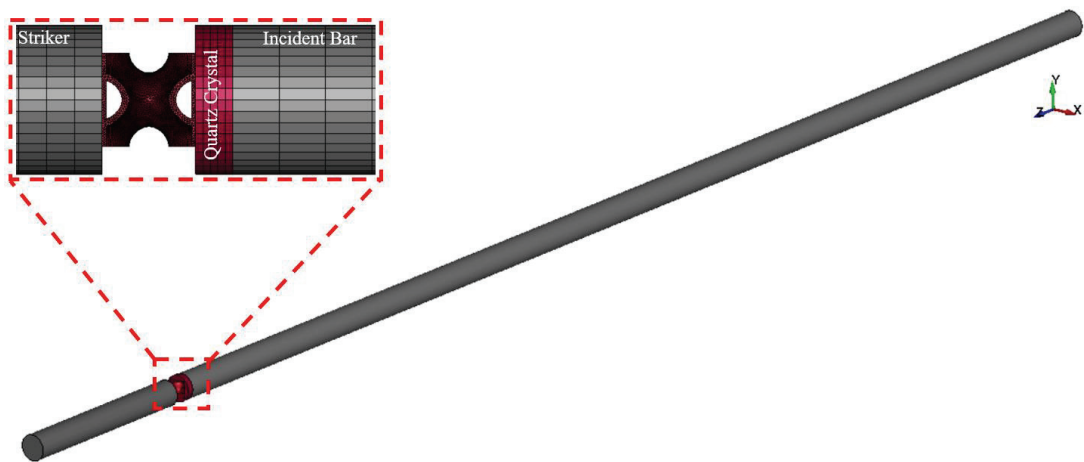


Figure 3.11. Numerical model of the direct impact test for unit cell

displacements are free on the Z-axis. By using the INITIAL_VELOCITY keyword, the desired velocity values in the - Z direction were assigned to the nodes that created the striker.

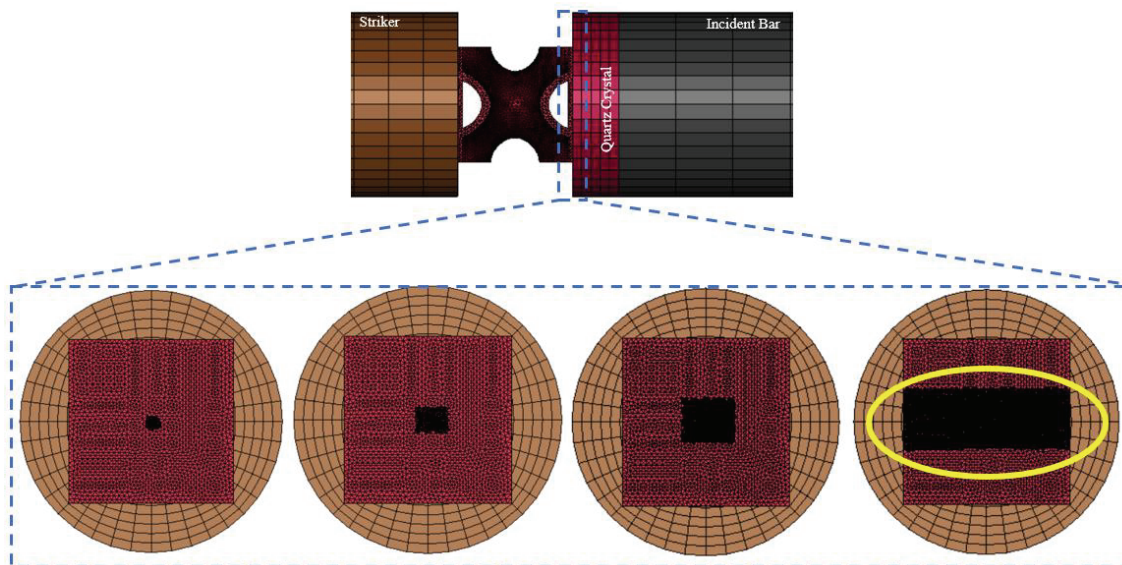


Figure 3.12. Double sided tape area trials

A double-sided tape, mentioned in the previous chapter, between the quartz crystal and the sample surface is used to keep the sample fixed on the bar surface. Therefore, the keyword CONTACT_TIED_SURFACE_TO_SURFACE_OFFSET is defined on the bottom surface of the sample shown in the Figure 3.12 and on the quartz crystal surface. It is assumed that the confinement effect on the bottom surface of the sample will change depending on the size of the double-sided tape used, and analyses with the double-sided

tape of different sizes are also tried and examined. As a result of the analysis, one node on the striker and quartz crystal is defined with the keyword DATABASE_HISTORY_NODE to get the displacement output quickly.

3.4.3. Drop Weight

The drop weight tester was modeled with an explicit solver. In this numerical model, initial conditions were necessary besides the material model, just like in the direct impact model. The striking upper head and fixed lower base are modeled RIGID. MAT_181 material model was used for core TPMS structures 9 cells. The velocity value is given to the moving head with the INITIAL_VELOCITY keyword. ELEMENT_MASS_PART keyword is used to add additional mass to the movable upper head. Apart from these, the contact formulations used are the same as the direct impact numerical model. Numerical models of four-cell and nine-cell TPMS core structures are shown in the FIGURE.

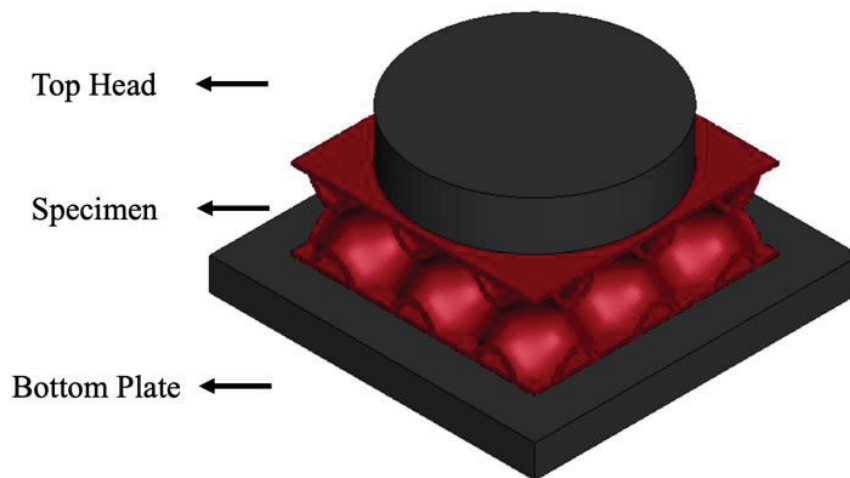


Figure 3.13. Numerical model of the 9 cells structures drop test

From numerical models, energy and SAE value was obtained. The area under the load-displacement curve can be used to calculate the specific energy absorption (SAE), which is a commonly used parameter to indicate the energy absorption capability.

$$EA = \int_0^{\varepsilon_D} \sigma(\varepsilon) d\varepsilon \quad (3.9)$$

where σ is stress and ϵ is strain. The specific energy absorption (SAE), which measures energy absorption per unit mass, is used to assess the effectiveness of energy absorption. A definition of the SAE is:

$$SAE = \frac{EA}{m} \quad (3.10)$$

where m is the mass of the lattice material, EA -is the absorbed deformation energy per unit volume. By integrating $\sigma(\epsilon)$ at displacements, the energy absorption of the lattice structure under different displacement can be obtained

The Crush Efficiency (CE) of the structure decreases as a result of dynamic tests due to the change in the deformation mechanism and the hyperelastic nature of the structure. The specified CE value is calculated as follows;

$$CE = \frac{P_{max}}{P_{mean}} \times 100 \quad (3.11)$$

3.4.4. Blast

An explicit solver is used in blast numerical modeling. This modeling aims to investigate whether the fractures in the tibia bone of the soldiers due to the acceleration caused by the explosive loads in NATO STANAG 4569 standards can be prevented with the designed TPMS core structure. In previous studies, it aimed to absorb energy against the explosion loads coming from the vehicle's underside by covering the structures designed on the bottom base plate (Zhu et al. 2013; Schaedler et al. 2014; Zhu et al. 2014; Quenneville, Fournier, and Shewchenko 2017).

There is more than one method to perform a blast simulation. The most known methods are ALE, CONWEP, and PDM-DEM models. In this study, the CONWEP function was used to get the fastest result, and it was activated with the `LOAD_BLAST_ENHANCED` keyword in Ls-Dyna. The HYBRID III(50% Centile) dummy is positioned in the middle of the 200x200x1 cm plate in the model. The explosive was placed 50 cm below the floor plate as in the Figure 3.14. Steel was used as the plate

material, and it was assumed that no damage occurred. The mass was defined as 10 tons with the ELEMENT_MASS_PART keyword.

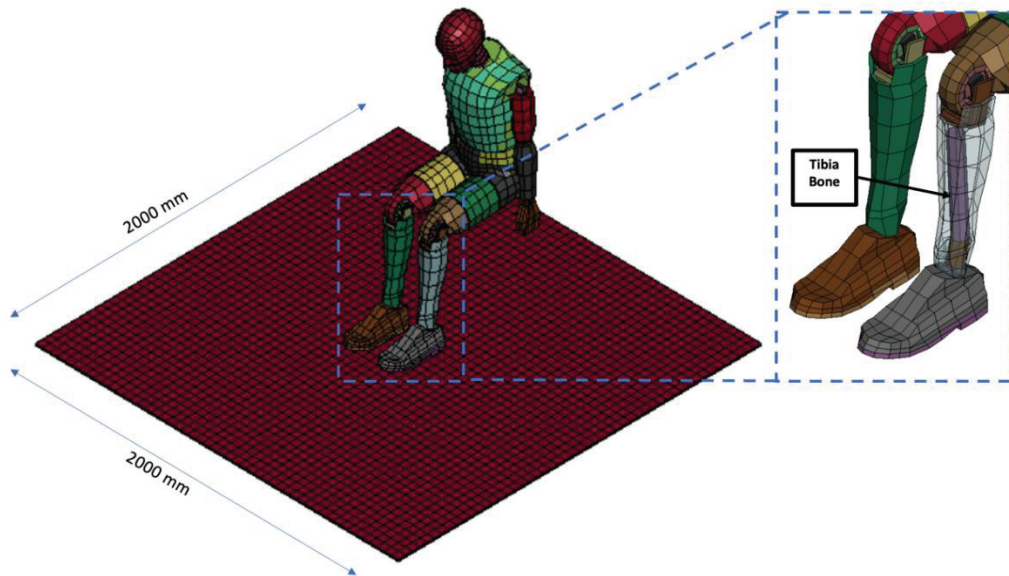


Figure 3.14. Numerical model result of the blast and joint points of the tibia bone

The contact keyword TIED_SURFACE_TO_SURFACE_OFFSET was used between the core structure and the plate, and the AUTO_SURFACE_TO_SURFACE contact keyword was used between the foot and the structure. For stabilization of the assay, the timestep was set to 0.33. Analyzes were performed under the same conditions as the Figure 3.15 for only the bottom plate and TPMS core structure.

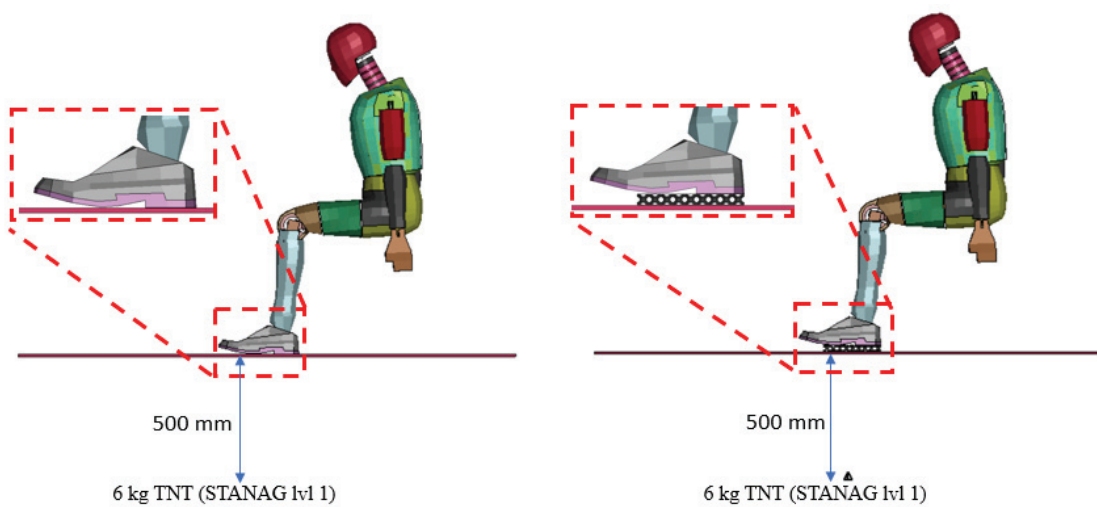


Figure 3.15. Numerical model prepared with only bottom plate and bottom plate with TPU TPMS structure

CHAPTER 4

EXPERIMENTAL AND NUMERICAL RESULTS

According to ASTM 638D-14 Standard, the test process was carried out after the samples were kept at room condition for at least 4 hours. Tensile Tests were carried out according to ASTM 638D standard. Individual samples were used for compressing.

The printed material exhibits a typical elastomeric behavior in the stress vs. strain curve, with a linear elastic area and then a non-linear behavior. Following the first stress-strain response, the strain begins to soften at around 25% strain, then begins to harden at about 300% strain. No failure was observed as a result of static characterization and structure tests. However, in the compression test performed at 4187 1/s strain rate, it was observed that there was separation between the layers of the specimen. However, in the dynamic tests performed with single and multiple cells, no separation was observed in the microscope examinations.

ASTM 638D Type IV samples were used in quasi-static tensile specimens. First, 1/s tensile test was performed and the test results are shown in the Figure 4.2. The test velocity was set as 0.025 mm/s depending on the strain rate. The tests were terminated at 1.6 strain, which is the maximum measuring range of the extensometer, and it was observed that the above part of the graph displayed similar behavior when compared with the literature (Płatek et al. 2020).

In this study, since no failure was observed in the static and dynamic analyses of both single and multi-cell structures, no failure criteria were considered in the material model. Since the engineering stress-strain curve will be entered as input in the material model found in Ls - Dyna, no conversion process has been applied. Only the curves entered as input in Ls - Dyna was smoothed beforehand and then defined.

Due to the nature of TPU, high strain rate sensitivity was observed as expected. Then, the previously shown cylindrical specimens were used for quasi-static compression tests. Tests were carried out at 10^{-3} , 10^{-2} and 10^{-1} 1/s strain rates, and head velocity of 0.002 mm/s, 0.02 mm/s, and 0.2 mm/s were set, respectively.

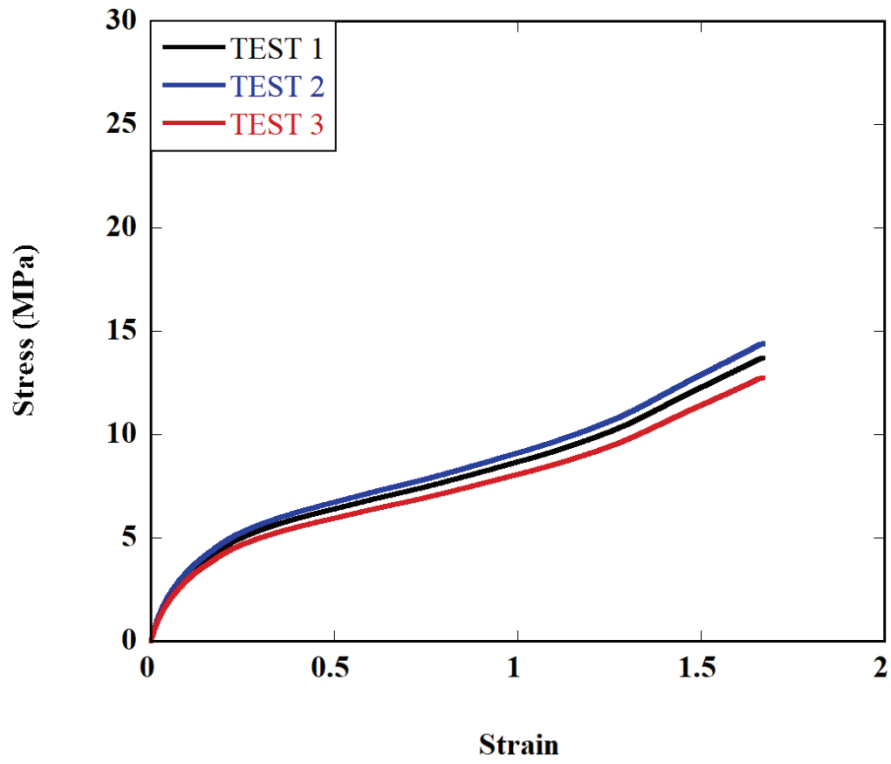


Figure 4.1. $10^{-3}/s$ Quasi-static tensile stress-strain curves

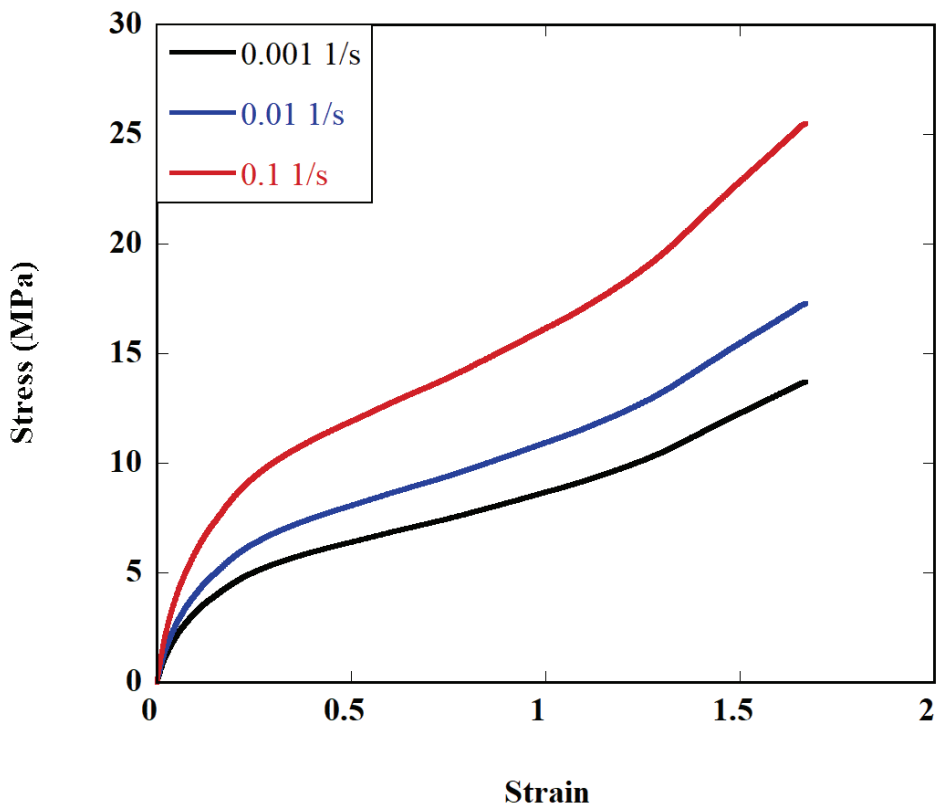


Figure 4.2. Comparison of quasi-static tensile stress-strain curve

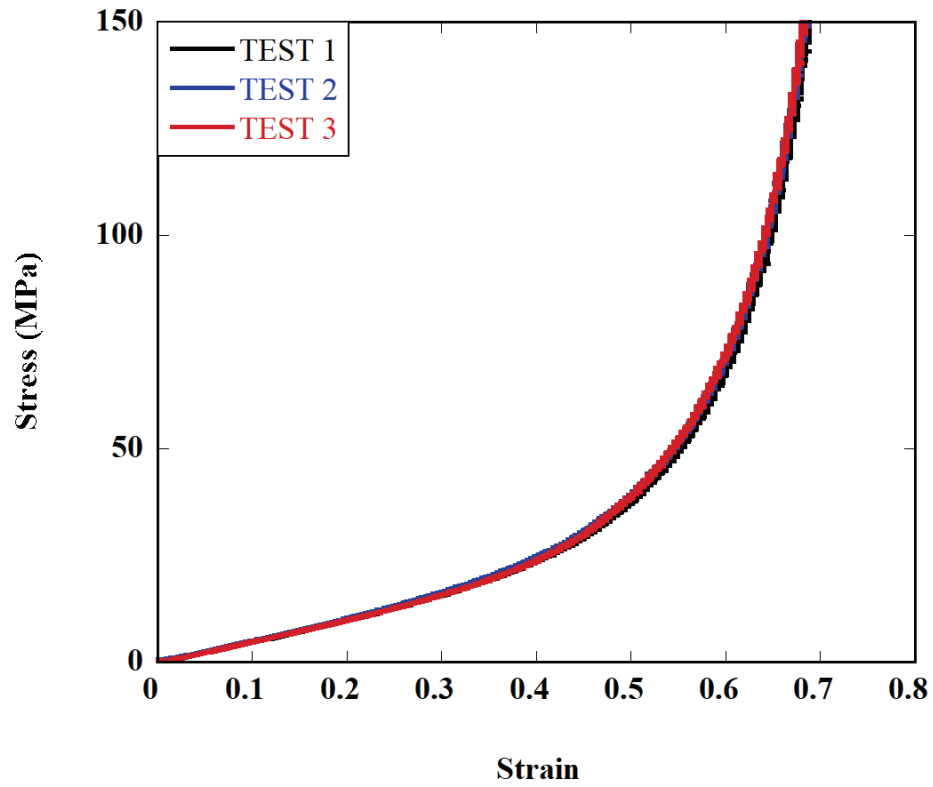


Figure 4.3. $10^{-3}/s$ Quasi-static compression stress-strain curves

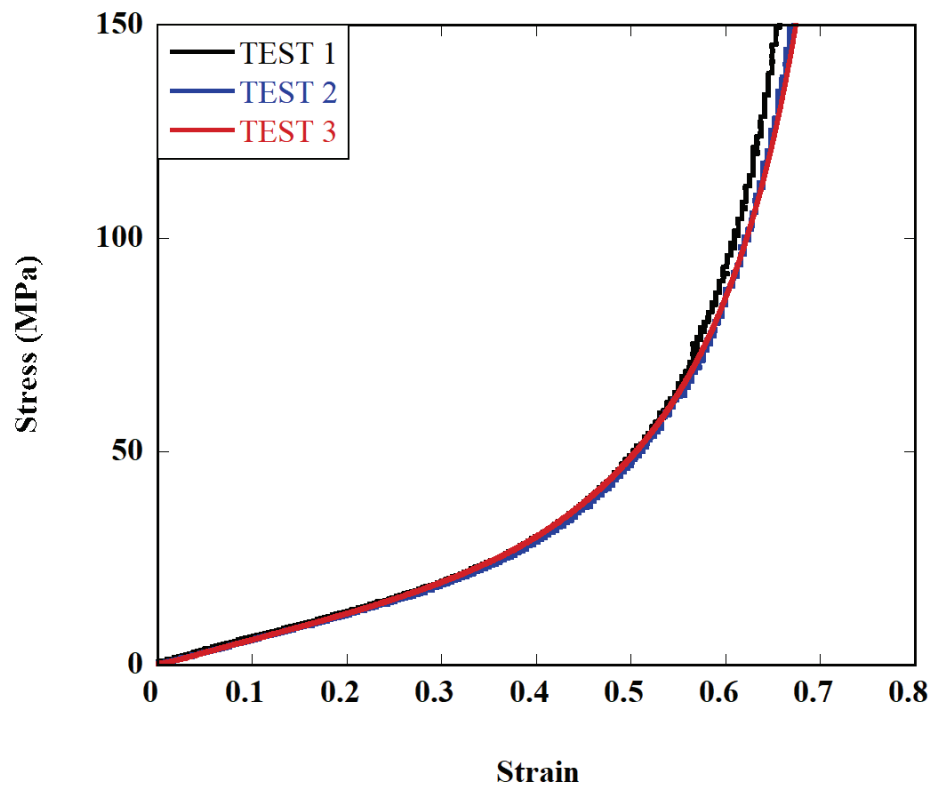


Figure 4.4. $10^{-2}/s$ Quasi-static compression stress-strain curves

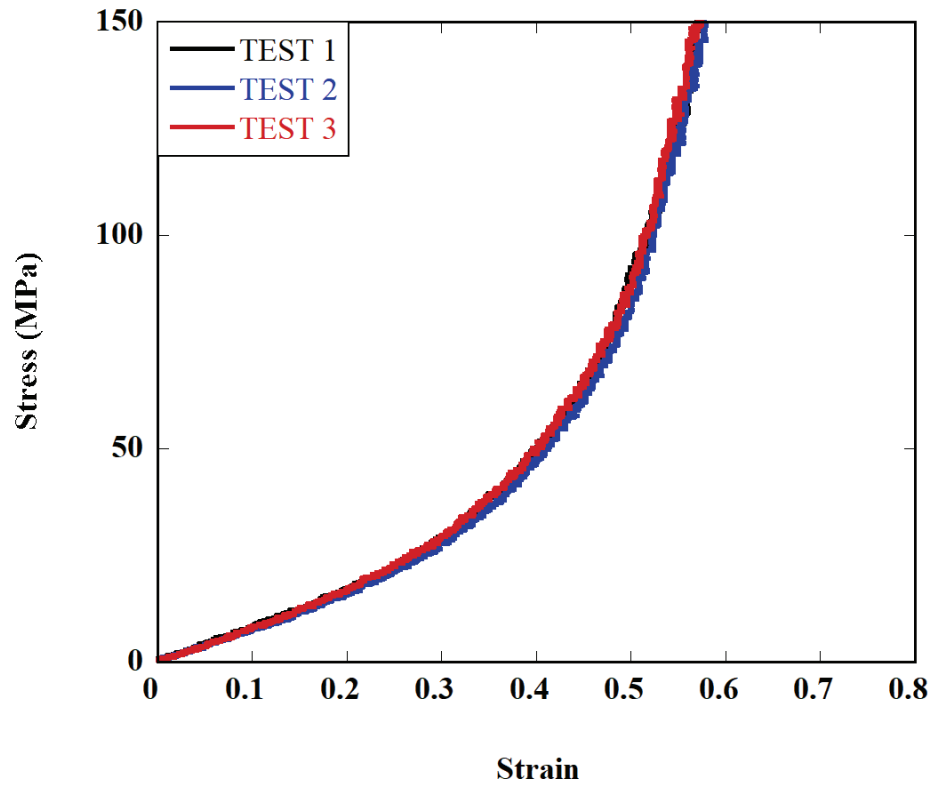


Figure 4.5. $10^{-1}/s$ Quasi-static compression stress-strain curves

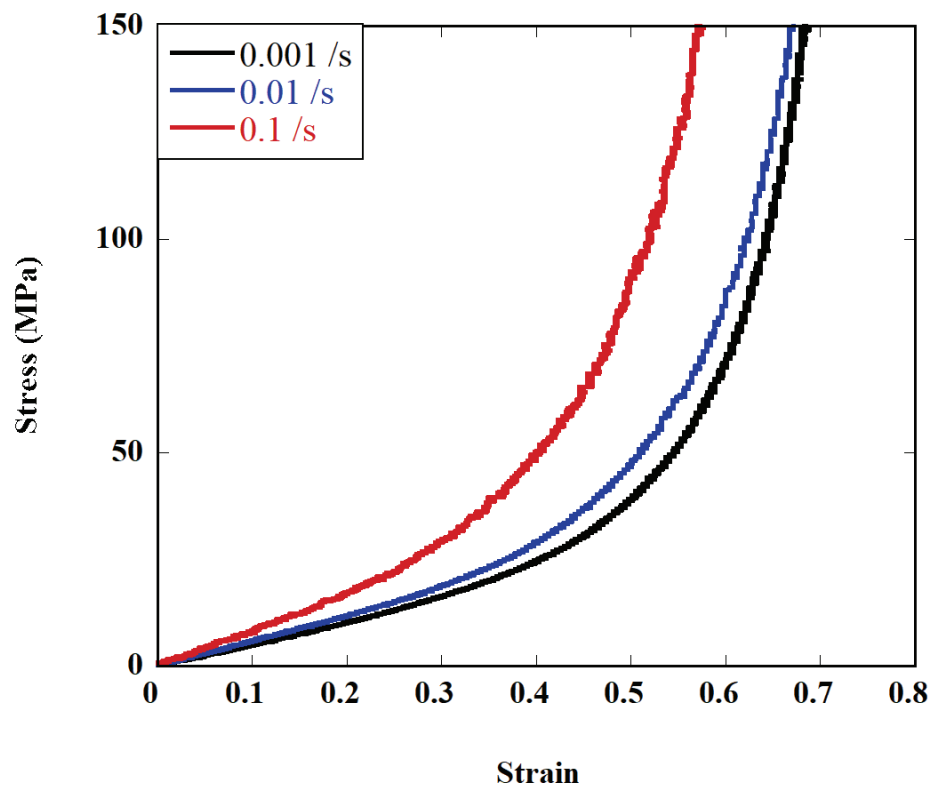


Figure 4.6. Quasi-static compression stress-strain curves comparison

As a result of these tests, both tension and compression curves were combined, and the static region was completed. The comparison of the quasi-static compression curves for the 10^{-3} 1/s to 10^{-1} 1/s strain rates is shown in Figure 4.6. The material's behavior under compression stresses was strain rate dependent, just like under tension stresses.

The accurate stress-strain correlations show that in Figure 4.7, the TPU polymer's reaction was significantly influenced by strain rates across five decades of strain rates. As the strain-rate increases, the stress levels continuously increase. At strain rates below 4157 1/s, failure was not apparent. The literature shows that the observed failure rate for TPU produced with conventional methods was 5000 1/s (Jamil 2018).

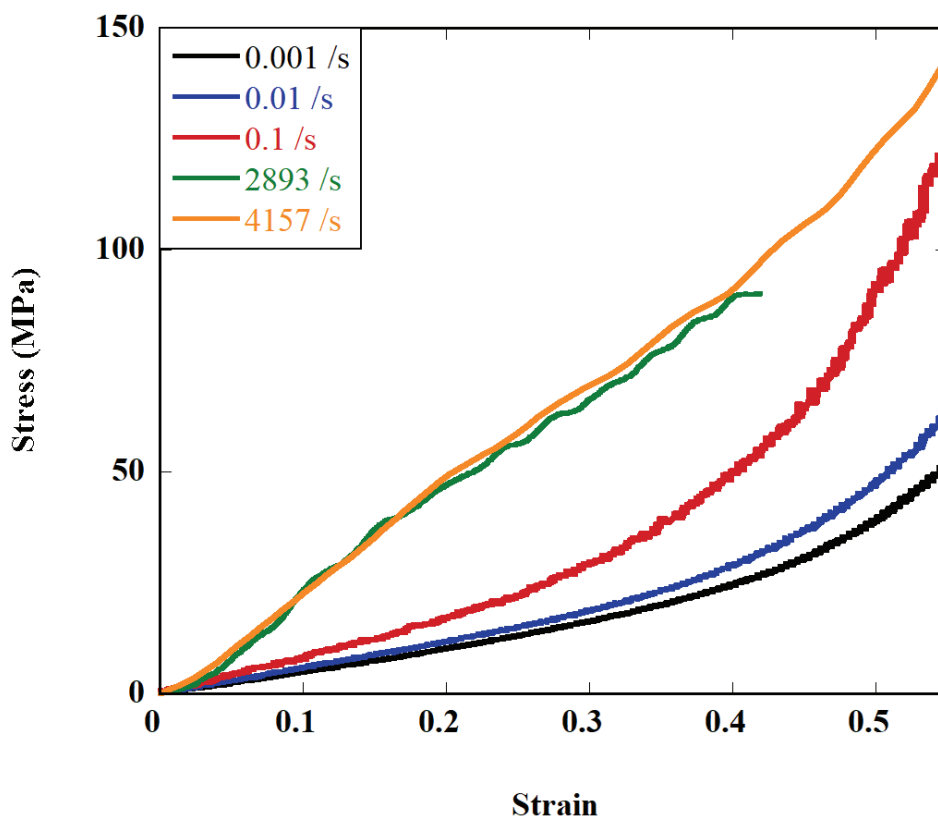


Figure 4.7. Comparison of quasi-static and dynamic compression stress-strain curves of 3D printed compression specimens

SHPB tests were performed to observe the behavior of TPU at dynamic strain rates. With the dynamic compression tests performed at 2893 1/s and 4157 1/s strain rates, it was observed that the material has high strain rate sensitivity. As a result of the tests, it was found that the densification strain was between 0.6-0.7 in static tests, but this value was between 0.5-0.6 at high strain rates and was shown in Figure 4.7.

Under the higher strain-rate loadings, the shape tendency of the stress-strain curves mostly maintains the same, with an apparent strain-hardening phase after the first loading. Furthermore, it is clear that as the strain rate grows, the TPU's strain energy release also rises, which may be a beneficial strain rate-dependent behavior under shock-loading circumstances. Such strain rates make it possible to precisely characterize how the stress-strain behavior changes with increasing strain-rate loading.

The engineering stress-strain curves obtained after the static and dynamic compression tests were collected in a table and defined in the numerical model, as mentioned in the previous chapter, in the material card.

As seen in the Figure 4.8, the stress-strain characteristic of TPU is not symmetrical for compression and tension zones. Although the linear part in the compression region is negligible, this region can be seen for the tension side.

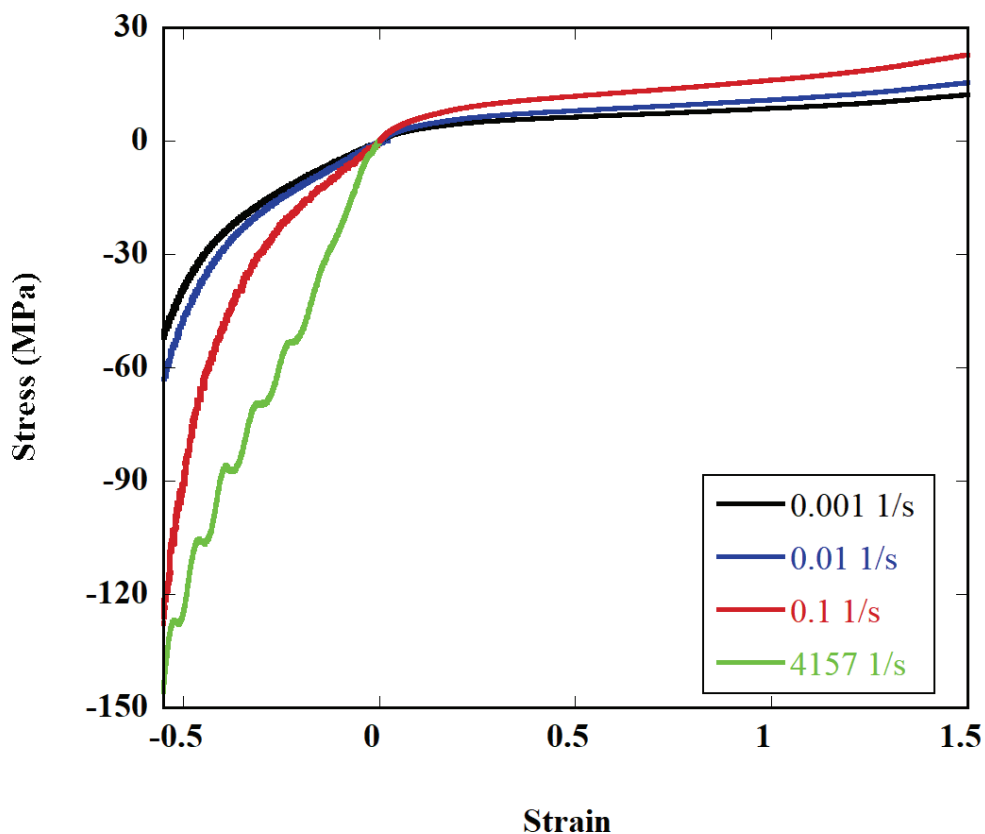


Figure 4.8. Input curve of material model in Ls - Dyna

As a result of the tests, it was observed that the stress at the densification point decreased as the strain rate increased. The material's behavior can be transferred to the model numerically from the strain rate sensitivity of the selected material model.

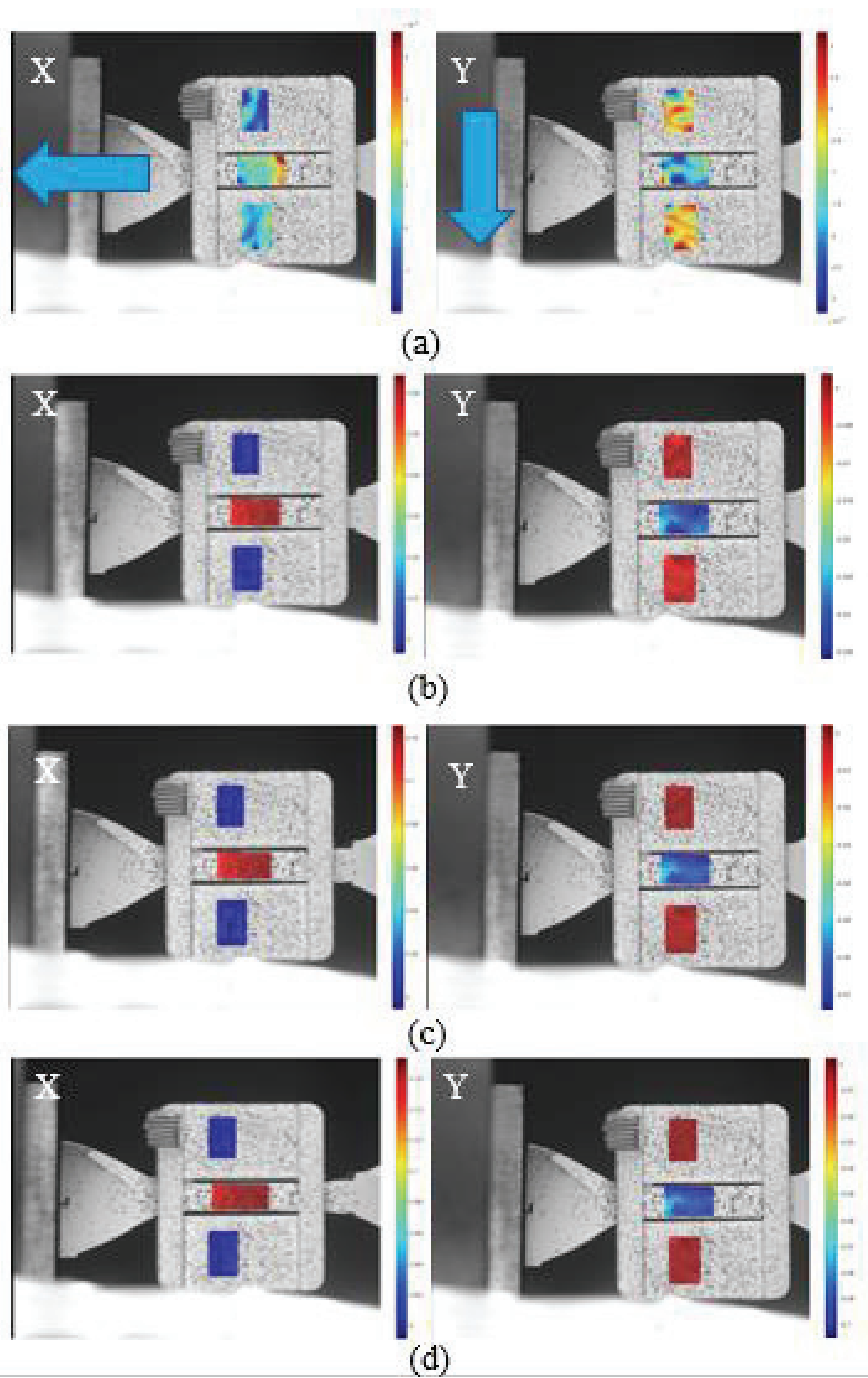


Figure 4.9. Displacement of specimen at (a) 0 sec (b) 12.3 sec (c) 24.6 sec (d) 36.9 sec by using DIC

According to Juang et al. , the average poisson ratio was found 0.42. In Figure 4.9, the fit curve used for poisson and the DIC output at the specified displacement moments are seen for the X and Y axes (Juang 2021). For the accuracy of the method, the results of the type I sample specified in the ASTM 638D standard were compared in the article from which the method was taken, and the poisson's ratio was found to be 0.47 for the type I sample. However, since it is known that the thickness of the TPU TPMS structure varies between 1.2 mm and 1.8 mm, type IV specimen was used to consider the Poisson's ratio.

4.1. Validation of Numerical Model and Test Result

In order to verify the compilation of the element with the state parameter model, single-element analyses of the conventional compression test were performed and compared with the single-element results. Thanks to the MAT_181 material model, the analysis correlates with the test and ends without error, even up to the densification zone.

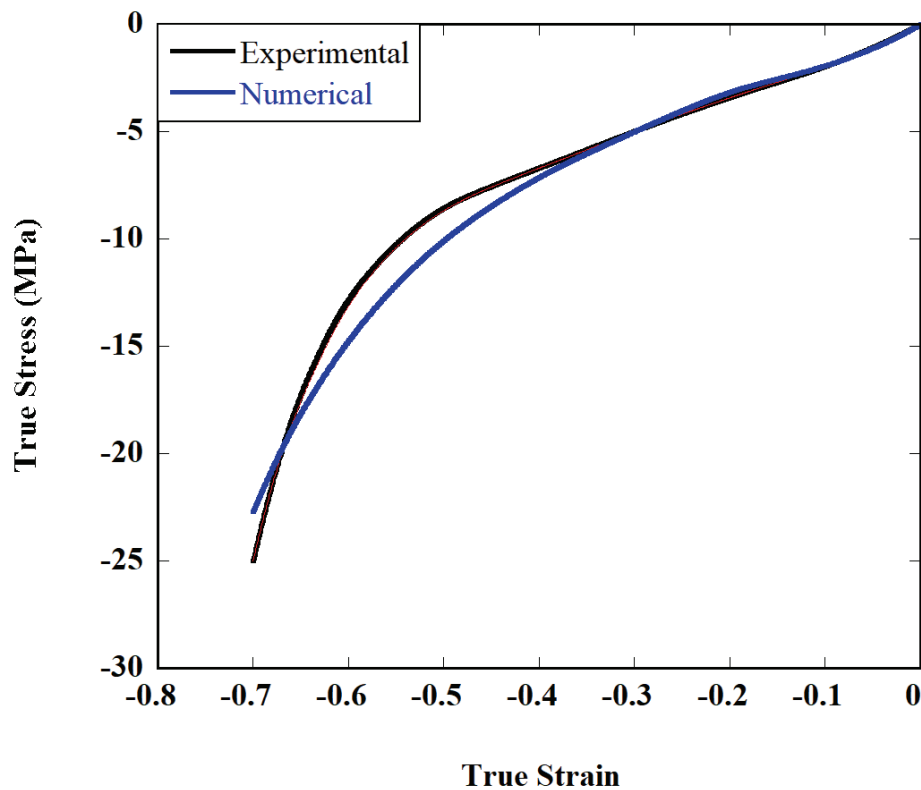
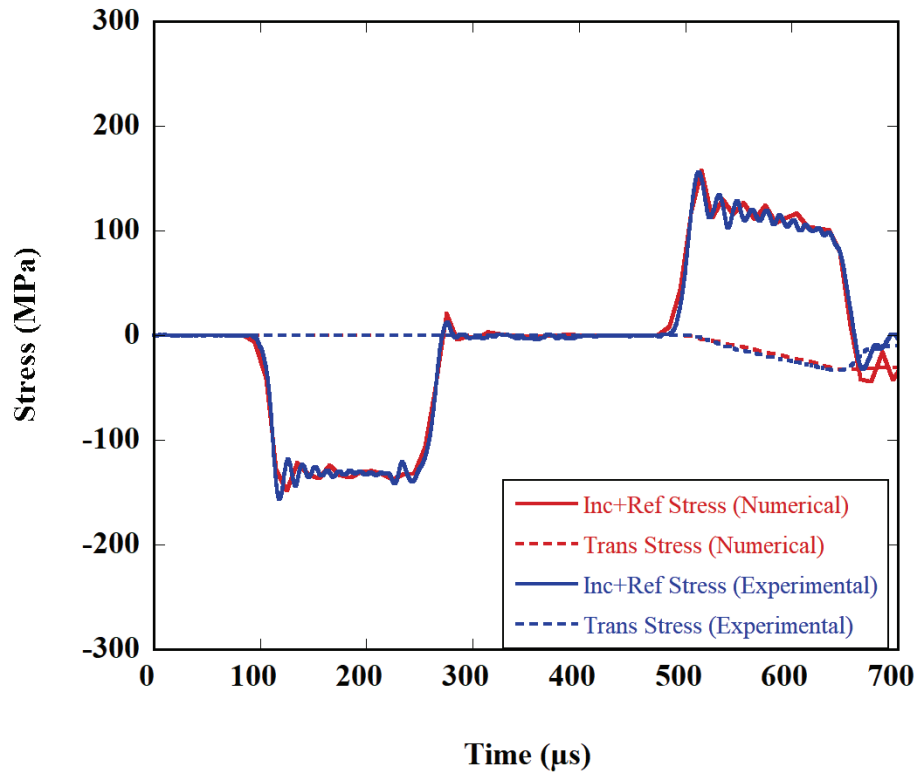
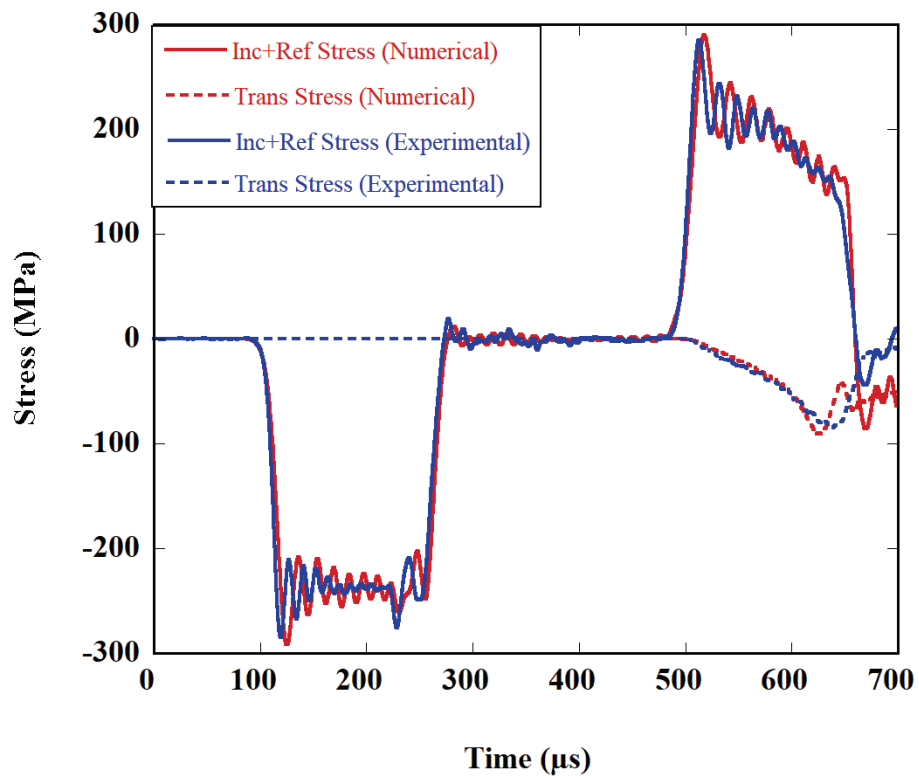


Figure 4.10. Comparison of the numerical model by using MAT_181 and the static compression test



(a)



(b)

Figure 4.11. Stress - strain curves of TPU specimen at (a) 2893/s (b) 4157/s strain rate

For dynamic tests performed at strain rates of 2893 1/s and 4157 1/s, the Split Hopkinson Pressure Bar (SHPB) test setup model explained in chapter 3 was used. It is seen in the Figure 4.11 that the material model is correlated with the tests. Since the unloading curves of the TPU are not defined in the model, the difference between the test and numerical after maximum stress increased.

4.2. Unit Cell Structure Static and Dynamic Compression Results

In this thesis, schwarz primitive unit cell was selected. This geometry was the first investigated TPMS type of structure. Also, schwarz primitive is known for relatively high compressive strength and SAE capabilities (Restrepo et al. 2017). However, since it is intended to make one cell throughout the thickness of the cells, the region between the two cells was chosen, and the force-displacement and SAE graphs with the regular Schwarz primitive and the selected intermediate region rotated 90 degrees are shown in the Figure 4.12. Simplified Rubber material model was chosen in the numerical model for all structures. Graphs were drawn with the contact forces taken from the direct impact test numerical model.

The chosen single-cell geometry was compression tested at a quasi-static strain rate. The structures having 25 mm height and varying thickness of 1.2 to 1.8 mm. The crosshead velocity was selected at 0.025 mm/min, corresponding to the desired strain rate level (0.001/s). The quasi-static force-displacement curve of the TPMS cell is shown in Figure 4.13.

From the force vs. displacement curve, SAE and peak force were calculated. Thus this test allowed relatively compared alternative geometry along each other. The secondary outcome of the test, for the dynamic compression test, was needed to calculate the impactor initial velocity for the subsequent drop test. Also from this test, peak force and densification point was noted from experimental curves.

As a result of the test, peak force, and densification points were noted from the force-displacement curve. In addition, it has been observed that the structure exhibits type I crushing behavior under static loads, which is described in the literature section (Lu and Yu 2003).

The comparison of the force-displacement curves of the experimental and the numerical model with the corresponding shown in Figure 4.14. In this experiment, some

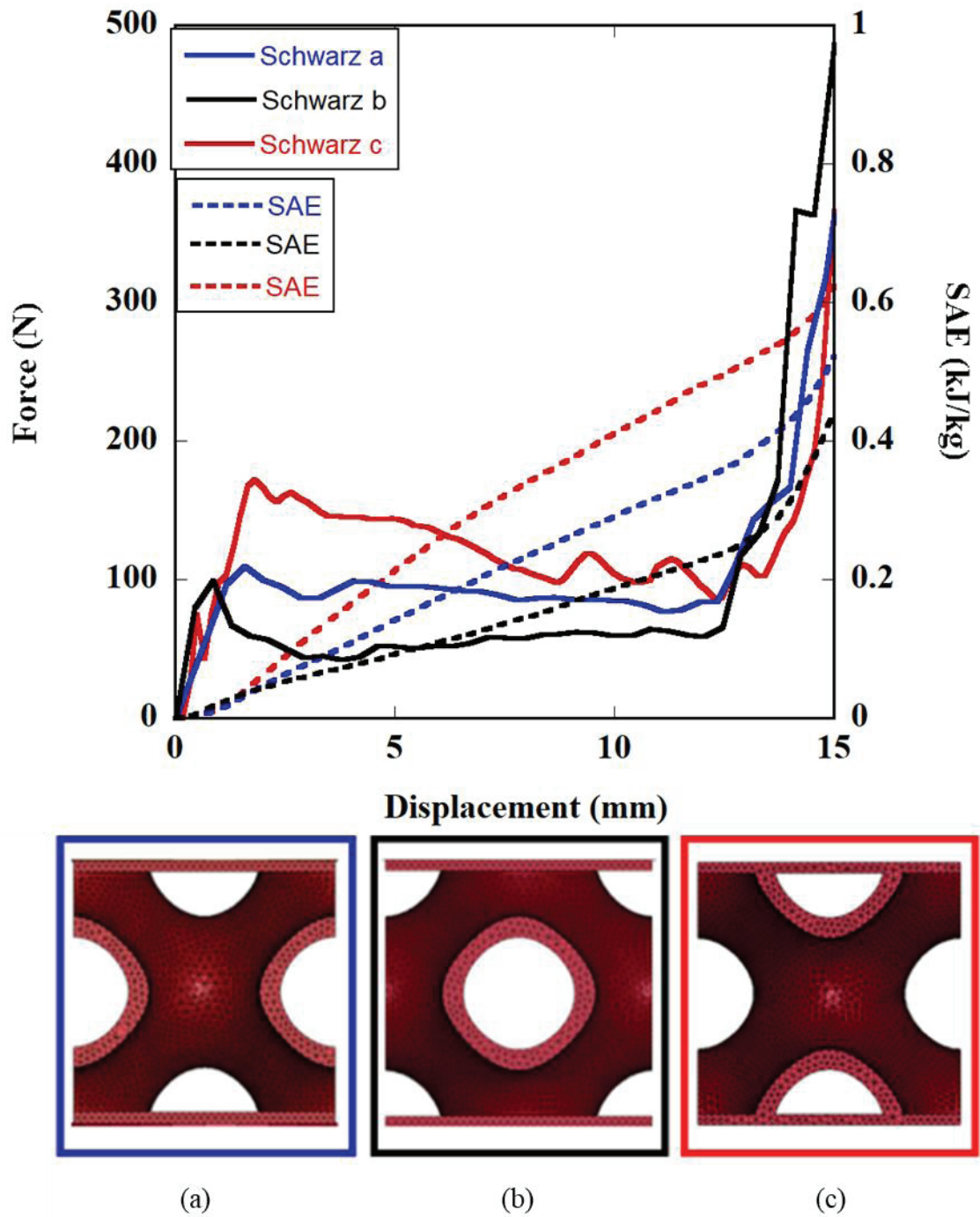


Figure 4.12. Comparison of the force displacement and specific absorb energy of (a) the schwarz primitive (b) 90-degree rotation of the investigated cell, (c) investigated cell

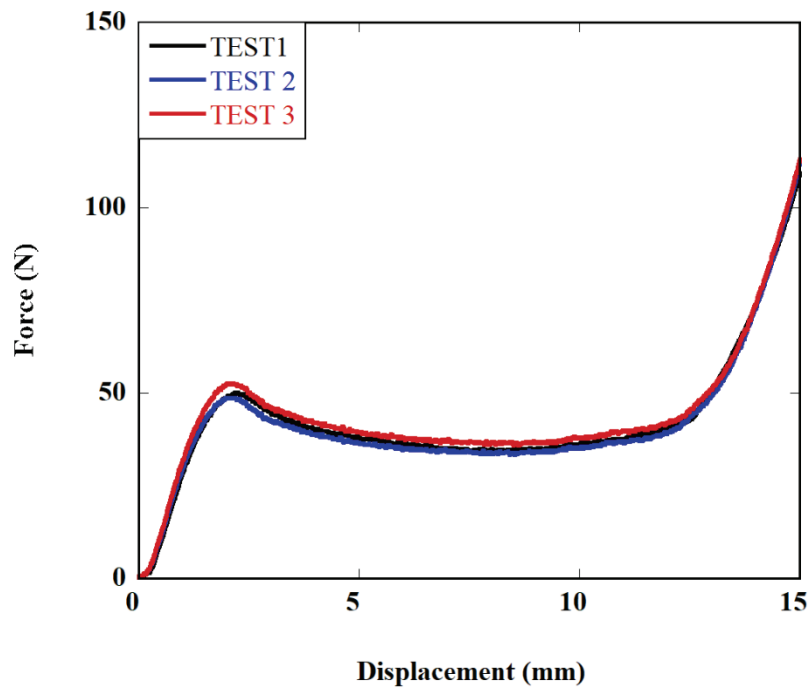


Figure 4.13. Experimental force-displacement curves of unit cell at $10^{-3}/s$

parameters varied to find numerical responses. For this reason, the bulk modulus of material was selected to compare 5 MPa and 50 MPa. 50 MPa was chosen for close agreement with the experimental results. Different material models were also tried. Mooney Rivlin and Simplified Rubber material model were used in static compression of the unit cell structure.

The compressive behavior of the structure well predicted with the experimental and numerical models. Peak force comparison seen in Figure 4.15, it was observed that the Simplified Rubber material model and the model in which the bulk modulus value was determined as 50 MPa remained in the 10% difference compared to the peak force value determined in the tests. Although the peak displacement observed in the test was 2.1 mm, 2.4 mm was obtained in the model. However, the densification point was determined to be approximately 12.3 mm in both the numerical model and the tests.

The Simplified Rubber material model takes into account the strain rate effect with stress strain curves at discrete strain rates entered into it. However, the Mooney Rivlin material model does not take into account the rate sensitivity of the base material.

In Figure 4.17 The quasi-static experimental and numerical force-displacement curves of the unit cell are given along with specimens and also diagonal section the deformation deformation modes are in good agreement.

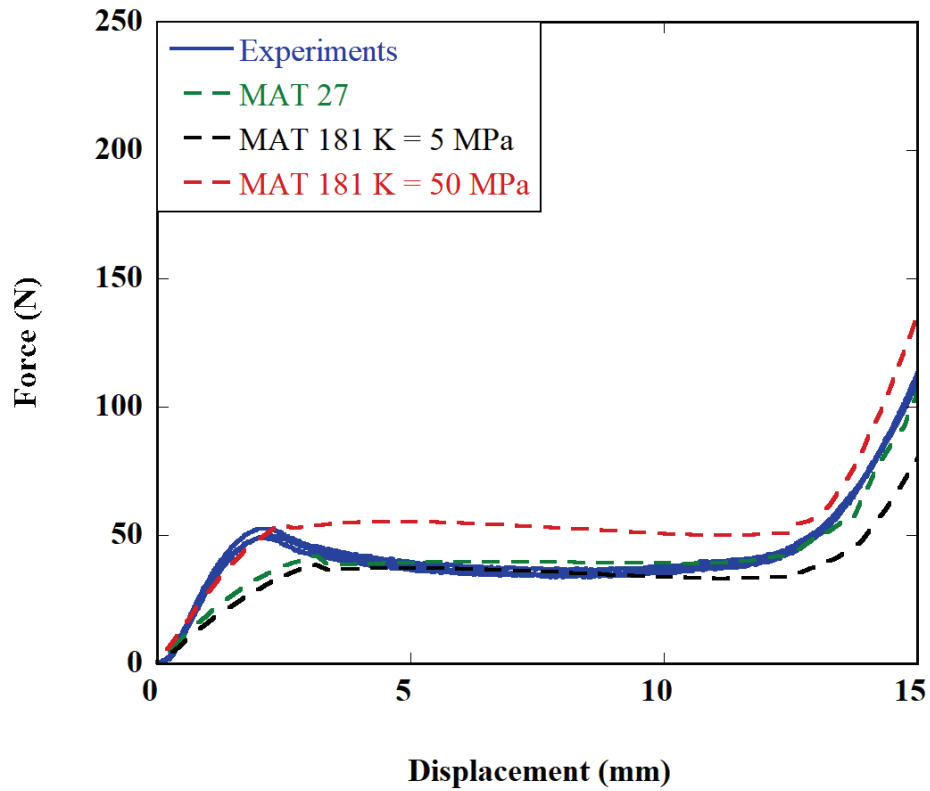


Figure 4.14. The experimental and numerical force-displacement curves for different material model

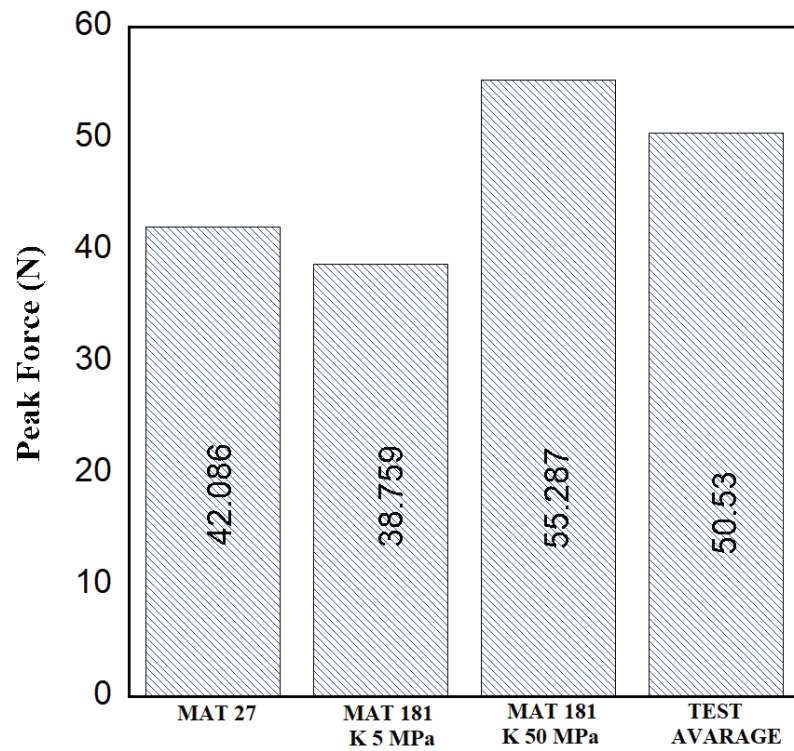


Figure 4.15. The effect of the material model type and parameter on peak force

In the composite (half experiment, half numerical) picture given in Figure 4.17. There is a close agreement between the experiment and the numerical model for the unit cells. At about 2.2 mm. displacement in experimental and numerical studies, nearly 50 N peak force was observed. Then the center section of the unit cell was significantly warped and twisted after 2.1 mm. and the force values drop observed after the peak point.

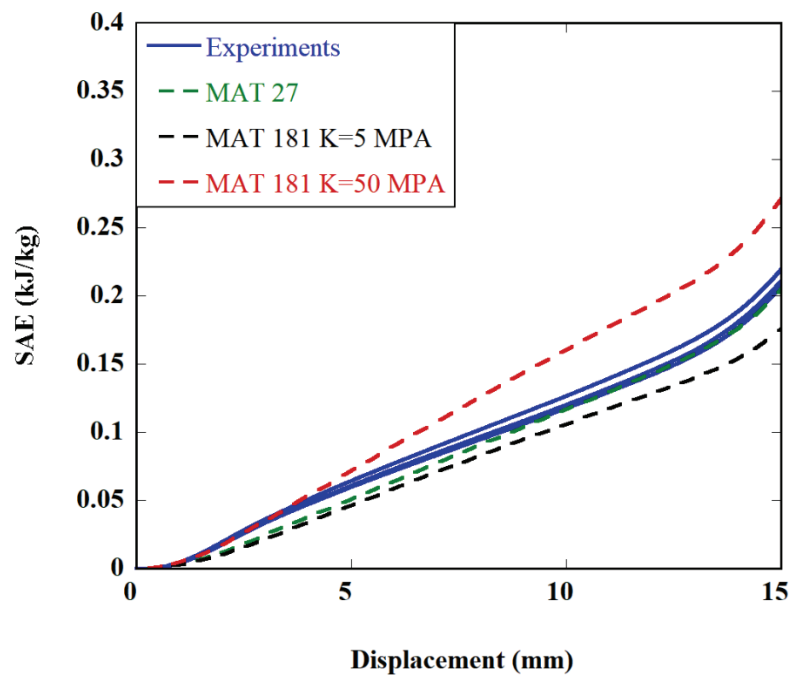


Figure 4.16. SAE vs. displacement curves of unit cell structure at $10^{-3}/s$ strain rate

As can be seen, the diagonal section is given in Figure 4.17. The bottom half of the unit cell was also locally bent. At around 11.4 mm. displacement, the top and bottom half lean toward each other, and the force curve suddenly increases. This results in a densification displacement of 12.95 mm. And asymmetric mode of deformation was noted after 4.1 mm. (Figure 4.17 (c),(d)).

Due to the high strain rate sensitive material, TPU, there is a significant force increase, 50N for quasistatic and 150N for dynamic, respectively. The most significant differences between static and dynamic deformation behavior were observed after 2.2 mm. displacement. An inverted dimpling was observed at the unit cell's central section in the dynamic deformation. Then as the deformation proceed, both the lower and bottom part of the unit cell lean each other. Finally, densification displacement was observed at 14.2 mm.

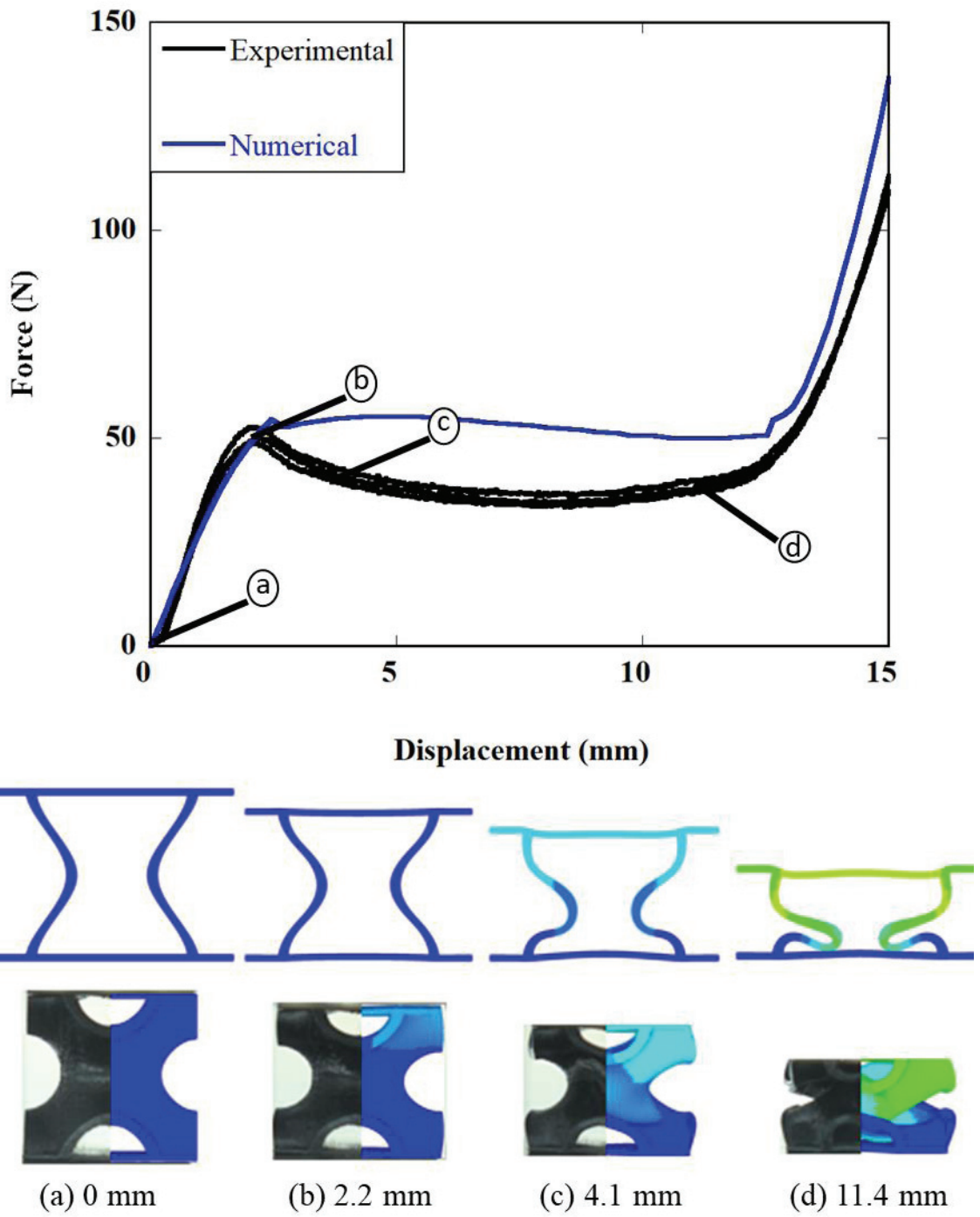


Figure 4.17. Static experimental and numerical force-displacement history of a unit cell at (a) 0 mm, (b) 2.2 mm, (c) 4.1 mm, (d) 11.4 mm..

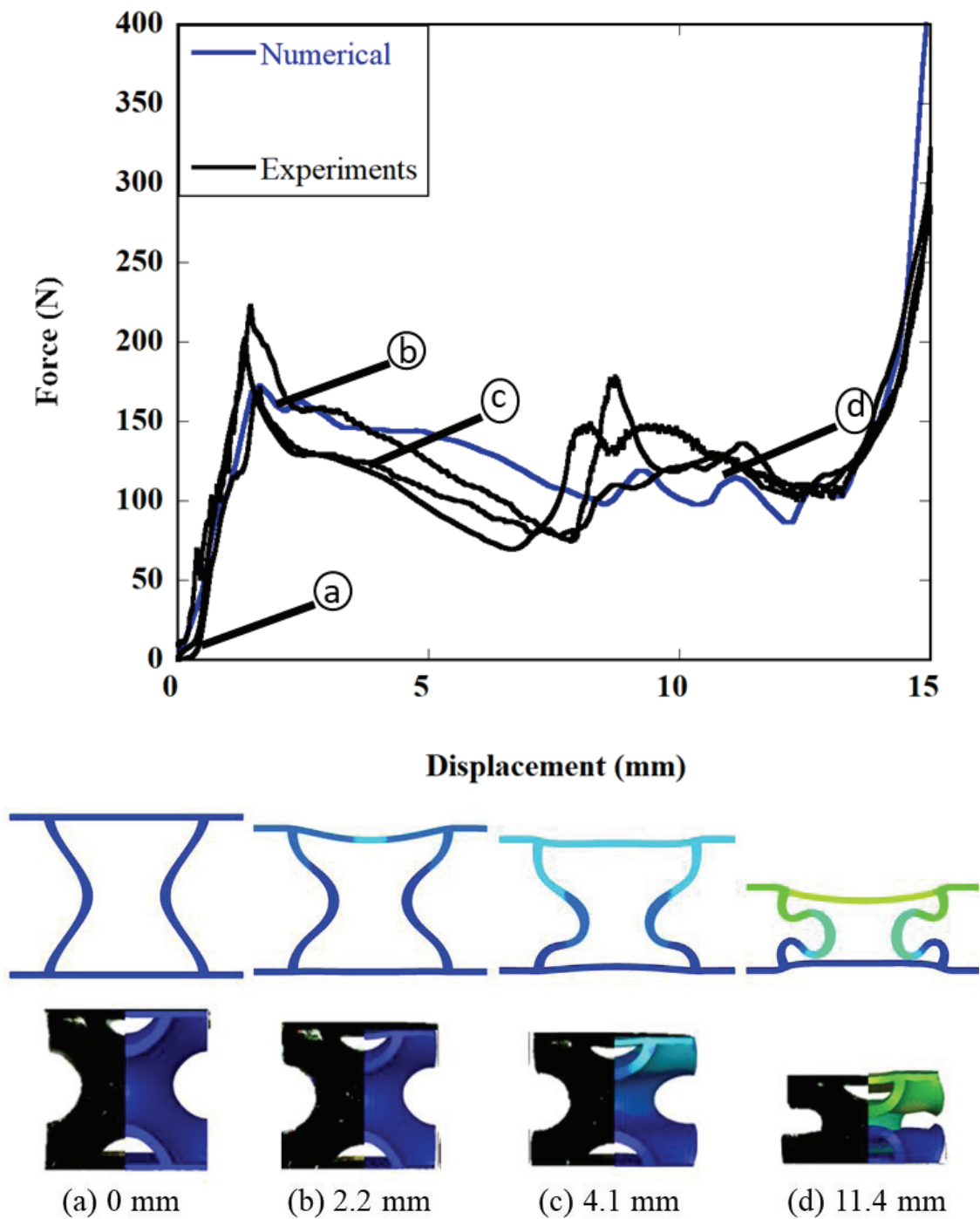


Figure 4.18. Dynamic experimental and numerical force-displacement history of a unit cell at (a) 0 mm, (b) 2.2 mm, (c) 4.1 mm, (d) 11.4 mm.

The SAE curve obtained from the force-displacement curves is shown in Figure 4.19. It has been noted that the numerical behavior in the zone of densification is consistent with the tests due to the Simplified Rubber material model used.

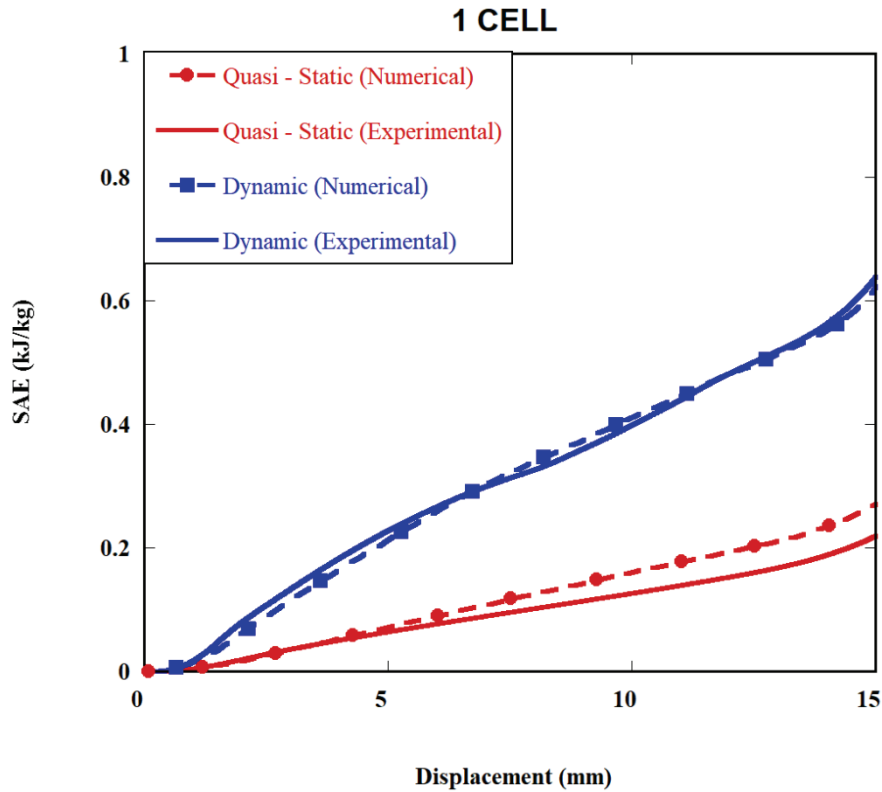


Figure 4.19 SAE vs. displacement curves comparison of unit cell

4.2.1. Strain Rate and Micro-inertia Effects for One Cell Structure

After showing the validity of the numerical model through experimental studies, the study proceeded to in this section to investigate various mechanisms, including higher impact rates. The deformation behavior of thin-walled structures defines the classification of energy-absorbing structures as Type I and Type II (Tam and Calladine 1991; Calladine and English 1984). Force-displacement curves with relatively flat peaks are classified as type I, and steep force-displacement curves are classified as type II. Type II structures are more sensitive to strain rate and micro-inertia than Type I structures. The efficiency of type 1 crushing behavior is higher than that of type II. Although the first peak force is higher in Type I, the slope on the plateau reduces the crushing efficiency.

The structure's deformation strain rate will substantially influence mechanical behavior where the inertial effect is pronounced. Dynamic loads accelerate structures and after deformation mechanisms by generating shear forces and/or bending moments. Therefore, they affect the energy absorption of the structure (Wierzbicki 2004).

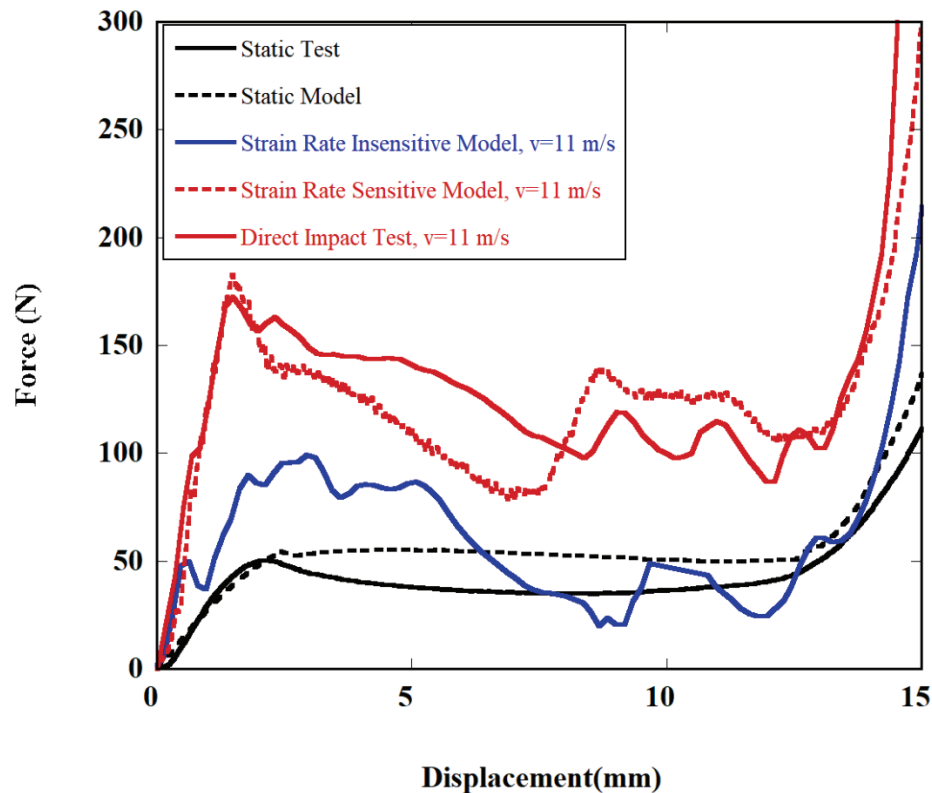


Figure 4.20. Comparison of force vs. displacement direct impact test and numerical model

As mentioned in the previous section, the peak force was a strong function of the strain rate, and deformation behavior was changed with the strain rate as well.

The increase in the peak force may be attributed to two different contributions, namely strain rate sensitivity of the base material and the inertia effect of the structure. In order to difference, the experimental and numerical model was re-run to incorporate strain rate and without effect, whereas the material model used stress-strain curve. This was done in the definition by switching on and off. While the difference between static and dynamic is that the contribution of both effects can give rate sensitivity of the base material, as seen in Figure 4.20. The peak force portion of the force-displacement curve was examined. As shown in Figure 4.21, the first part of the force-displacement curves for the quasi-static model, the direct impact test with 11 m/s penetrator initial velocity

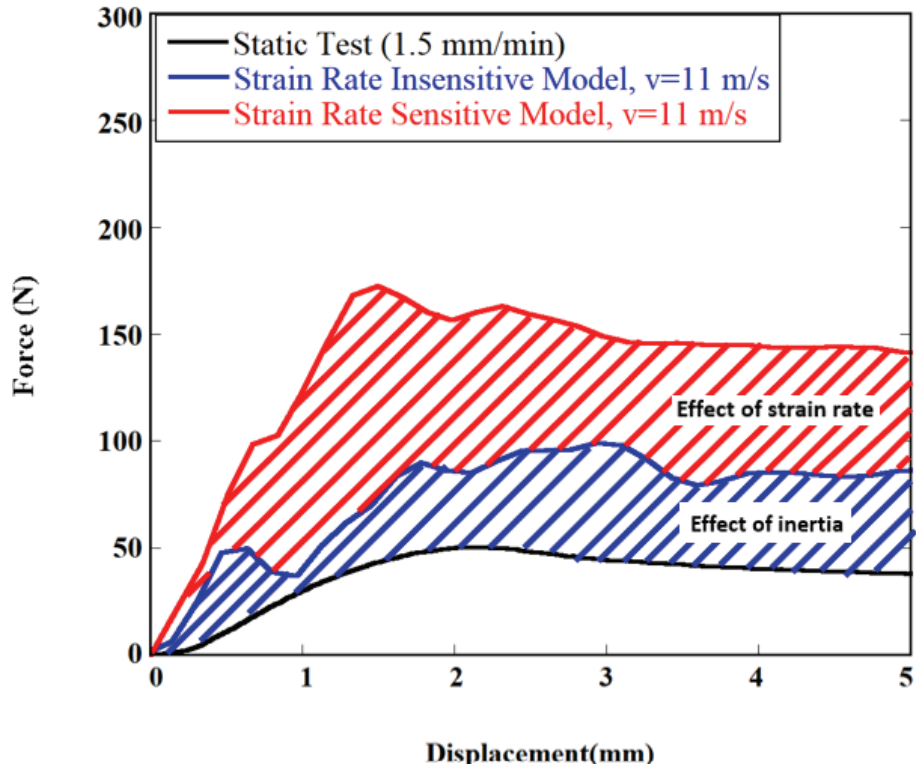


Figure 4.21. Investigation of inertia effect with rate sensitive experiment and rate insensitive numerical model

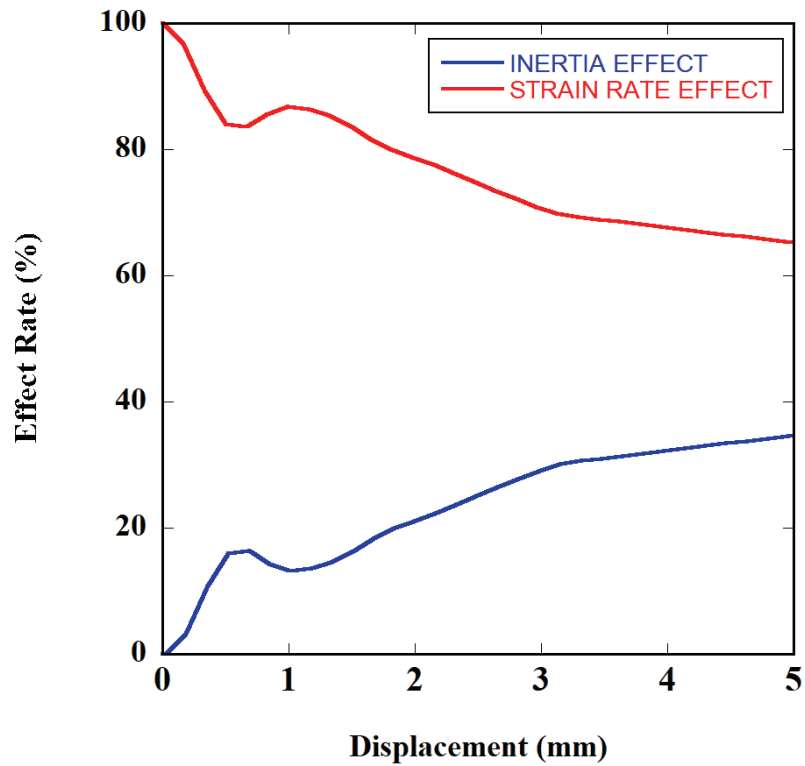


Figure 4.22. The percentage effect ratio-displacement curves of strain rate and inertia

and the strain rate-dependent model (0 to 5 mm). As can be seen in Figure 4.22, the force peak values were found to be more sensitive to strain rate than to inertia.

Experimental and numerical results are given in Figure 4.20. The maximum force value in direct impact experiments for one cell (183.35 N) is approximately 72 percent greater than quasi-static (50.53 N). The variation of the deformation mechanism is the cause, as will be detailed in more depth in the following section.

In the Table 4.1, the point chosen for the mean strength and SAE is chosen as the point where the structure enters the earliest densification and is specified based on that point in all other tests and models. As can be seen from the Table 4.1, the mean force values and SAE values increase as expected as the strain rate increases.

4.2.2. Nine Cell Structures Static and Dynamic Compression Results

For nine cells, tests were carried out at static and dynamic strain rates then experimental verified numerical models was used to determine deformation characteristic. However, since the bar diameter of the direct impact test setup was 40 mm., the dynamic tests were performed on the drop-weight test setup. Sandwich structure that consist of TPU face sheets having 1 mm thickness and 9 TPMS structures cores.

The force vs. displacement curve obtained from the static tests is as in Figure 4.23. In the multi-cell static analysis, the cross head covers all cells. With this test, it was essential both for the interaction between cells and for determining the energy level for the drop-weight test to be performed afterward. As a result of the test, the peak force was found to be 691.67 N, which was observed as 612.06 N in the numerical analysis. Densification point was found 13.26 mm. and 13.18 mm. in the experiment and numerical, respectively. The deformation behavior observed in the tests with numerical analysis for the points a,b,c,d in Figure 4.23 and the folding forms in the diagonal cross-section are shown.

Deformation behavior similar to that of the single-cell structure was observed in multiple cells as well. As explained in the previous section, twisting and global bending deformation behavior were noted in the center of the structure. Following the deformation behavior, one peak force was recorded in the force-displacement curve.

The SAE vs. displacement curve is given in Figure 4.24. The SAE value as a result of this curve taken up to the densification point was found to be 0.228 kJ/kg at 13.26 mm

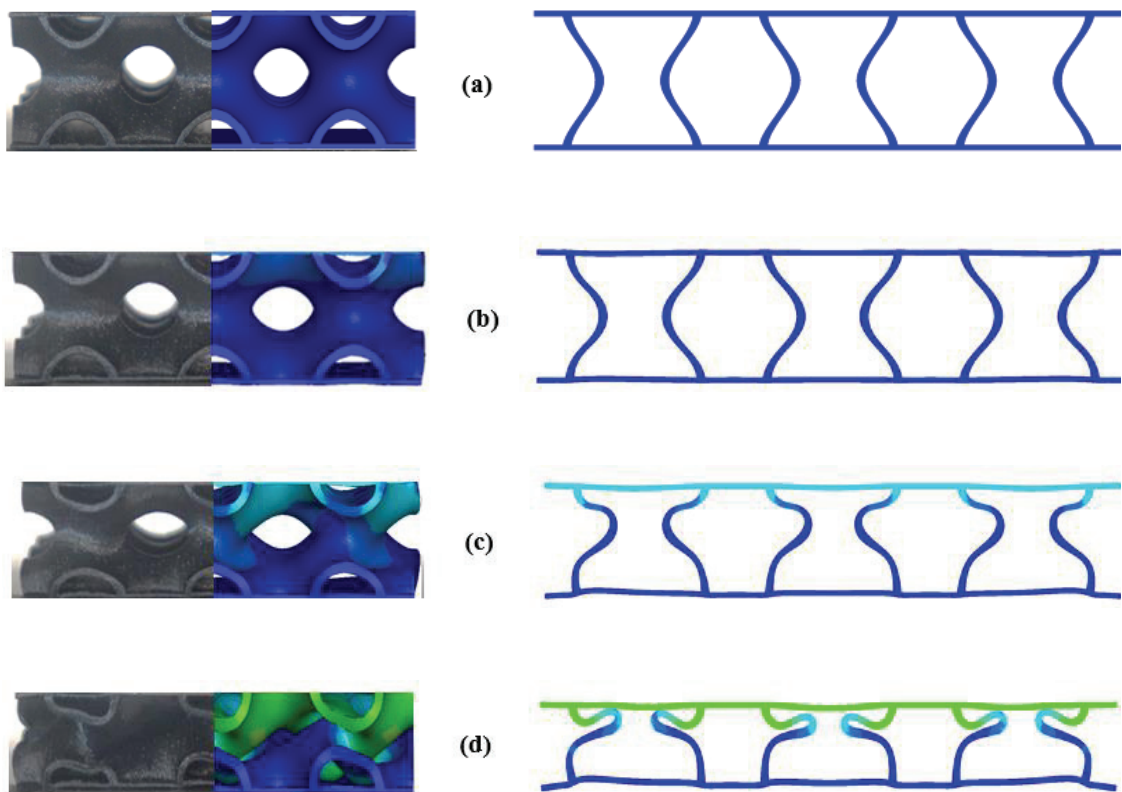
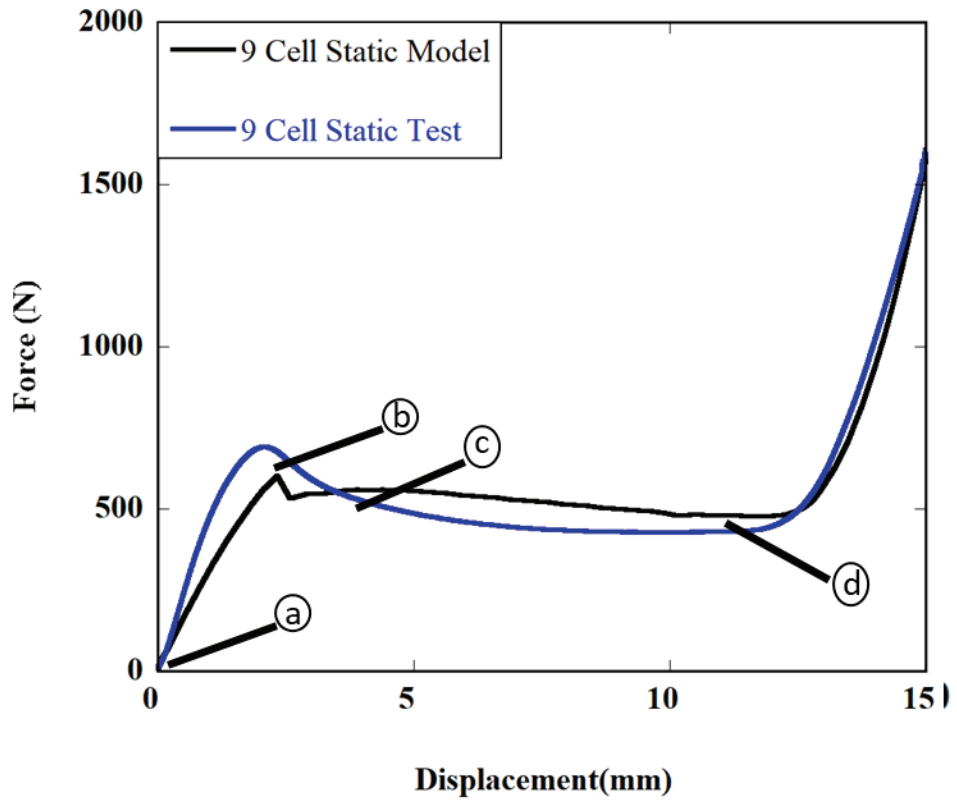


Figure 4.23. Experimental and numerical quasi-static compression force-displacement curves of the TPMS 9 cell at (a) 0 mm. (b) 2.2 mm. (c) 4.1 mm. (d) 11.4mm.

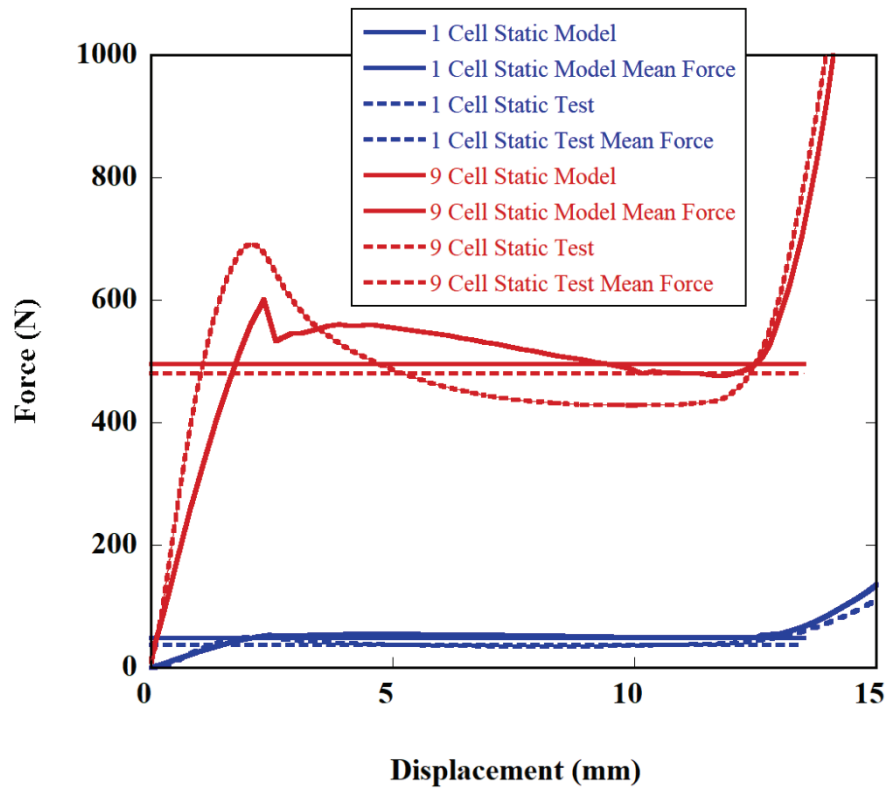


Figure 4.24. SAE vs. displacement curves comparison of TPMS multi-core structures

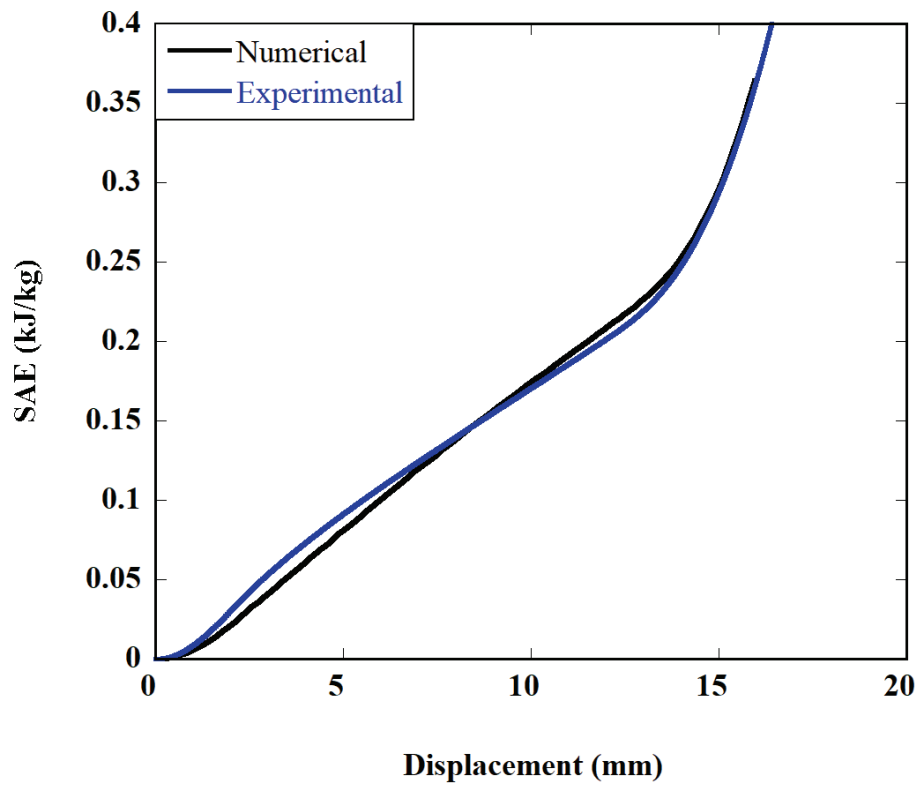


Figure 4.25. Force vs. displacement and mean force comparison of unit cell and 9 cell structures

for 9 cells. In the numerical model, there was a good agreement for SAE, and the value was close to what was observed in the experiment, i.e., 0.23 kJ/kg.

Figure 4.21 shows the force vs. displacement curves obtained from the tests and the average force curves of the sandwich structures with 9 cells and unit cell. In the structure with unit cell, the average force in the test was 50.53 N; in the numerical model, it was 48.56 N. For 9 cells, the average force for the test and numerical model was 470.01 N and 477.97 N, respectively. With these results, the difference was 4.06% for unit cell and 1.66% for 9 cells.

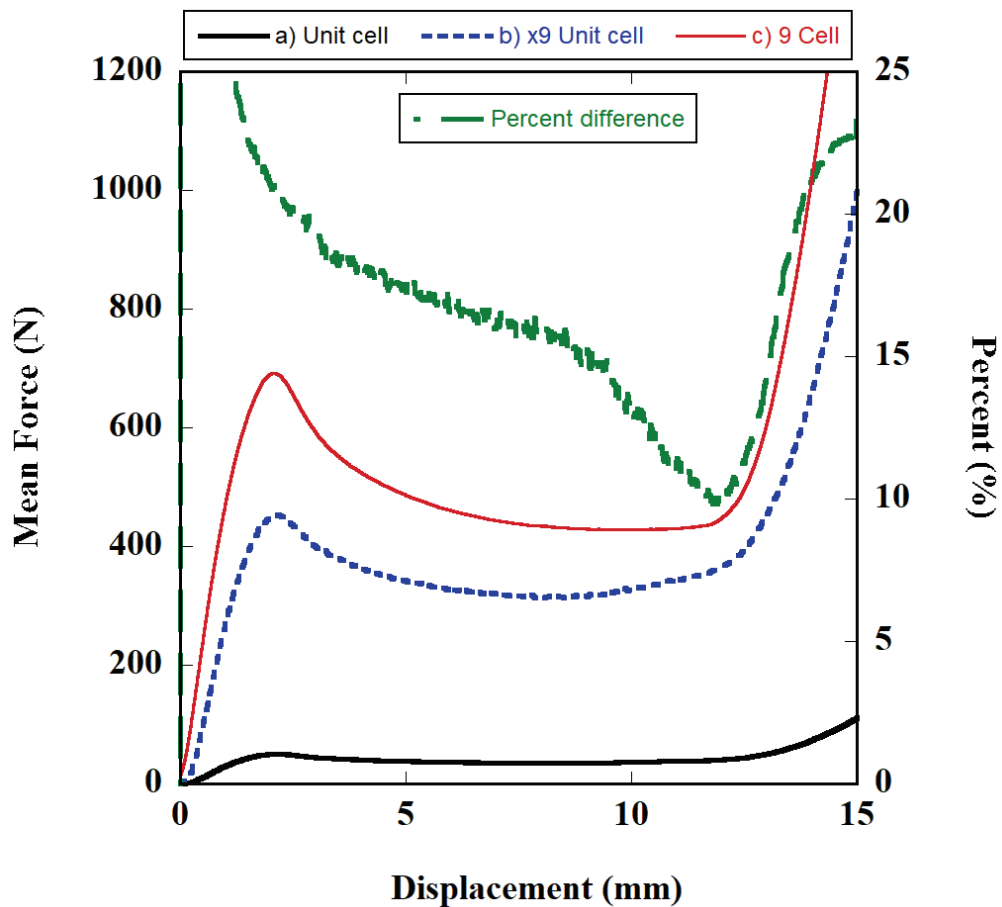


Figure 4.26. Comparison of force vs. displacement curves of numerical TPU TPMS structure and experiment for single core multiplied by 9 at static test.

Specifically, the result of a unit cell static test was multiplied by nine, then compared with the unit cell force displacement curve for static test (Figure 4.24). Additionally, the static test result with nine cores compared to distinguish cell interaction. The graph generated from this analysis clearly illustrates that cell interaction has led to a 20% increase in the peak strength of the structure (Figure 4.26). Furthermore, the pre-

buckle stiffness has also been enhanced due to cell interaction. Crucially, no early densification was observed at the densification point, providing sufficient space for the structure to resist compression. These findings demonstrate that cell interaction is critical to the structure's performance, and the analysis provides valuable insights into the underlying mechanisms.

Studies show that the force value in the plateau area nearly constant. Additionally, the difference between the expected force value before densification and the experimental value less than 10%. After analyzing the results, it was discovered that precise predictions for nine cells structures could be made with an error margin of no more than 15% compared to single-cell testing (Figure 4.25).

As seen in Figure 4.27, the numerical model underestimates the initial peak and then captures the rest of the deformation close enough. From the composite picture given in the same figure, when the crosshead hits the front face of the sandwich structure, there is a local bending effect determined by the outer diameter crosshead (in the test, the diameter of the crosshead and specimen were 70 mm., 75 mm., respectively).

As the deformation continued, the unit cell placed in the middle of the sandwich deformed anti-symmetrically, while the cell positioned close to the outer diameter of the crosshead was deformed and slightly skewed, resulting in a non-uniform deformation behavior of these cells. At later stages of the deformation, the top half of the unit cell deformed abruptly as compared bottom cell.

The cell structures started to fold, just like in the direct impact single compression test. The created numerical model successfully predicted the behavior of structures made by the additive production method when comparing deformation histories, force displacement, and SAE values in nine cell drop-weight numerical model. Although the peak force value obtained is 25% different when the test and the numerical model are compared, the characteristics of the post-peak and mean force differences found %2.2.

The densification point obtained in the tests is 14.64 mm. While in the numerical model, this value was obtained as 13.98 and the difference was found to be 4.5%.

As seen in Figure 4.27, the test and numerical results confirm each other in the drop test scenario for 9-cell TPMS structures up to the densification points. While the SAE value obtained after the drop test was 0.45 J/g, it was obtained as 0.44 J/g in the numerical analysis at 12.36 mm . Since one of the aims of the study is to provide the lowest possible energy absorption per unit mass, the SAE value is of great importance in comparisons of

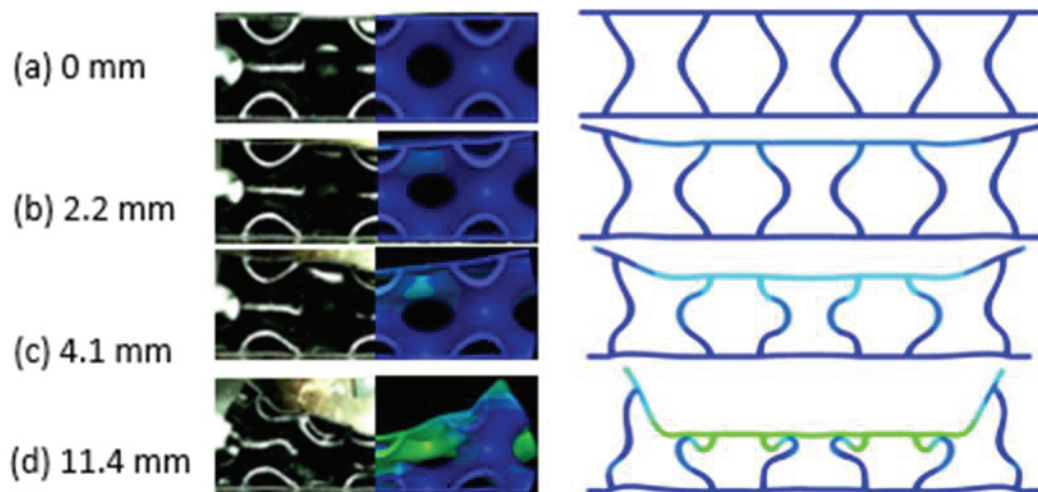
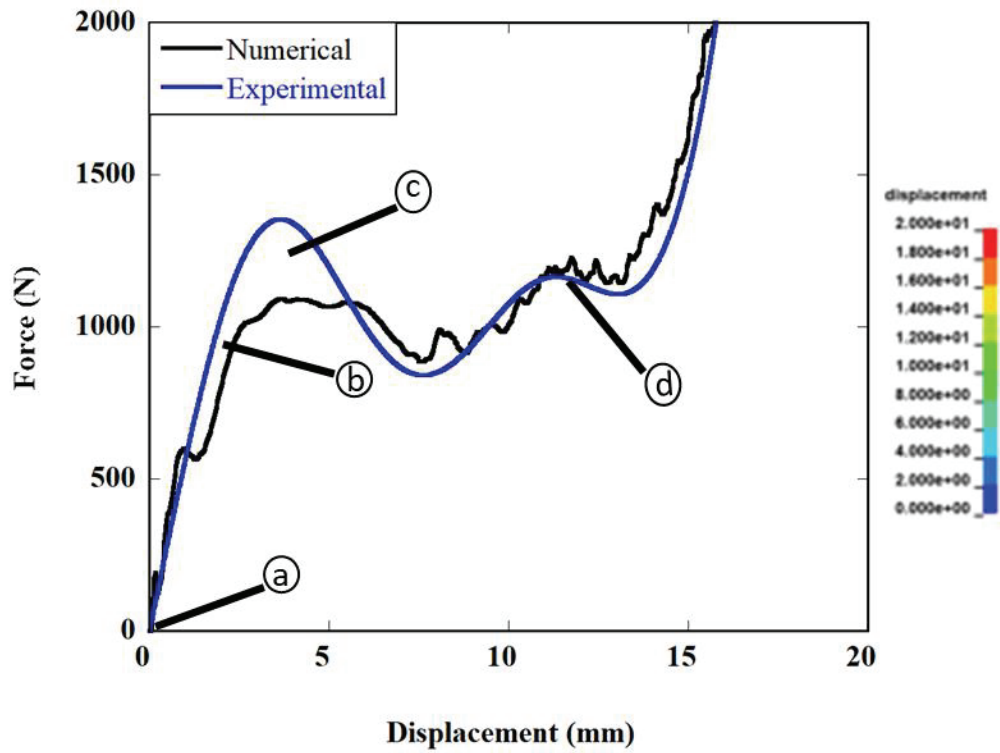


Figure 4.27. Comparison of 9 TPMS cell structure numerical and experimental drop-weight test result.

tests and numerical analysis. In the SAE results for 9 Cell drop weight, the difference between the tests and the numerical method was found to be only 2.2%, which ensures that the target value is below 10%.

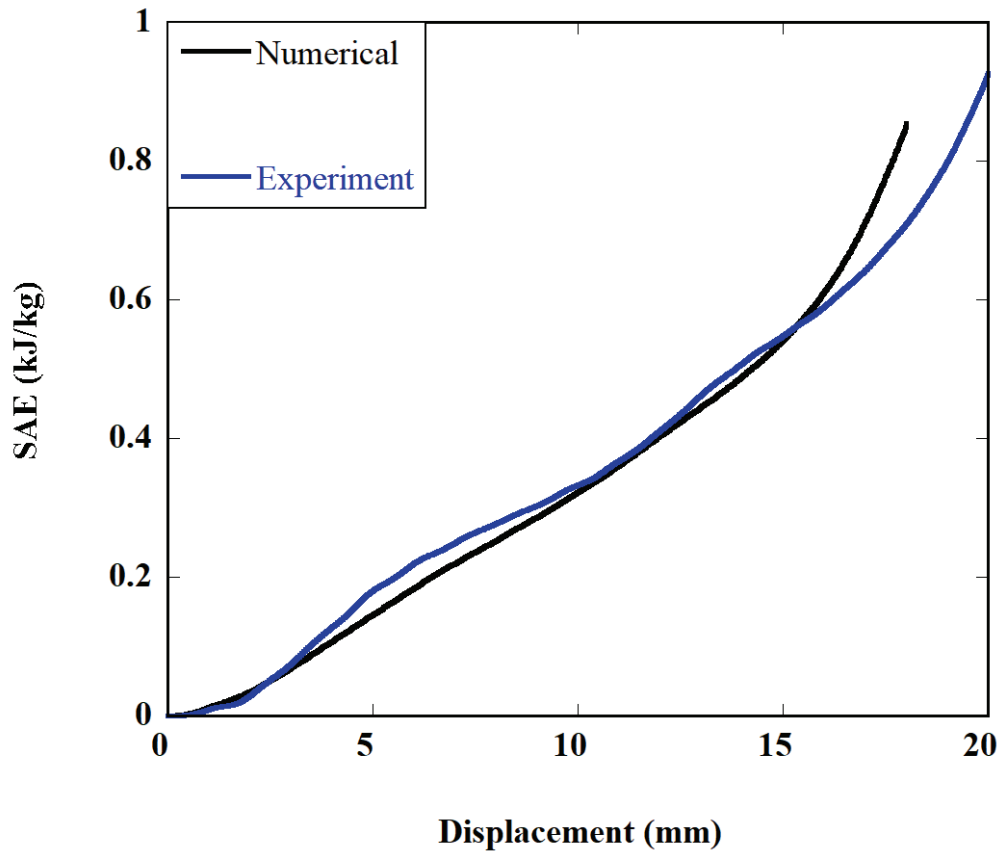


Figure 4.28. Comparison of SAE vs. displacement curves of numerical and experimental for 9 cell structures drop weight test.

The values obtained from static and dynamic tests and numerical model comparisons with 1-cell and 9-cell TPMS structures are given in Table 4.1. Also in the table, after the test was proven to be consistent with the numerical model, the 1-cell direct impact test performed analyses with the numerical model with an impactor initial velocity of 5, 15, 20, and 25 m/s. The aim here is to change the behavior of a unit cell of the structure at different strain rates to obtain the effect on SAE and crush efficiency.

According to the results obtained, the most effective velocity value of the TPU TPMS structure was found in direct impact numerical analysis with the initial velocity of the impactor of 5 m/s, and a near-perfect efficiency of 92.84% was obtained. As expected, as the impactor velocity increased, the peak and average force values increased with the effect of strain rate and inertia. The densification point of the structure, on the other hand,

Table 4.1. Comparison energy absorbtion characteristics of unit and nine cell

	Result	Test Type	Pmax (N)	Pmean (N) @12.36mm	Energy(J)	Dens. Point (mm)	SAE (J/g) @12.36mm	CE (%)	Conditions
1 CELL	Exp.	Quasi-Static	50.53	36.801	0.46	12.95	0.17	72.83	1.5 mm/min
	Num.	Quasi-Static	55.287	48.559	0.59	12.85	0.20	87.83	1.5 mm/min
	Num.	Direct Impact	132.77	123.26	1.52	13.88	0.51	92.84	5 m/s
	Exp.	Direct Impact	183.35	115.16	1.42	14.2	0.47	62.81	11 m/s
	Num.	Direct Impact	172.55	121.87	1.50	14.12	0.50	70.63	11 m/s
	Num.	Direct Impact	222.38	132.52	1.63	14.09	0.54	59.59	15 m/s
	Num.	Direct Impact	270.07	145.24	1.80	13.4	0.60	53.78	20 m/s
	Num.	Direct Impact	285.38	173.61	2.15	12.36	0.72	60.83	25 m/s
9 CELL	Exp.	Quasi-Static	691.67	470.01	5.81	13.26	0.23	67.95	1.5 mm/min
	Num.	Quasi-Static	612.06	477.97	5.91	13.18	0.22	78.09	1.5 mm/min
	Exp.	Drop-Weight	1503.14	971.31	12.01	14.64	0.45	64.75	4.21 m/s
	Num.	Drop-Weight	1118.23	949.7	11.74	13.98	0.44	86.34	4.21 m/s

became decreased as the strain rate increased in the same characterization tests, and a similar response was observed in the 1-cell structure tests. For SAE, it was found that as the deformation rate of the unit cell increased SAE of the structure also increased. This may be attributed to inherent strain rate sensitivity and the micro-inertia effect of the structure. Similar observations were also noted for nine cells. The densification point at quasistatic strain rate levels were relatively lower than those of dynamic ones, due to different deformation modes as explained in the previous section.

4.3. Numerical Results of Blast Model

In order to observe the deformation behavior of the developed structure under the blast type of loading, a comprehensive numerical analysis was carried out (Niezgoda and Wojtkowski 2013b). Before setting up the numerical model, previous studies conducted on the similar issue were investigated. Since the LSTC Hybrid III 50th Fast Dummy is used, the lower left tibia force comparison was obtained from the JT-41 joint in the model (LSTC 2011).

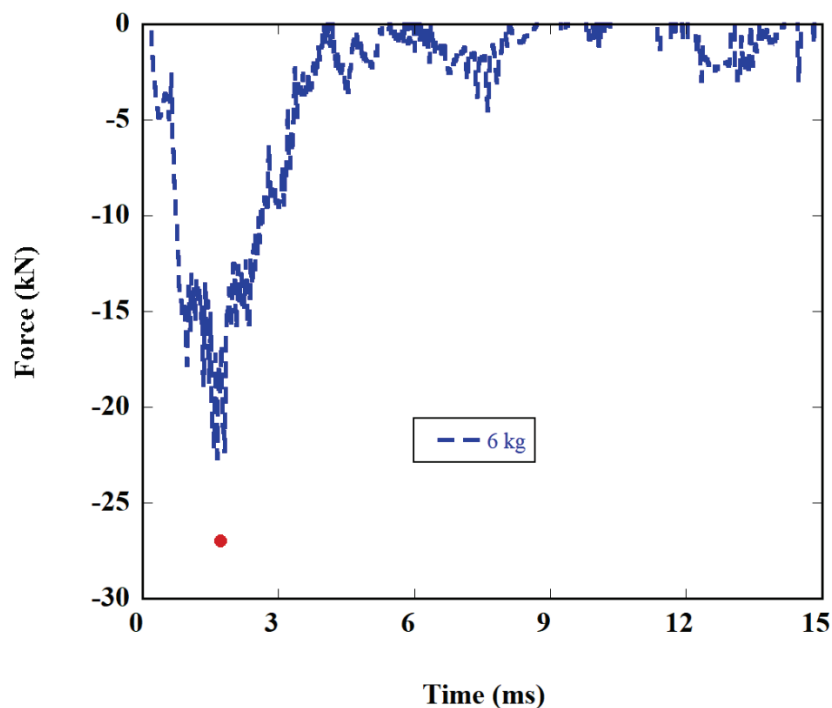


Figure 4.29. Comparison of axial force loading on the lower tibia

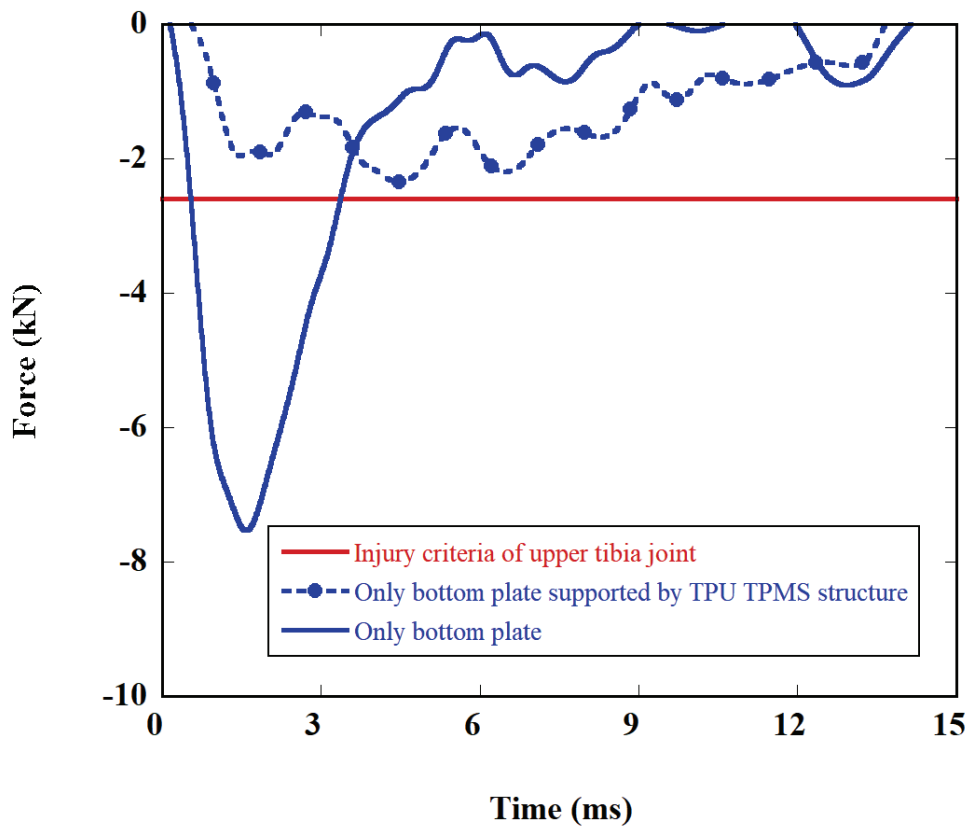
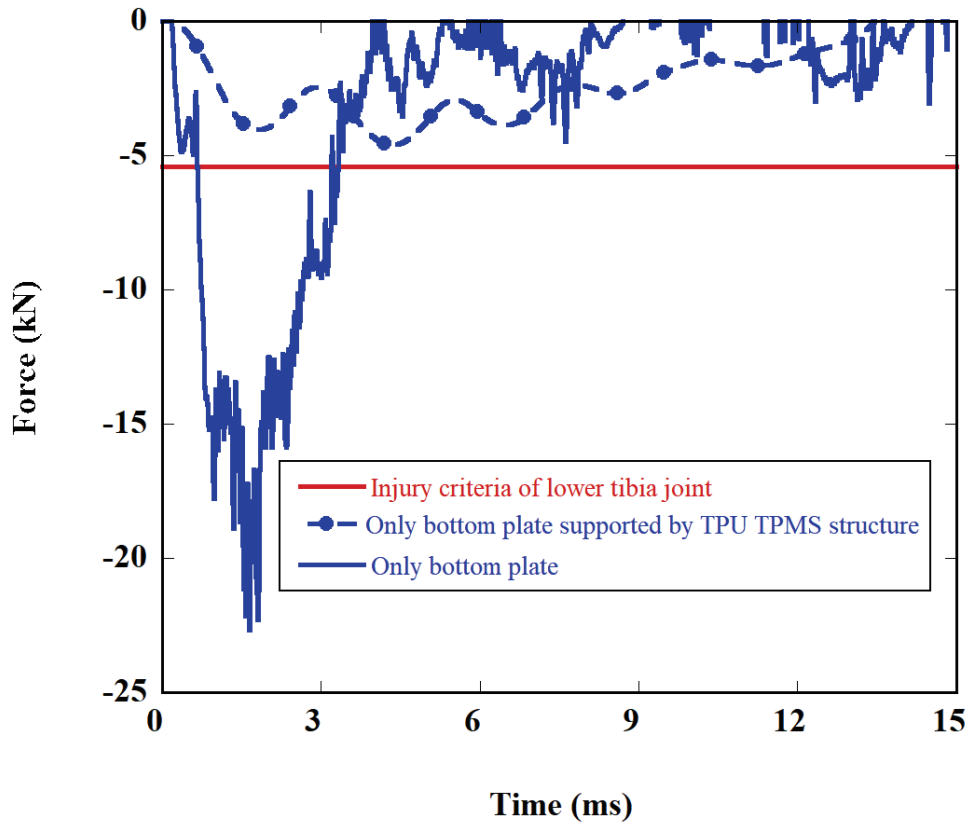


Figure 4.30. Comparison of axial compressive force on lower and upper tibia

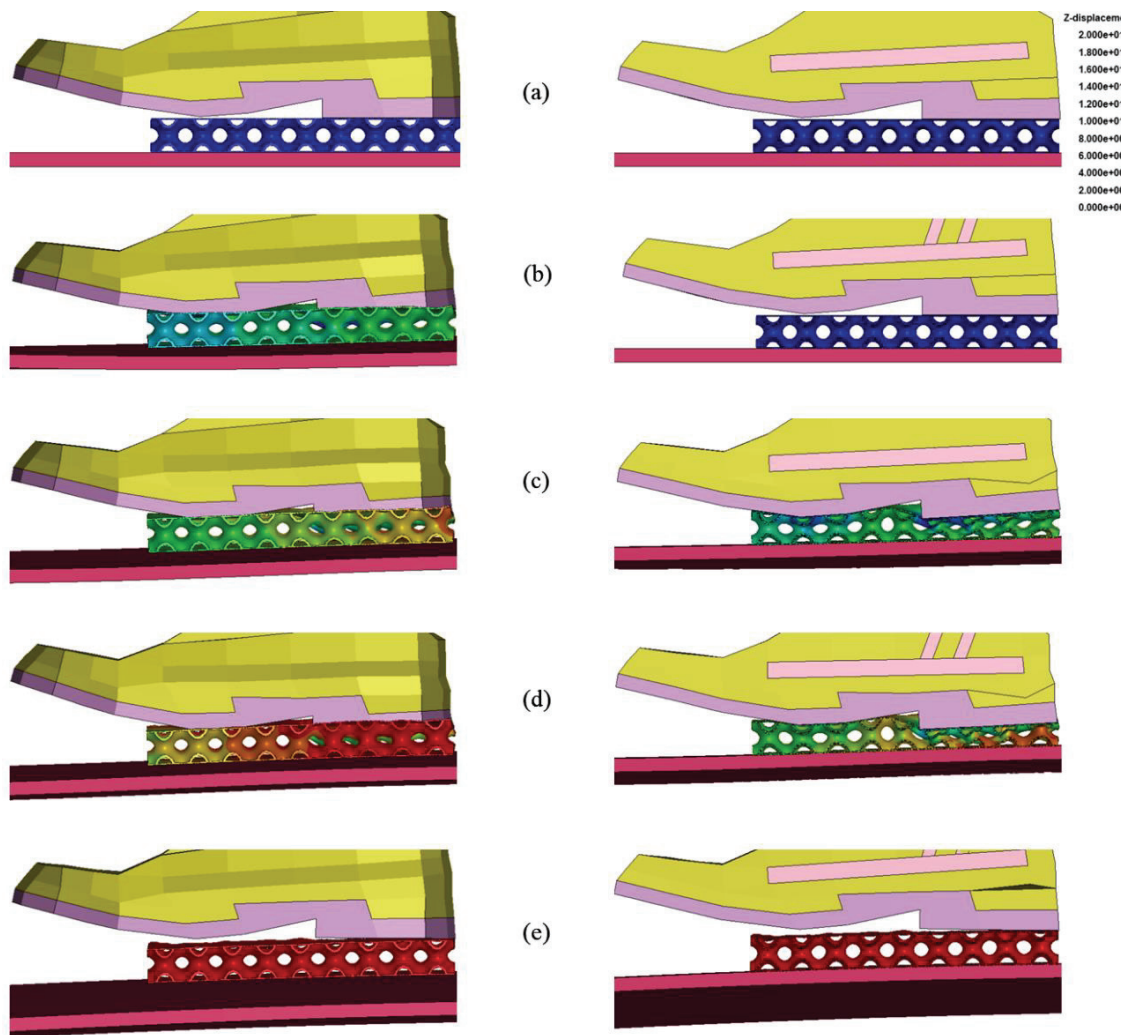


Figure 4.31. The displacement of the investigated TPU TPMS multi-core structure bottom pad at (a) 0 ms (b) 2.12 ms (c) 4.40 ms (d) 6.66 ms (e) 14.24 ms

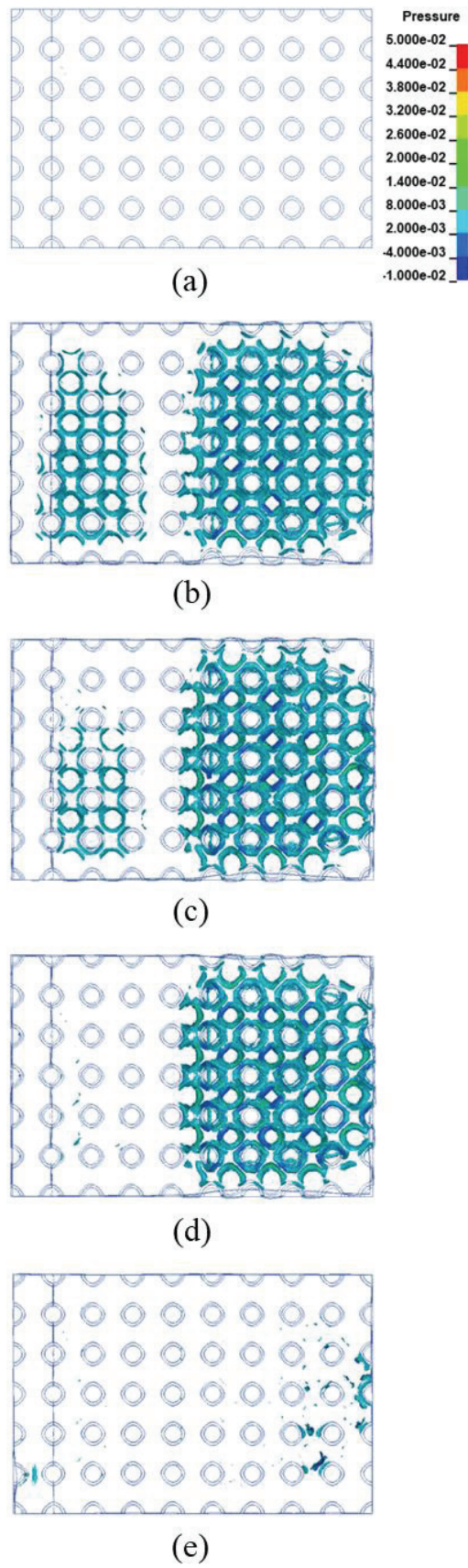


Figure 4.32. The pressure of the designed TPU TPMS multi-core structure bottom pad (a) 0 ms (b) 2.12 ms (c) 4.40 ms (d) 6.66 ms (e) 14.24 ms.

In the model based on the literature, for the numerical model with only the bottom plate, the axial force on the lower tibia was 27 kN, while in the prepared model, it was 23 kN in the compression axis. The reason for this is that although the model in the literature was prepared using the ALE method, Conweb modeling was used in the study. Afterward, the comparison of the axial force on the lower and upper tibia joint with the TPU TPMS structures only bottom plate and by using created TPU TPMS structures are shown in Figure 4.30. The Figure 4.30 also shows the maximum forces that should come to the upper and lower tibia joints according to Nato Stanag 4569 standard. In the numerical model with only the lower plate, the maximum axial force on the lower and upper tibia joint was observed as compressive axial 24 kN and 7.6 kN, respectively. In the analyzes supported by the TPU TPMS bottom pad, the maximum force for the lower tibia was 4.4 kN, and for the upper tibia joint 2.4 kN.

In addition, due to the cellular structure used, it allowed the blast energy to be mitigated by distribution it over time. In Figure 4.31, the behavior of the TPU TPMS structure under explosion load is illustrated and also shown in the cross-section. It was observed that the cells were deformed, especially in the heel region, with the acceleration of the substrate by the effect of the pressure wave. The pressure value observed on the pad fixed to the floor plate depending on the displacement, iso image with the help of Isprepost was examined in Figure 4.32. Although the back and middle parts of the foot compressed the structure with the effect of the pressure wave, it was observed that it only concentrated in the heel area after 6 ms. Since no failure was used in the material model, it was stated that the pressure was decreased from the TPU TPMS structure after 14 ms.

CHAPTER 5

CONCLUSIONS

The goal of this thesis was to create a cell structure with improved mechanical characteristics and increased impact energy absorption. The energy absorbers must have the lowest possible density and the maximum impact energy absorption capacity. In order to further enhance energy absorption capability at relatively lower weights, TPMS primitive schwarz was used. To obtain deformation behavior of compression and energy absorption, the TPU TPMS structure was used to quasi-static compression and dynamic impact both experimentally and numerically. Additionally, verified experimentally numerical models in the LS-DYNA software were used to observe the strain rate and inertia effects of the structure.

Briefly summarized experimental and numerical observations are listed below in detail:

Fused Deposition Modeling (FDM), a method of additive manufacturing also known as 3D printing, was chosen due to the complex structure of the designed core geometry because it allowed for the production of complex geometries and shapes thanks to its manufacturing method, which is based on layer-by-layer production. Since thermoplastic polyurethane is difficult to produce with FDM due to its high elasticity, the applied methodology is explained and the printer parameters used are clearly stated.

It has been determined that the gaps between the layers can be minimized and the quality of the samples printed by removing moisture from the TPU filament before production increases by changing the operating parameters of the 3D printer in terms of scanning angle, feed rate, the temperature difference between the platform and the nozzle, and infill density.

Since there are no existing test standards at dynamic strain rate for 3D printed materials and the dynamic characterization is crucial for hyperelastic materials due to their known strain rate sensitivity, suitable testing samples and procedures were designed to describe the 3D printed TPU samples. Under both static and dynamic loads, the mechanical characterization tests were carried out, and the impacts of strain rate and stress-strain relations on compressive strength were identified.

The observed material curves and constants are anisotropic due to the production process, as the characterization specimens were produced by FDM and employed 45/-45 infill parameters, however, the procedure was carried out assuming isotropic in Ls-dyna, and the results were obtained.

LS-DYNA software was used to carry out numerical validations. The force-displacement curves from the numerical analyses and the experiments agree well. Since the characteristic stress is compressively dominant, the failure was not taken into consideration in the implicit and explicit analysis. As a result, numerical observations of layer separation on the structure were not considered. On the other hand, both experimental and numerical tests found that the structure's compressive behavior was identical.

Under static and dynamic loads, the single and multiple core structure's energy absorption characteristics were studied numerically and experimentally. To determine the model's correctness, the energy-absorbing behaviors and deformation histories were compared.

Comparing the results of the quasi-static test with the numerical simulations of the direct impact test, both strain rate and inertia impact on the compressive behavior of the structure were examined. The strain rate effect was increased to a ratio of 60% during the buckling beginning stage, whereas the inertia effect reduced by about 40%.

In comparison to individual 3-D printed core geometry, it was shown that the TPU TPMS sandwich structures made up of 9 cells could absorb 20% more impact energy.

Since the peak force increases with increasing strain rates, the mean force value increases for increasing strain rates. Since the structure shows buckle without being folded, the plateau phase in the force-displacement curve goes at peak force levels. Therefore, the compression efficiency is high where initial velocity 5 m/s in direct impact numerical models. As the strain rate increased, it was determined that the densification point was at earlier levels in the tests and analyses performed with a unit cell, as seen in the same characterization tests.

The effect of 3-D printing on mechanical properties and strain rate sensitive behavior of thermoplastic material was found to be similar to that of experiments using a developed material model that takes static and dynamic characterization curves as input. It has been observed that the compressive characteristic of the structure changes after the impactor initial velocity of 5 m/s for a unit cell, depending on the strain rate.

In the case examined for the 6 kg TNT and 500 mm burst distance scenario prepared with the Conweb method, it was observed that the peak force of the TPU TPMS structure used was 20% and 9.2% lower than the maximum axial force limits specified for the lower and upper tibia bones, respectively. It shows the unique sandwich structure's encouraging potential for use in crashworthiness applications.

Future work recommendations:

It can be investigated how the strength of the sample is affected by the changes in important parameters for 3D manufacturing, such as the infill angle used and nozzle temperature values.

Analyzes of the TPU TPMS structure used in the thesis for different usage areas such as sports, transportation, and maritime can be performed and optimization studies can be carried out following the specified sectors.

The necessary tests can be made for the unloading part of the material in the material model used, and the Mullins effect observed in the structure in hysteresis cases can be investigated.

Dynamic tensile test methodology can be developed for TPU material produced by additive manufacturing.

For the explosion model, solutions can be obtained with full-scale analysis by using ALE or S-ALE methods.

REFERENCES

- Abdulhameed, Osama, Abdulrahman Al-Ahmari, Wadea Ameen, and Syed Hammad Mian. 2019. "Additive Manufacturing: Challenges, Trends, and Applications." *Advances in Mechanical Engineering* 11 (2): 1–27. <https://doi.org/10.1177/1687814018822880>.
- "Airless Tyres for Military Humvee." 2021. 2021. theawesomer.com.
- ANSYS. 2002. "Mechanical-A Powerful Nonlinear Simulation Tool."
- Aquino, D. A. de, I. Maskery, G. A. Longhitano, A. L. Jardini, and E. G. del Conte. 2020. "Investigation of Load Direction on the Compressive Strength of Additively Manufactured Triply Periodic Minimal Surface Scaffolds." *International Journal of Advanced Manufacturing Technology* 109 (3–4): 771–79. <https://doi.org/10.1007/s00170-020-05706-y>.
- Baranowski, Paweł, Jerzy Małachowski, Łukasz Mazurkiewicz, and Krzysztof Damaziak. 2013. "Rubber Structural Coupon Behaviour Study under Pressure Impulse." *Solid State Phenomena* 198: 394–99. <https://doi.org/10.4028/www.scientific.net/SSP.198.394>.
- Bird, David T., and Nuggehalli M. Ravindra. 2021. "Additive Manufacturing of Sensors for Military Monitoring Applications." *Polymers* 13 (9). <https://doi.org/10.3390/polym13091455>.
- Bondy, Matthew. 2013. "Scholarship at UWindsor Development of Procedures for Accurate Finite Element Modeling of the Dynamic and Quasi-Static Performance of Automotive Chassis Components Incorporating Hyperelastic Materials."
- Calladine, C. R., and R. W. English. 1984. "Strain-Rate and Inertia Effects in the Collapse of Two Types of Energy-Absorbing Structure." *International Journal of Mechanical Sciences* 26 (11–12): 689–701. [https://doi.org/10.1016/0020-7403\(84\)90021-3](https://doi.org/10.1016/0020-7403(84)90021-3).
- Camirero, M A. 2017. "Additive Manufacturing OfPLA Structures Using Fused Deposition Modelling: Effect of Process Parameters on Mechanical Properties and Their Optimal Selection." <https://doi.org/10.1016/j.matdes.2017.03.065>.
- Charlton, D. J., J. Yang, and K. K. Teh. 1994. "Review of Methods to Characterize Rubber Elastic Behavior for Use in Finite Element Analysis." *Rubber Chemistry and Technology*. <https://doi.org/10.5254/1.3538686>.
- Chaudhry, Muhammad Salman, and Aleksander Czekanski. 2020. "Evaluating FDM Process Parameter Sensitive Mechanical Performance of Elastomers at Various Strain Rates of Loading," no. Figure 1: 1–10.
- Chu, Chen, Greg Graf, and David W. Rosen. 2008. "Design for Additive Manufacturing of Cellular Structures." *Computer-Aided Design and Applications* 5 (5): 686–96. <https://doi.org/10.3722/cadaps.2008.686-696>.

- Davis, Sol. 1972. "Application of the Shock Response Spectrum to Some Automotive Crashworthiness Problems." *SAE Technical Papers*. <https://doi.org/10.4271/720071>.
- Diosdado-De la Peña, Jose Angel, Charles M. Dwyer, David Krzeminski, Eric MacDonald, Alberto Saldaña-Robles, Pedro Cortes, and Kyosung Choo. 2022. "Low Impact Velocity Modeling of 3D Printed Spatially Graded Elastomeric Lattices." *Polymers* 14 (21). <https://doi.org/10.3390/polym14214780>.
- Donath, Steffen. 2019. "3D Printing a Rocket Engine." *Etm*. <https://www.etmm-online.com/3d-printing-a-rocket-engine-a-886960/>.
- Engelbrektsson, Kristofer. 2011. "Evaluation of Material Models in LS-DYNA for Impact Simulation of White Adipose Tissue."
- Erdik, Atil, Namik Kilic, and Hakan Ak. 2014. "May 1 n Patlama Simülasyonlar ı Nda Üç Farklı Yöntemin İncelenmesi : CONWEP , MM-ALE ve Birleşik CONWEP-ALE," no. June.
- Finney, Robert H., and Alok Kumar. 1988. "Development of Material Constants for Nonlinear Finite-Element Analysis." *Rubber Chemistry and Technology*. <https://doi.org/10.5254/1.3536224>.
- Hohimer, Cameron, Josef Christ, Nahal Aliheidari, Changki Mo, Amir Ameli, and Crimson Way. 2017. "3D Printed Thermoplastic Polyurethane with Isotropic Material Properties" 10165: 1–9. <https://doi.org/10.1117/12.2259810>.
- Huang, Zhixin, Ying Li, Xiong Zhang, Wei Chen, and Daining Fang. 2021. "A Comparative Study on the Energy Absorption Mechanism of Aluminum/CFRP Hybrid Beams under Quasi-Static and Dynamic Bending." *Thin-Walled Structures* 163 (January): 107772. <https://doi.org/10.1016/j.tws.2021.107772>.
- Jamil, Adil. 2018. "Structural Response of Novel PU Structures under Quasi-Static , Impact and Blast Loading - Experimental and Numerical Analyses By." <https://livrepository.liverpool.ac.uk/id/eprint/3018626>.
- Javaid, Mohd, Abid Haleem, Ravi Pratap Singh, Rajiv Suman, and Shanay Rab. 2021. "Role of Additive Manufacturing Applications towards Environmental Sustainability." *Advanced Industrial and Engineering Polymer Research* 4 (4): 312–22. <https://doi.org/10.1016/j.aiepr.2021.07.005>.
- Jiang, Binhui, Feng Zhu, Xin Jin, Libo Cao, and King H Yang. 2013. "Computational Modeling of the Crushing Behavior of SKYDEX Ò Material Using Homogenized Material Laws." *Composite Structures* 106: 306–16. <https://doi.org/10.1016/j.compstruct.2013.06.011>.
- Jin, Yu An, Hui Li, Yong He, and Jian Zhong Fu. 2015. "Quantitative Analysis of Surface Profile in Fused Deposition Modelling." *Additive Manufacturing* 8: 142–48. <https://doi.org/10.1016/j.addma.2015.10.001>.

- Juang, Yi-Xian Xu and Jia-Yang. 2021. "Measurement of Nonlinear Poisson ' s Ratio of Thermoplastic Polyurethanes under Cyclic Softening Using 2D Digital."
- Kanu, Rex C., Caleb Hale, and Patrick O.Neal Piper. 2016. "The Use of 3D Printing to Introduce Students to ASTM Standards for Testing Tensile Properties of Acrylonitrile-Butadiene-Styrene (ABS) Plastic Material." *ASEE Annual Conference and Exposition, Conference Proceedings* 2016-June. <https://doi.org/10.18260/p.27027>.
- Khorram Niaki, Mojtaba, Fabio Nonino, Giulia Palombi, and S. Ali Torabi. 2019. "Economic Sustainability of Additive Manufacturing: Contextual Factors Driving Its Performance in Rapid Prototyping." *Journal of Manufacturing Technology Management* 30 (2): 353–65. <https://doi.org/10.1108/JMTM-05-2018-0131>.
- Kingery, C. No. 1966. "Air Blast Parameters Versus Distance For Hemispherical Tnt Surface Bursts."
- Kladovasilakis, Nikolaos, Konstantinos Tsongas, and Dimitrios Tzetzis. 2020. "Finite Element Analysis of Orthopedic Hip Implant with Functionally Graded Bioinspired Lattice Structures." *Biomimetics* 5 (3). <https://doi.org/10.3390/BIOMIMETICS5030044>.
- Laurin, Frederick, and Anthony J Vizzini. 2005. "Journal of Sandwich Structures and Materials Energy Absorption of Sandwich Panels." <https://doi.org/10.1177/1099636205047888>.
- LSTC. 2005. *Theory Manual*. Vol. 22.
- LSTC, 2011. "LSTC Hybrid III 50 Fast Dummy."
- LSTC, 2012. "Contact in LS-DYNA - Practical Guidelines."
- LSTC, 2021. "R13 Manual Volume I" I (February). www.lstc.com.
- LSTC, 2021. "R13 Manual Volume II" II (October): 1993. www.lstc.com.
- LSTC, 2013. "Numerical Analysis Of The Influence" 20 (3): 1–6.
- Lu, Guoxing, and Tongxi Yu. 2003. *Energy Absorption of Structures and Materials*. <https://doi.org/10.1533/9781855738584>.
- Martin. n.d. "PLA vs ABS, PETG, TPU for 3D Printing | Comparison & Guide."
- Maskery, I., L. Sturm, A. O. Aremu, A. Panesar, C. B. Williams, C. J. Tuck, R. D. Wildman, I. A. Ashcroft, and R. J.M. Hague. 2018. "Insights into the Mechanical Properties of Several Triply Periodic Minimal Surface Lattice Structures Made by Polymer Additive Manufacturing." *Polymer* 152 (September): 62–71. <https://doi.org/10.1016/j.polymer.2017.11.049>.

- McCreight, Cayleigh. 2022. "What Equations Are Used to Create the TPMS Types?" 2022. <https://support.ntopology.com/hc/en-us/articles/360053267814-What-equations-are-used-to-create-the-TPMS-types->.
- McHenry, Raymond R., and Patrick M. Miller. 1970. "State-of-the-Art - Automobile Structural Crashworthiness." *SAE Technical Papers*. <https://doi.org/10.4271/700412>.
- Miralbes, R., D. Ranz, F. J. Pascual, D. Zouzas, and M. Maza. 2020. "Characterization of Additively Manufactured Triply Periodic Minimal Surface Structures under Compressive Loading." *Mechanics of Advanced Materials and Structures*. <https://doi.org/10.1080/15376494.2020.1842948>.
- Mishra, Ashish Kumar, Hrushikesh Chavan, and Arvind Kumar. 2021. "Effect of Material Variation on the Uniaxial Compression Behavior of FDM Manufactured Polymeric TPMS Lattice Materials." *Materials Today: Proceedings* 46: 7752–59. <https://doi.org/10.1016/j.matpr.2021.02.276>.
- Mooney, M. 1940. "A Theory of Large Elastic Deformation." *Journal of Applied Physics* 11 (9): 582–92. <https://doi.org/10.1063/1.1712836>.
- Niezgoda, Tadeusz, and Marcin Wojtkowski. 2013a. "Numerical Analysis Of The Influence" 20 (3).
- Novak, Nejc, Oraib Al-Ketan, Anja Mauko, Yunus Emre Yilmaz, Lovre Krstulović-Opara, Shigeru Tanaka, Kazuyuki Hokamoto, et al. 2023. "Impact Loading of Additively Manufactured Metallic Stochastic Sheet-Based Cellular Material." *International Journal of Impact Engineering* 174 (January). <https://doi.org/10.1016/j.ijimpeng.2023.104527>.
- Orme, Melissa E., Michael Gschweidl, Michael Ferrari, Russell Vernon, Ivan J. Madera, Robert Yancey, and Franck Mouriaux. 2017. "Additive Manufacturing of Lightweight, Optimized, Metallic Components Suitable for Space Flight." *Journal of Spacecraft and Rockets* 54 (5): 1050–59. <https://doi.org/10.2514/1.A33749>.
- Palanivelu, Sivakumar, Wim Van Paeppegem, Joris Degrieck, John Vantomme, Dimitrios Kakogiannis, Johan Van Ackeren, Danny Van Hemelrijck, and Jan Wastiels. 2011. "Crushing and Energy Absorption Performance of Different Geometrical Shapes of Small-Scale Glass/Polyester Composite Tubes under Quasi-Static Loading Conditions." *Composite Structures* 93 (2): 992–1007. <https://doi.org/10.1016/j.compstruct.2010.06.021>.
- Papon, Easir Arafat, and Anwarul Haque. 2018. "Tensile Properties, Void Contents, Dispersion and Fracture Behaviour of 3D Printed Carbon Nanofiber Reinforced Composites." *Journal of Reinforced Plastics and Composites* 37 (6): 381–95. <https://doi.org/10.1177/0731684417750477>.
- Pavlenko, Ivan, Milan Edl, and Ivan Kuric. 2020. *Advanced Manufacturing Processes II Selected Papers from The*.

- Plątek, Paweł, Kamil Rajkowski, Kamil Cieplak, Marcin Sarzyński, Jerzy Małachowski, Ryszard Woźniak, and Jacek Janiszewski. 2020. "Deformation Process of 3D Printed Structures Made from Flexible Material with Different Values of Relative Density." *Polymers* 12 (9). <https://doi.org/10.3390/POLYM12092120>.
- Plessis, Anton du, Seyed Mohammad Javad Razavi, Matteo Benedetti, Simone Murchio, Martin Leary, Marcus Watson, Dhruv Bhate, and Filippo Berto. 2022. "Properties and Applications of Additively Manufactured Metallic Cellular Materials: A Review." *Progress in Materials Science* 125 (December 2021): 100918. <https://doi.org/10.1016/j.pmatsci.2021.100918>.
- Pollard, David, C. Ward, G. Herrmann, and J. Etches. 2017. "The Manufacture of Honeycomb Cores Using Fused Deposition Modeling." *Advanced Manufacturing: Polymer and Composites Science* 3 (1): 21–31. <https://doi.org/10.1080/20550340.2017.1306337>.
- Qi, H. J., and M. C. Boyce. 2005. "Stress-Strain Behavior of Thermoplastic Polyurethanes." *Mechanics of Materials* 37 (8): 817–39. <https://doi.org/10.1016/j.mechmat.2004.08.001>.
- Quenneville, Cheryl E., Ed Fournier, and Nicholas Shewchenko. 2017. "The Effect of Anthropomorphic Test Device Lower Leg Surrogate Selection on Impact Mitigating System Evaluation in Low- and High-Rate Loading Conditions." *Military Medicine* 182 (9): e1981–86. <https://doi.org/10.7205/MILMED-D-16-00358>.
- Raman, S. N., T. Ngo, and P. Mendis. 2011. "A Review on the Use of Polymeric Coatings for Retrofitting of Structural Elements against Blast Effects." *Electronic Journal of Structural Engineering* 11 (May): 69–80. <https://doi.org/10.56748/ejse.11144>.
- Restrepo, S., S. Ocampo, J. A. Ramirez, C. Paucar, and C. Garcia. 2017. "Mechanical Properties of Ceramic Structures Based on Triply Periodic Minimal Surface (TPMS) Processed by 3D Printing." *Journal of Physics: Conference Series* 935 (1): 8–14. <https://doi.org/10.1088/1742-6596/935/1/012036>.
- Rohbeck, Nadia, Rajaprakash Ramachandramoorthy, Daniele Casari, Patrik Schürch, Thomas E.J. Edwards, Laura Schilinsky, Laetitia Philippe, Jakob Schwiedrzik, and Johann Michler. 2020. "Effect of High Strain Rates and Temperature on the Micromechanical Properties of 3D-Printed Polymer Structures Made by Two-Photon Lithography." *Materials and Design* 195: 108977. <https://doi.org/10.1016/j.matdes.2020.108977>.
- Sarva, Sai S., Stephanie Deschanel, Mary C. Boyce, and Weinong Chen. 2007. "Stress-Strain Behavior of a Polyurea and a Polyurethane from Low to High Strain Rates." *Polymer* 48 (8): 2208–13. <https://doi.org/10.1016/j.polymer.2007.02.058>.
- Schaedler, Tobias A., Christopher J. Ro, Adam E. Sorensen, Zak Eckel, Sophia S. Yang, William B. Carter, and Alan J. Jacobsen. 2014. "Designing Metallic Microlattices for Energy Absorber Applications." *Advanced Engineering Materials* 16 (3): 276–83. <https://doi.org/10.1002/adem.201300206>.

- Schollenbenger, C.S., Scott, H., Moore, G.R. 1958. "Polyurethane VC, a Virtually Crosslinked Elastomer."
- Seepersad, Carolyn C, and Richard H Crawford. n.d. "Topology Optimization for Additive Manufacturing of Customized Meso-Structures Using Homogenization and Parametric Smoothing Functions Approved By Supervising Committee."
- Shepherd, Todd, Keith Winwood, Prabhuraj Venkatraman, Andrew Alderson, and Thomas Allen. 2020. "Validation of a Finite Element Modeling Process for Auxetic Structures under Impact," no. April. <https://doi.org/10.1002/pssb.201900197>.
- Shields, Gerard. 2022. "3D Printing Support Structures – The Ultimate Guide." <https://all3dp.com/1/3d-printing-lattice-structures-the-ultimate-guide/>.
- Siviour, Clive R. 2015. "High Strain Rate Characterization of Polymers," 8–13. <https://doi.org/10.1063/1.4971585>.
- Su, X. Y., T. X. Yu, and S. R. Reid. 1995. "Inertia-Sensitive Impact Energy-Absorbing Structures Part I: Effects of Inertia and Elasticity." *International Journal of Impact Engineering* 16 (4): 651–72. [https://doi.org/10.1016/0734-743X\(94\)00061-Z](https://doi.org/10.1016/0734-743X(94)00061-Z).
- Sundaramurthy, Aravind, Aaron Alai, Shailesh Ganpule, Aaron Holmberg, Erwan Plougonven, and Namas Chandra. 2012. "Blast-Induced Biomechanical Loading of the Rat : An Experimental and Anatomically Accurate Computational Blast Injury Model" 2364: 2352–64. <https://doi.org/10.1089/neu.2012.2413>.
- Tam, L. L., and C. R. Calladine. 1991. "Inertia and Strain-Rate Effects in a Simple Plate-Structure under Impact Loading." *International Journal of Impact Engineering* 11 (3): 349–77. [https://doi.org/10.1016/0734-743X\(91\)90044-G](https://doi.org/10.1016/0734-743X(91)90044-G).
- Ursini, Chiara, and Luca Collini. 2021. "Fdm Layering Deposition Effects on Mechanical Response of Tpu Lattice Structures." *Materials* 14 (19). <https://doi.org/10.3390/ma14195645>.
- Verhoef, Leendert A., Bart W. Budde, Cindhuja Chockalingam, Brais García Nodar, and Ad J.M. van Wijk. 2018. "The Effect of Additive Manufacturing on Global Energy Demand: An Assessment Using a Bottom-up Approach." *Energy Policy* 112 (November 2017): 349–60. <https://doi.org/10.1016/j.enpol.2017.10.034>.
- Vidakis, Nectarios, Markos Petousis, Apostolos Korlos, Emmanouil Velidakis, Nikolaos Mountakis, Chrisa Charou, and Adrian Myftari. 2021. "Strain Rate Sensitivity of Polycarbonate and Thermoplastic Polyurethane for Various 3d Printing Temperatures and Layer Heights." *Polymers* 13 (16). <https://doi.org/10.3390/polym13162752>.
- Vimal Kannan, I., and R. Rajkumar. 2020. "Deformation and Energy Absorption Analysis of Simple and Multi-Cell Thin-Walled Tubes under Quasi-Static Axial Crushing." *International Journal of Crashworthiness* 25 (2): 121–30. <https://doi.org/10.1080/13588265.2018.1542956>.

- Webbe, Tomas, Hyoungjun Lim, Woong Yeol, and Gun Jin. 2019. "Characterization of Process – Deformation / Damage Property Relationship of Fused Deposition Modeling (FDM) 3D-Printed Specimens." *Additive Manufacturing* 25 (December 2018): 532–44. <https://doi.org/10.1016/j.addma.2018.11.008>.
- Wierzbicki, T. 2004. *Energy Absorption of Structures and Materials. International Journal of Impact Engineering*. Vol. 30. <https://doi.org/10.1016/j.ijimpeng.2003.12.004>.
- Williams, Kevin, Scott Mcclennan, Robert Durocher, Benoit St-jean, and Jocelyn Tremblay. 2002. "7 Th International LS-DYNA Users Conference Penetration / Explosive Validation of a Loading Model for Simulating Blast Mine Effects on Armoured Vehicles," 35–44.
- Wong, Kaufui V., and Aldo Hernandez. 2012. "A Review of Additive Manufacturing." *ISRN Mechanical Engineering* 2012: 1–10. <https://doi.org/10.5402/2012/208760>.
- Wu, Haishang, Hamid Mehrabi, Panagiotis Karagiannidis, and Nida Naveed. 2022. "Additive Manufacturing of Recycled Plastics: Strategies towards a More Sustainable Future." *Journal of Cleaner Production* 335 (December 2021): 130236. <https://doi.org/10.1016/j.jclepro.2021.130236>.
- Yan, Chunze, Liang Hao, Ahmed Hussein, and David Raymont. 2012. "Evaluations of Cellular Lattice Structures Manufactured Using Selective Laser Melting." *International Journal of Machine Tools and Manufacture* 62 (November): 32–38. <https://doi.org/10.1016/j.ijmachtools.2012.06.002>.
- Yang, Lei, Yang Li, Siqi Wu, Peng Chen, Hongzhi Wu, Jin Su, Haoze Wang, Jie Liu, Chunze Yan, and Yusheng Shi. 2022. "Tailorable and Predictable Mechanical Responses of Additive Manufactured TPMS Lattices with Graded Structures." *Materials Science and Engineering A* 843 (October 2021): 143109. <https://doi.org/10.1016/j.msea.2022.143109>.
- Yu, Zhenhao, Kai Liu, Xiongfei Zhou, and Lin Jing. 2023. "Low-Velocity Impact Response of Aluminum Alloy Corrugated Sandwich Beams Used for High-Speed Trains." *Thin-Walled Structures* 183 (October 2022): 110375. <https://doi.org/10.1016/j.tws.2022.110375>.
- Zhang, Chenglin, Sibob Ba, Zifeng Zhao, Li Li, Haishan Tang, and Xuelin Wang. 2023. "Energy Absorption Characteristics of Novel Bio-Inspired Hierarchical Anti-Tetrachiral Structures." *Composite Structures* 313 (January): 116860. <https://doi.org/10.1016/j.compstruct.2023.116860>.
- Zhu, Feng, Liqiang Dong, Honglei Ma, Cliff C. Chou, and King H. Yang. 2014. "Parameterized Optimal Design of a Novel Cellular Energy Absorber." *International Journal of Mechanical Sciences* 86: 60–68. <https://doi.org/10.1016/j.ijmecsci.2013.09.021>.

Zhu, Feng, Binhui Jiang, King H. Yang, Dong Ruan, Mike S. Boczek, and Rabih Tannous. 2013. "Crushing Behavior of SKYDEX® Material." *Key Engineering Materials* 535–536: 121–24. <https://doi.org/10.4028/www.scientific.net/KEM.535-536.121>.